Automated forming of multi-ply non-crimp fabric structures

by

Guy D. Lawrence

MEng (Hons.)

Thesis submitted to the University of Nottingham for the degree of Doctor of Philosophy

June 2024

Abstract

Out-of-autoclave manufacturing methods, such as liquid composite moulding (LCM), present opportunities for economical, high-rate production of composite components. Elimination of the autoclave from the manufacturing cycle not only significantly reduces cycle times and energy consumption, but capital equipment costs are also lower, improving access to lightweight, high stiffness and strength composite components across many engineering sectors. However, a bottleneck stage common to most LCM processes is the transformation of two-dimensional dry reinforcement material to a three-dimensional preform. Defects, including out-of-plane wrinkling, fabric bridging and fibre waviness, which are possible to correct by hand during traditional laminating methods, reduce the strength and stiffness of the finished component. The generation of these defects presents a significant challenge to the development and subsequent industrial uptake of automated preforming processes, such as double diaphragm forming (DDF) and matched tool forming.

This thesis presents an investigation into the deformation mechanisms that cause defects when preforming laminates of multiple plies of non-crimp fabrics (NCFs). NCFs are well placed to be used in automated processes as absence of crimp improves their in-plane mechanical properties, but this comes at the expense of reduced overall stability. Deformation modes of NCFs, such as out-of-plane bending and in-plane shear, are well known for single plies, but the influence of inter and intra-ply frictional and nesting behaviours on formability is less well understood.

To investigate the inter-ply frictional behaviour (Chapter 3), a novel characterisation test was developed to determine coefficients of friction

when subject to conditions representative of a DDF process. Results for a pillar stitched, biaxial NCF indicated the high sensitivity of the coefficient of friction to the level of applied compaction pressure generated by the vacuum. Friction values at vacuum pressure were observed to be up to 100% higher than those recorded using a conventional sled test. Fabric-fabric friction was also observed to be orientation dependent, as parallel fibres at the inter-ply interface produced higher coefficients of friction than at any other angle. The significance of these orientation and pressure dependencies was demonstrated using a modified hemisphere forming rig to control the degree of inter-ply slip. Results from the test indicated that the resulting punch force was dependent on the fibre angles at the inter-ply interface, and that variation in the local friction behaviour can affect the formability of a component and induce unwanted defects.

Through-thickness compaction behaviour of the same biaxial NCF was investigated using a conventional compaction test (Chapter 4). The response of multi-ply laminates to normal load was found to be orientation dependent, with parallel inter-ply fibre orientations exhibiting lower compaction stiffness than at any other angle. Optical microscopy was used to visualise this behaviour at the microscale, demonstrating differing intra-ply deformation mechanisms dependent on orientation. Improvements to numerical modelling of inter-ply compression were made, as the standard hard contact model was shown to significantly overestimate contact stiffnesses.

To establish the relationship between inter-ply friction and compaction behaviours, a further compaction analysis was performed in-situ of a computed tomography (CT) scanner to evaluate the deformation of the fabric surfaces at the mesoscale (Chapter 5). Due to low contrast between dry carbon fibres and air, a machine learning approach was applied to process the data and isolate the parameters of interest. Fibre volume

fraction, fibre bundle aspect ratio and inter-ply contact area were used to analyse the fabric deformation when subjected to pressures of up to 165 kPa. Good correlation was observed between the experimental and machine learning values for the fibre volume fraction. At vacuum pressure, it was estimated that the real mesoscale inter-ply contact area was only 40% of the total apparent ply surface, which was then used in a numerical model to predict inter-ply frictional forces as a function of applied normal load.

Finally, the direct influence of inter-ply friction on in-plane shear and out-of-plane bending deformation modes was analysed (Chapter 6). It was demonstrated that the bending stiffness of a multi-ply NCF stack is much greater than the sum of its parts, due the contribution of a frictional bending moment. Similarly, by using a novel adapted bias extension test the shear resistance of a multi-ply stack under vacuum pressure was shown to be highly dependent on the number of fabric-fabric interfaces between plies of differing fibre orientations. To conclude, a DDF case study was presented to demonstrate the effect of these behaviours on the formability of an industrially relevant geometry. A finite element process model was used to analyse the out-of-plane wrinkling defects generated during the forming of thick NCF structures.

Acknowledgements

I find myself in the fortunate position of having too many kind people to thank for their support and encouragement over the last 4 years as I write these acknowledgements. In no particular order, I would like to express my gratitude to some of them:

Publication list

Journal Papers

A. Codolini, S. Chen, **G. D. Lawrence**, L. T. Harper, and M. P. F. Sutcliffe, "Characterisation of process-induced variability in wrinkle defects during double diaphragm forming of non-crimp fabric," *Compos. Part B*, vol. 281, 2024, doi: 10.1016/j.compositesb.2024.111549.

G. D. Lawrence, S. Chen, N. A. Warrior, and L. T. Harper, "The influence of inter-ply friction during double-diaphragm forming of biaxial NCFs," *Compos. Part A Appl. Sci. Manuf.*, vol. 167, Apr. 2023, doi: 10.1016/j.compositesa.2023.107426.

F. Yu, S. Chen, **G. D. Lawrence**, N. A. Warrior, and L. T. Harper, "A global-to-local sub modelling approach to investigate the effect of lubrication during double diaphragm forming of multi-ply biaxial non-crimp fabric preforms," *Compos. Part B Eng.*, vol. 254, 2023, doi: 10.1016/j.compositesb.2023.110590.

A. Trenam, C. Aza, C. Jones, **G. D. Lawrence**, L. T. Harper, A. Rhead, E. Loukaides and R. Butler, "An analytical model for wrinkle-free forming of composite laminates," *Compos. Part A Appl. Sci. Manuf.,* vol. 186, 2024, doi: 10.1016/j.compositesa.2024.108386.

Under review at time of submission:

G.D. Lawrence, S. Chen, N. A. Warrior and L. T. Harper, "Double diaphragm forming of thick non-crimp fabric preforms," *Compos. Part B Eng.*

Conference Papers

G. D. Lawrence, S. Chen, N. A. Warrior, and L. T. Harper, "The influence of inter-ply friction during double diaphragm forming of non-crimp fabrics," *SAMPE Europe*, November 2022, Hamburg, Germany.

G. D. Lawrence, S. Chen, N. A. Warrior, and L. T. Harper, "Preforming of Multi-Ply Non-Crimp Fabric Laminates Using Double Diaphragm Forming," *23rd Int. Conf. Compos. Mater. (ICCM23)*, August 2023, Belfast, UK.

Table of contents

Nomenclature

Acronym	Definition
ADFP	Automated dry fibre placement
ATL	Automated tape laying
CFRP	Carbon fibre reinforced polymer
COPV	Carbon overwrapped pressure vessel
CT	Computed tomography
DDF	Double diaphragm forming
DIC	Digital image correlation
FE	Finite element
FEA	Finite element analysis
GFRP	Glass fibre reinforced polymer
KDS	Kinematic draping simulation
KES	Kawabata Evaluation System
LCM	Liquid composite moulding
LVDT	Linear Variable Differential Transformer
ML	Machine learning
NCF	Non-crimp fabric
OEM	Original equipment manufacturer
RMSE	Root mean square error
ROI	Region of interest
RTM	Resin transfer moulding
S2S	Surface to surface
SDF	Single diaphragm forming
SEM	Scanning electron microscopy
SI	Slip/shear interface
UD	Uni-directional (fabric)
VI	Vacuum infusion
XRM	X-ray microscope

1. Introduction

1.1   Background and motivation

The demand for advanced composite materials, such as carbon or glass fibre reinforced polymers (CFRPs or GFRPs), is increasing across many different engineering sectors. Their high specific strength and stiffness makes them an ideal candidate for many weight-saving applications, offering performance advantages over more commonly used isotropic materials.

The driving force behind this demand and associated research has historically been the aerospace industry. The Boeing 787 Dreamliner and Airbus A350 XWB were both launched in 2013 and created a significant milestone, as each aircraft was constructed from over 50% composite materials by weight [1], [2]. Since then, global demand for more fuel efficient aircraft has only increased, with Airbus forecasting a demand of 40,850 new passenger and freighter aircraft by 2042 [3].

In more recent years, the energy sector has been the principal driver for composite material market growth, generating 14% of global volume between 2019 and 2022, supported by regulations and subsidies benefitting wind energy [4]. The most commonly used materials in the wind turbine industry are GFRPs, rather than CFRPs, due to cost and damage tolerance [5]. Wind turbine blades can be very large (up to 131 m in length [6]), but are typically not as geometrically complex as aerospace and automotive components, and as such are still typically produced using traditional manufacturing processes such as hand layup [7]. However, as the wind turbine blade market is expected to grow from USD$ 18.68 billion in 2023 to USD$ 83.03 billion by 2032 [8], higher rate, automated manufacturing processes such as liquid composite moulding (LCM) [9], automated tape laying (ATL) or braiding [10] may be required to meet the demand.

The escalating demand for composites from the automotive industry should also not be overlooked. The use of composites in road vehicles is no longer reserved only for high-end, niche vehicle applications, as reduced mass is required to meet challenges concerning general consumers and climate change. Many high-volume original equipment manufacturers (OEMs), such as BMW [11], Jaguar Land Rover [12] and Toyota [13] are now regularly producing and researching the use of not only CFRPs and GFRPs, but also natural fibre composites [14], as well as recycling of end of life components. For example, as well as using natural fibres and bio resins [15], ProDrive's P2T technology uses thermoplastic resin systems to enable the recovery and reapplication of the reinforcement material [16]. Body panels [17], entire chassis [18] and chassis components [19], and pressure vessels (COPVs) for use in hydrogen storage [20] have all been targets for lightweighting using composite materials. Low emission vehicles are a particularly prominent user of composites due to the relative importance of minimising component mass to maximising vehicle efficiency and range. As the UK transitions towards the 2035 zero emissions target the demand will only increase, with UK electric sales alone being expected to reach nearly 600,000 vehicles by 2028 [21].

The increasing production volumes required across so many engineering sectors are generating considerable research into many automated manufacturing processes, as traditional manufacturing techniques are simply too slow and energy intensive to meet cost and rate requirements. Parts are often hand-formed from prepreg material, layer by layer, and then cured within an autoclave. Depending on component size and the material systems used, a typical autoclave cure cycle can range from 2 to 10 hours, producing a theoretical maximum output of approximately 1,000 parts per annum (ppa). Hand layup is skilled and time-consuming work, and further complications from the storage and limited shelf life of

prepregs, combined with high capital equipment cost, results in-autoclave manufacturing being unsuitable to meet the demand for most non-aerospace composite applications.

Resin transfer moulding (RTM) processes present an opportunity to improve cycle times compared to in-autoclave manufacturing, with some processes able to produce up to 90,000 ppa [22]. Energy usage and material wastage is also reduced during high volume manufacture of net-shaped components [23]. RTM can offer significant cost savings over autoclave processes in terms of time, energy intensity and raw material cost [24], but only when considering large enough production volumes (100-10,000 ppa [25]), since RTM tooling can require high initial capital.

RTM requires the transformation of 2D raw, dry reinforcement material into a 3D component in an initial preforming stage before injecting resin under pressures of up to 100 bar [26]. The principal disadvantage of using an automated preforming stage is the formation of defects such as wrinkling, fabric bridging or fibre buckling within the reinforcement fabric architecture, which could otherwise be removed by hand with traditional hand layup processes. Subsequently, preforming is the current bottleneck in an RTM process and is hindering its industrial uptake. These defects can reduce the mechanical performance of a finished composite component by up to 40% [27], and therefore understanding why they form is critical for the development of mass-manufacturing of composite components.

Composite components across automotive and aerospace often differ in terms of size, geometry and production volumes, but non-crimp fabrics (NCFs) are of interest to many sectors due to their improved in-plane mechanical properties compared to woven fabrics and highly tailorable laminate configurations. Consequently, NCFs are well-suited for engineering applications where mass saving is critical, as a well optimised layup can maximise the specific mechanical properties of a composite

component. On paper, the absence of crimp often makes NCFs less formable than woven fabrics [28], but in reality, the increased stability makes them ideal candidates for use in automated and semi-automated preforming, which enables multiple plies to be formed in a single operation. Although NCFs have seen some automated use in industry (for example, BMW's use of NCF and RTM manufacturing in 2007 [29]), defect formation is one reason why NCFs have not yet seen more widespread adoption.

1.2 Thesis aims and objectives

The formation of defects during automated and semi-automated preforming methods is a key challenge to high volume production of light-weight composite components. The principal aim of this thesis is to further the understanding of the mechanisms that cause these defects to arise when forming NCFs, as they are of particular interest to industry. The focus of the work is on the specific deformation modes that arise when forming laminates consisting of two or more plies – predominantly inter-ply sliding and through thickness laminate compaction. This aim will be achieved through the following four principal objectives:

1. To characterise and understand the inter-ply sliding behaviour of an NCF subject to representative forming conditions.

2. To characterise and understand the through-thickness compaction behaviour of an NCF subject to representative forming conditions.

3. To determine the influence of through-thickness compaction and inter-ply friction on the formability of NCF preforms.

4. To improve process modelling techniques for forming of multi-ply preforms over realistic geometries, and to predict defects induced by multi-ply deformation mechanisms.

The motivation and reasoning for these aims and objectives is further elaborated upon in the literature review presented in Chapter 2.

1.3 Outline of thesis

To achieve the aims and objectives described in section 1.2, this thesis is divided into the following key chapters:

- Chapter 2 presents a comprehensive literature review of the state of the art of composites manufacturing, providing background information on various reinforcement material architectures and manufacturing techniques. Both single and multi-ply deformation mechanisms are analysed, and common characterisation methods are evaluated for each. A review of existing numerical modelling techniques is presented for conducting fabric forming simulations. Finally, the research questions created by the literature review are highlighted and related to the aforementioned aims and objectives.

- Chapter 3 presents a novel method that attempts to overcome the limitations of existing inter-ply friction characterisation tests, addressing Objective #1. This test is used to investigate the frictional response of a biaxial NCF to parameters of interest, including the applied normal load and inter-ply fibre orientation. The influence the frictional behaviour has on a preform is demonstrated using a matched tool forming process, to address Objective #3.

- Chapter 4 focuses on the through-thickness compaction characterisation of the same biaxial NCF to meet Objective #2. Compaction tests are used to measure the laminate response of dry laminates of varying thicknesses and ply orientations. The nesting behaviour of the laminate is evaluated using both compression tests and optical microscopy and compared to a similar biaxial NCF. Finally, the experimental data is used to improve an existing numerical process model to define interactions between fabric plies, in view of Objective #4.

- Chapter 5 considers the relationship between the macroscale friction and compaction mechanisms observed in the previous two chapters, concluding Objectives #1 and #2 and informing Objective #3. Microscale CT scanning is used to capture laminate deformation subject to increasing through-thickness compaction loads. A novel methodology to process the CT data is presented, employing machine learning instance segmentation to isolate the changing shape of the fabric yarns. The output of the model is used to estimate key parameters of interest, including mesoscale inter-ply contact area, which is then used to explain macroscale frictional behaviour observed in Chapter 2.

- Chapter 6 finalises the work on Objective #3 by considering the influence of friction on the isolated bending and shear deformation mechanisms of biaxial NCFs with novel methods presented for characterising multi-ply behaviours. This influence is fully contextualised through the use of a finite element (FE) forming model, using experimental data from previous chapters to accurately

consider the friction and compaction behaviours. Finally, this model is validated by experiments, using an industrially relevant preform geometry, produced using DDF.

- Chapter 7 concludes the work completed by summarising the key contributions made and providing guidelines for multi-ply process modelling and analysis. Finally, areas for potential future work are discussed.

1.4 Chapter summary

This first chapter has outlined the thesis, contextualising the overarching aims and objectives with a brief introduction to the background of the problem. The structure of the work has been presented, and each chapter's relationship with the objectives of the research has been discussed.

A simple graphic is shown in Figure 1.1 to summarise the structure of this thesis and each chapter's relation to the aims and objectives of the work.
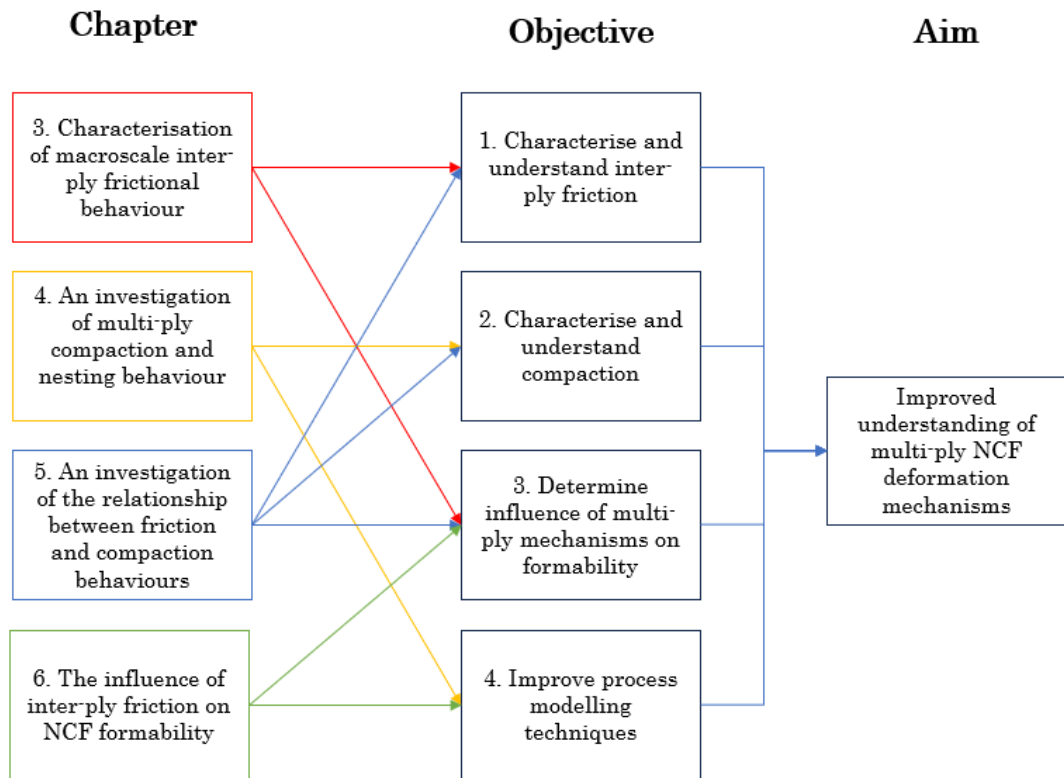
Figure 1.1 - Overview of thesis structure.

2. Literature Review

2.1. Introduction

This chapter reviews the current state-of-the-art for composites manufacturing to best understand the mechanisms of how dry composite fabrics transform from two-dimensional to three-dimensional geometries. Key manufacturing techniques and common fabric architectures are presented, followed by a discussion of the principal forming mechanisms for both single plies and multi-ply laminates. Typical defects that these mechanisms can cause are evaluated, followed by an analysis of common characterisation methods to describe their behaviour. Finally, the use of advanced methods of predicting and measuring fabric forming behaviours are discussed, including finite element (FE) models.

2.2. Out-of-autoclave manufacturing of fibre reinforced composites

Reduction of both production cycle time and energy consumption is critical to meeting the rising demand of composite materials. The end market for composite products is expected to expand at a compound annual growth rate of 3.3% and reach an estimated value of USD\$ 114.7 billion by 2024 [30]. Traditional manufacturing techniques (predominantly hand layup) are not positioned to meet this demand and present a major bottleneck in the production process. Viable solutions to increasing the rate production must reduce the dependency on touch-labour and increase levels of automation [31]. To reduce energy consumption and meet sustainability targets within the composites sector, a shift away from autoclave focused manufacturing is necessary. The embodied energy of CFRP has been reported up to values of 1150 MJ/kg [32], significantly higher than that of isotropic materials such as steel, which with an average amount of recycled content has a value of only 20.1 MJ/kg [33]. To be competitive within the

industry, out-of-autoclave processes must not only reduce energy consumption and increase rate, but maintain or improve upon component quality, scalability of size, adaptability of geometry and minimise cost.

2.2.1. Liquid composite moulding

Liquid composite moulding (LCM) processes are semi-automated composite manufacturing methods that produce high-rate, near-net shape composite components with complex geometry [34]. The two most common LCM processes are vacuum infusion (VI) and resin transfer moulding (RTM), and both operate under similar principles. Compaction pressure is applied to dry reinforcement (typically continuous fibre) to consolidate the laminate, after which a low-viscosity polymer matrix is infused and allowed to cure once fully permeating the fabric. For VI, atmospheric pressure is used to both consolidate the dry reinforcement and drive the flow of the resin within the polymeric vacuum bag. Prior to infusing reinforcing material with resin, a semi-automated forming operation is performed on the preform stack to transform the 2D fibre reinforcement into a 3D component architecture. Processes such as automated dry fibre placement (ADFP) can be used to produce highly optimised fabric blanks to minimise material wastage and enhance mechanical properties of the preform, although production rate can be low. The geometry of the preform can be stabilised by using a small quantity of heat-activated polymer binder so it can subsequently be removed from the tool and trimmed to size as required. The polymer matrix is then infused under high pressure, typically < 10 bar [34]. This process of producing a composite component from its constituent materials is shown in Figure 2.1.
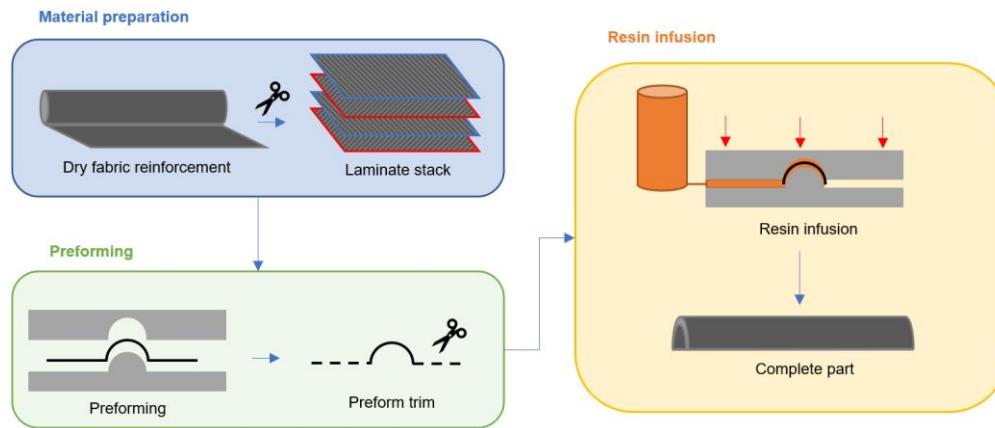
Figure 2.1 - A diagram of a 3 stage semi-automated manufacturing process, showing the material preparation and cutting, the preforming of the fibre reinforcement and the infusion of resin under pressure.

The preforming stage of any LCM process is critical to ensure defect free fibre architectures are produced of the final composite component. Where traditional hand-layup techniques would enable careful manipulation of the laminate by a skilled operator, the semi-automated preforming processes employed for LCM do not. As a result, preforming is often the primary production bottleneck of any LCM manufacturing, and therefore mostly been employed for relatively simple part geometries used in the aerospace industry [35–37]. Some preforming processes can also be used to directly produce composite components using thermoplastic [38] or thermoset [39] prepreg material, however this thesis will only consider their application to dry fibrous preforms for LCM applications.

2.2.2. Matched tool forming

One method of preforming both continuous and discontinuous fibre architectures is matched tool forming [40–42]. Using a punch, die and blank holder, matched tool preforming is a similar process to that of sheet metal punch forming. The 4-stage process to creating a preform using matched tool forming is shown in Figure 2.2:

a) Preparation: The tool surfaces are prepared with necessary mould release agents and binding agent is applied to the fabric blank, which can then be transferred to the tool.

b) Blank close: The blank holder is closed to constrain the preform material to the edge of the tool cavity. In a matched tool process, the constraining force and forming force are independent of one another.

c) Forming: The punch is driven into the die using a hydraulic press, passing through the blank holder. The fabric blank deforms, taking the shape of the tool. The heated tool activates the polymer binder so that it can stabilise the preform after deformation.

d) Preform removal: The punch is raised and the preform released from the mould, now as a 3D fabric architecture.
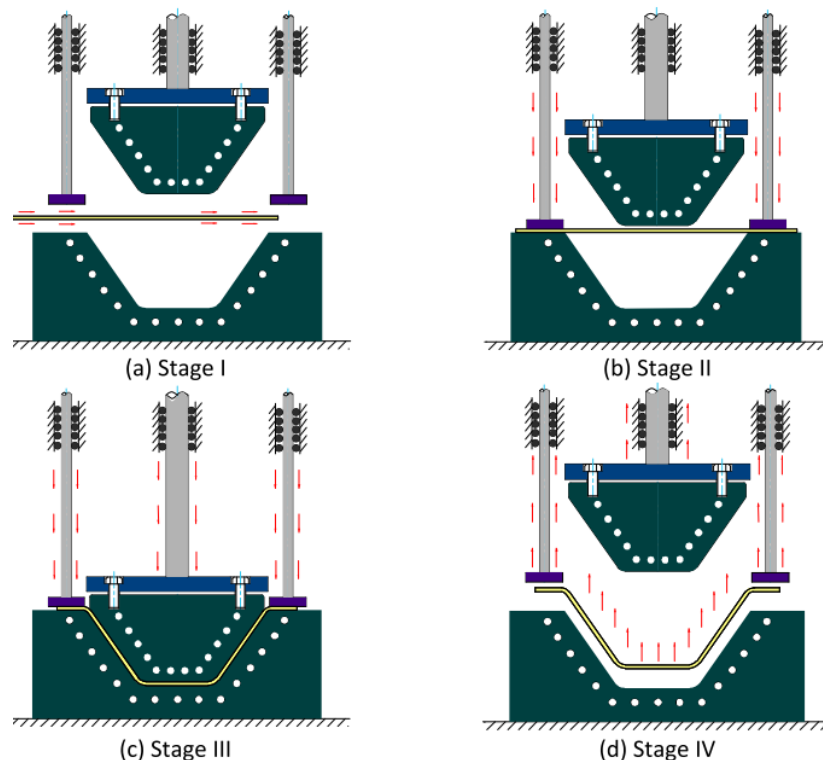
Figure 2.2 - A diagram showing the 4 stages undertaken in a typical matched tool preforming process [40].

The significant cost of industrial-scale matched tool machinery and its required tooling typically limits its use to high volume components (~30,000 ppa [43]), such as those seen in the automotive sector. Another limiting factor of matched tool preforming is that of size as the punch is actuated by a hydraulic press, very large components such as wind turbine blades or aerospace wing spars become prohibitively expensive to manufacture and maintain accuracy and part quality over large lengths.

2.2.3. Diaphragm forming

Diaphragm forming is a semi-automated method of manufacturing dry fibre preforms for use in LCM processes [34,44–46] A significant advantage of diaphragm forming over other forming processes is the lower capital cost, as the required vacuum pumps and associated rig are far cheaper than press tool or in-autoclave equipment. Additionally, its adaptability to a large range of component sizes with minimal difference in cost make diaphragm forming an attractive option for mass production of composite preforms. This scalability is limited only by the size of the diaphragms and rig available, as larger components can create challenges to handling and processing. However, there is evidence of DDF being used to manufacture structural aerospace composite components of up to 14m in length, significantly improving production rates when compared to hand-layup methods [47].

Diaphragm forming can be conducted with either one deformable diaphragm (single diaphragm forming, SDF) or two deformable diaphragms (double diaphragm forming, DDF). The DDF process is shown in Figure 2.3, and can be described in 4 principal stages:

  a) Preparation: the material blank with applied powder binder is placed between two deformable diaphragms applied with mould release agent to improve handling. The first vacuum is induced

between the diaphragms, consolidating the fabric stack, and constraining its movement relative to the tool position.

b) Tool approach: Heaters are used to activate powder binder prior to forming. The diaphragm frame is then lowered over the tool, bringing the diaphragms and fabric into contact with the upper surface of the tool.

c) Forming: A second vacuum is induced underneath the lower diaphragm, causing the diaphragms and fabric to draw into the tool and form the desired preform geometry in a single, rapid step. Both vacuums remain in place whilst heat is applied to activate the applied powder binder.

d) Part removal: Once the binder has cooled, the two vacuums are removed, and the upper diaphragm is detached. The finished preform can then be released from the mould.
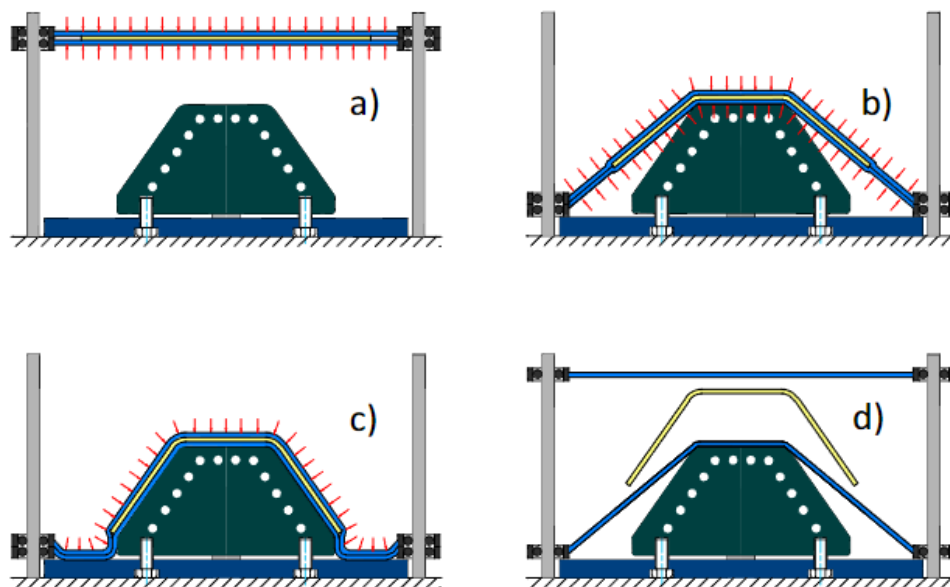
Figure 2.3 – A diagram showing the 4 principal stages of a double diaphragm forming process [44].

SDF processes are very similar to DDF, but do not have a secondary diaphragm to constrain the fabric prior to or during the forming step (stage c). Whilst this does offer more process flexibility (as multiple plies can be formed sequentially), the lack of control on the fabric provided by the diaphragm can increase variability, and the number and magnitude of defects found in the finished preform [48].

2.3. Dry fabric architectures

Composite textile fabrics are typically constructed of continuous yarns of glass, carbon or aramid fibres. Raw fibres are supplied on a spool (also referred to as a bobbin) and are then spread to achieve the desired yarn shape and size [49] (typically 6K, 12K or 24K), which can then be stitched or woven together using industrialised techniques similar to historical weaving or knitting, but at rates of several hundred kg/hr [50]. Textile fabrics present a good balance of material cost and manufacturability, but can produce large amounts of material scrap due to the on-roll format. Preparation of plies from feedstock rolls can waste between 25% and 50% of the input material for a given component [51], highlighting the need to rationalise the preforming process wherever possible.

The final intermediate composite material can take many forms, but the present work focuses on carbon fibre 2D woven textiles and non-crimp fabrics (NCFs), due to the increased interest in thin-ply composite laminates in the aerospace sector and other high-performance industries [52].

2.3.1. Woven fabrics

Arguably the most common form of dry composite textiles, woven fabrics are typically made of two yarn directions (warp and weft) that are interlaced in a repeating structure. The subsequent over-under undulation

of the yarns, known as crimp (shown in Figure 2.4), can have a significant effect on the formability, handleability and the overall mechanical properties of a part.
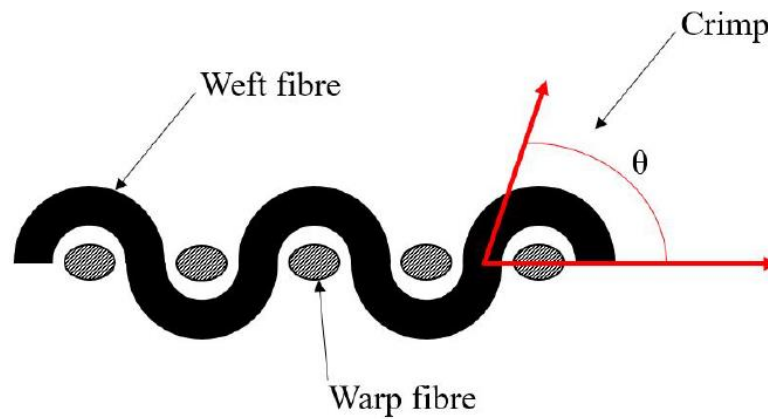
Figure 2.4 - A cross section of a simple woven fabric highlighting yarn crimp.

Fabric weaves with a large degree of crimp, such as the plain weave shown in Figure 2.5a), are easier to handle, since crimp increases the stability of the fabric. This is caused by the transfer of longitudinal stiffness of the yarns into the through thickness directions and increasing the intra-ply friction through the number of fibre to fibre contact surfaces. However, this also reduces the in-plane stiffness and strength of the fabric. Different weaves can decrease the amount of crimp present in a fabric (Figure 2.5b and c), which can improve mechanical properties and handling stability, at the cost of ease of formability.
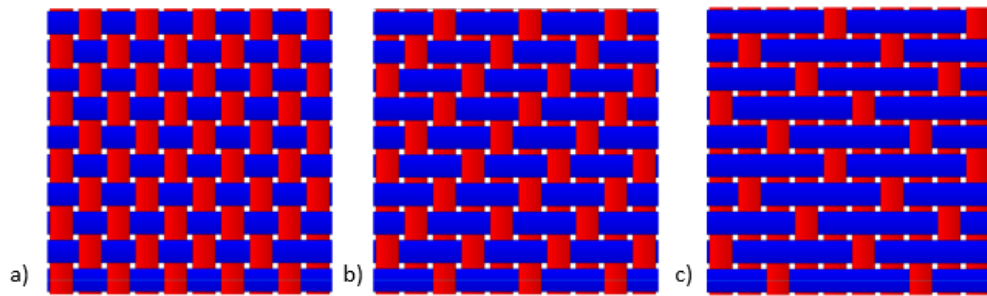
Figure 2.5 - Commonly found fabric weave patterns, generated using TexGen software [53]. a) Plain weave. b) Twill weave. c) Satin weave.

2.3.2. Non-crimp fabrics

Non-crimp fabrics (NCFs) are fabric materials that have significantly less crimp compared to traditional woven fabrics. One or more unidirectional (UD) plies are stitched together with an additional material, typically whose contribution to the mechanical properties of the complete fabric are negligible compared to that of the reinforcement fibres. The absence of crimp in the fabric results in improved in-plane mechanical properties [54,55], which alongside the inherent flexibility in laminate design makes NCFs an attractive choice for use in a wide range of composite components. Bibo et al. [56] demonstrated an improvement in both tensile strength and stiffness of approximately 30% when comparing a glass fibre NCF to a satin weave composite with comparable volume fractions, as shown in Figure 2.6.
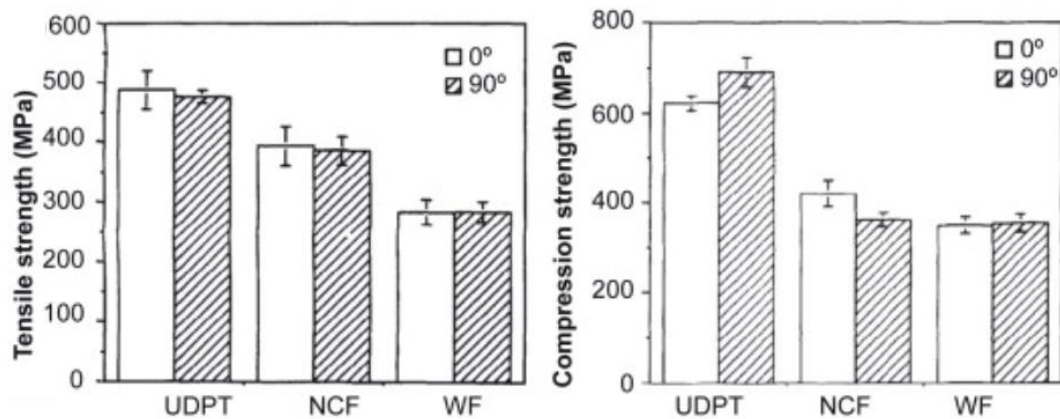
Figure 2.6 – Comparison of tensile (left) and compressive (right) strengths for 3 glass fibre composites of similar fibre volume fractions: unidirectional prepreg tape (UDPT), NCF and a woven composite with quasi-isotropic layup (WF) [56].

The improvement in mechanical properties comes at the cost of stability of the NCF material architecture, as each yarn is subject to fewer constraints. This can result in improved formability, as the fabric is able to easily conform to a given tool geometry, but the drawback is that the material is prone to generate defects when forming.

Single ply, UD NCFs provide the greatest flexibility in laminate design, as a specific fibre angle can be selected for each individual layer. This presents opportunities for UD NCFs to be used in laminates alongside other composite fabrics, providing additional strength and stiffness in the loading direction with minimal supplementary weight. For example, UD NCFs are often used in large wind turbine blades [57] and aerospace wing spars [58] where the principal loading direction is well known and can easily be reinforced. However, forming of dry UD NCFs presents challenges, as low transverse tensile stiffness can cause gapping and local in-plane waviness [59,60]. For the same reason, UD NCFs can be fragile when handling, and therefore usually require stitches or the inclusion of additional material to improve stability [61]. Furthermore, a complex

tailored layup design significantly inhibits production rate, as laying each individual ply at specific angles is a time-consuming process.

Biaxial NCFs present a potential solution to the obstacle of production rate; two UD layers are stitched together to create a single ply (Figure 2.7), increasing the rate at which laminates can be assembled. The yarn directions are typically stitched perpendicular to each other, with a stitch direction usually at either 45° or 90° to that of the fibre direction. The constraining effect of the stitch pattern is highly influential on the shear behaviour of a biaxial NCF, which in turn influences its formability. For example, the orientation of the in-plane segments of a pillar stitch pattern (Figure 2.8a) can lead to asymmetric shear behaviour [62], whereas a tricot stitch pattern (Figure 2.8b) exhibits shear behaviour, independent of direction [63].
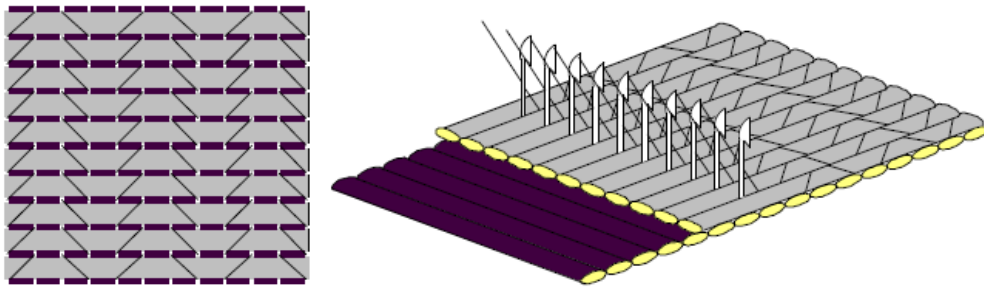
Figure 2.7 - Typical biaxial NCF assembly with a tricot stitch pattern [40].

Triaxial or quadaxial NCFs consist of additional layers of UD material stitched together in a similar manner to that of biaxial NCFs. More layers increase the handling stability and assembly time of the fabric [64]. However, the limitation to laminate design and decreased formability [65] often make triaxial and quadaxial NCFs a less attractive choice in general to industry than biaxial or UD fabrics (although are sometimes used in

hand layup manufacturing), and are therefore considered outside the scope of this thesis.
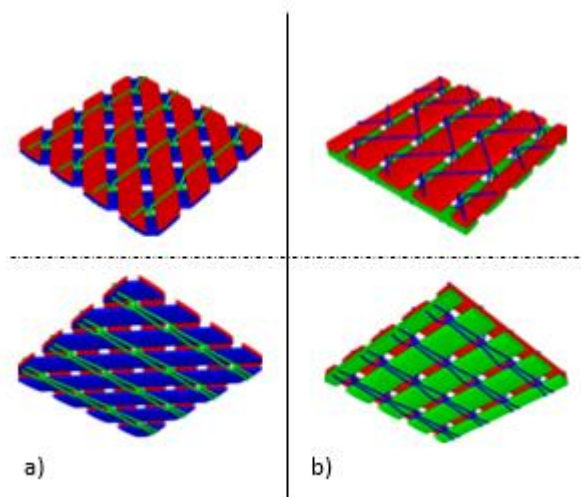
Figure 2.8 – Upper and lower perspectives of biaxial NCFs with a) pillar stitches and b) tricot stitches [63].

2.4. Single-ply NCF forming mechanisms

Understanding the mechanisms by which NCFs deform when transforming from a 2D fabric into a 3D preform is critical to the development of processes such as DDF. These deformation mechanisms are highly dependent on the architecture of the fabric in question and are influenced in turn by the constraints applied upon them by a given forming process. Deformation is typically non-linear and irreversible [40].

Macroscale forming mechanisms can be considered in 3 main modes: tension, shear and bending behaviours. Despite the multitude of differences in the structure of reinforcement materials used in forming processes, the deformation modes are often common between them.

2.4.1. Intra-ply shear behaviour

Considered to be the primary deformation mechanism for fibre-based materials [43,66], intra-ply shear describes the rotation, compaction and slip of tows about their crossover points, as shown in Figure 2.9. Since a two-dimensional fabric cannot conform to a three-dimensional tool (especially one with Gaussian curvature), the yarns of the fabric must rotate relative to each other in order to conform to the target geometry [43].
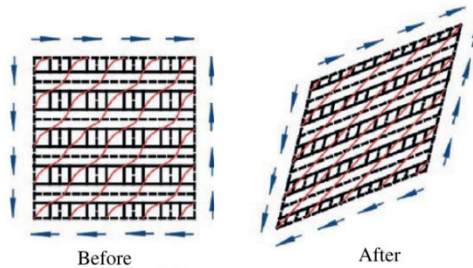
Figure 2.9 – Shear forming mechanism of a typical biaxial NCF [67].

The shear modulus of a fabric, G, is significantly smaller than its tensile counterpart, E (G/E < 0.001) [67]. In a woven fabric, this is due to the limited resistance created by the inter-yarn friction at the warp-weft crossover points. The shear behaviour of a plain weave glass fibre fabric is shown in Figure 2.10, indicating 3 distinct regions of shear behaviour [68], typical of many 2D woven fabrics. At low shear strain (Region 1), the shear resistance produced by the fabric is relatively low, as it is only a function of the weak intra-yarn frictional forces. As the yarns begin to partially contact, the filaments re-organise and compact together, increasing the measured shear force (Region 2). Upon reaching a critical shear angle, also known as the locking angle, the yarns are entirely laterally compressed, producing a sharp increase in in-plane shear force within the fabric (Region 3). This phenomenon is also known as shear locking.
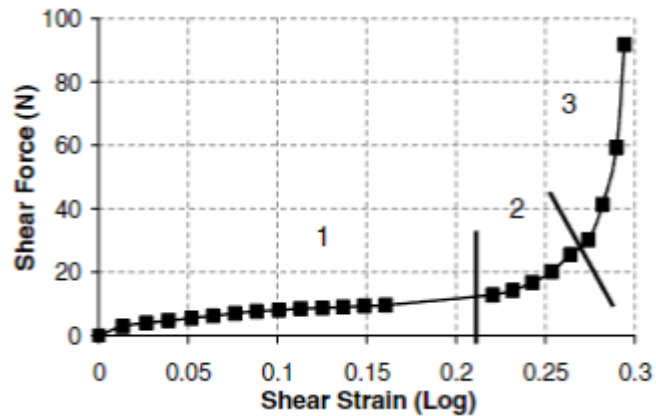
Figure 2.10 - Shear strain vs shear force for a plain weave glass fibre fabric, with 3 distinct regions of shear behaviour indicated [68].

In a biaxial NCF, the elimination of fibre crimp means that inter-yarn friction is much lower than woven fabrics, since there are no fibre crossover (pivot) points. The shear behaviour of the NCF is dominated by interactions from the stitch pattern. This results in typical biaxial NCFs exhibiting asymmetric shear behaviour, depending on the orientation of the stitches relative to the primary yarns [69,70]. For a biaxial NCF with fibre orientations ±45° relative to the stitch direction, this can be designated positive shear (stitches in tension) or negative shear (stitches in compression), as shown in Figure 2.11a. In positive shear, the stitches are likely to rupture at larger shear angles (as shown in Figure 2.11b), generating a sudden drop in shear resistance and non-elastic deformation. Since the compressive stiffness of the stitching is significantly less than the tensile stiffness, there is no peak found in negative shear, where the gradual increase in shear resistance is produced using the same yarn friction and compaction mechanisms as found in woven fabrics.
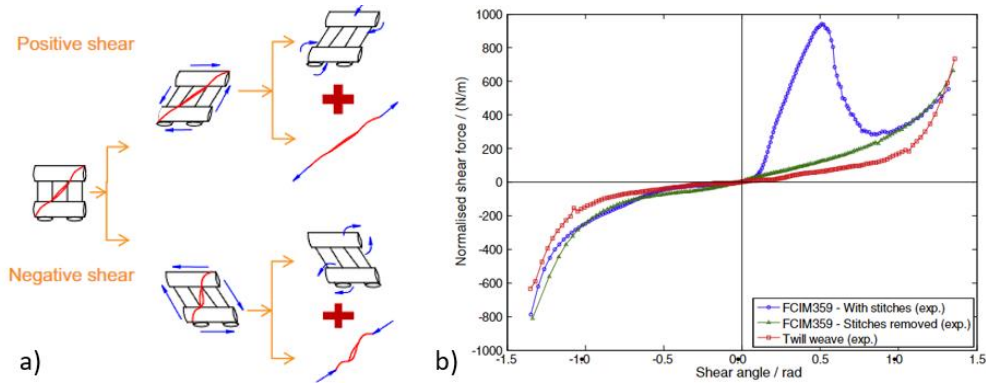
Figure 2.11a) – Schematic showing the asymmetric shear behaviour of a biaxial NCF as dictated by stitch tension and compression. b) Resulting difference in shear behaviour [62].

Intra-ply shear behaviour of UD NCFs is intrinsically linked to the transverse tensile behaviour due to their highly anisotropic structure, and so UD fabrics are never subject to pure shear deformation when forming [61]; instead shear strains rarely occur without inherent transverse strain [59]. Subsequently, as demonstrated in Figure 2.12, the shear resistance of a UD fabric is typically much lower than that of bi-directional fabrics due to the weak transverse tensile strength of the fabric.
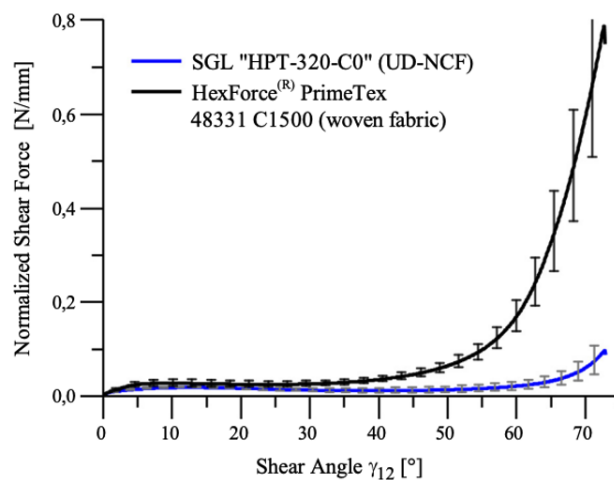
Figure 2.12 - Normalised shear force versus vs. shear angle comparison of a UD NCF and woven fabric material [61].

2.4.2. Out-of-plane bending behaviour

Out-of-plane bending behaviour (Figure 2.13) of NCFs is another deformation mechanism critical to forming curved geometries without damaging fibres. The bending stiffness is significantly lower than the in-plane stiffness as yarns can slide relative to each other [66], but it also exhibits non-linear behaviour. Consequently, conventional Bernoulli-Euler beam theory is not appropriate for describing the bending behaviour of dry NCF material, and more complex definitions are required. Figure 2.13 shows the typical bending mechanism for a biaxial NCF.
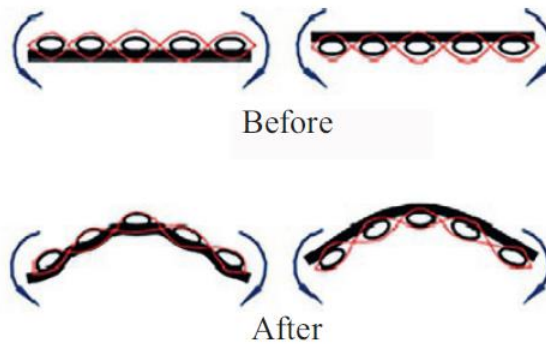
Figure 2.13 - Bending mechanism of a typical biaxial NCF [43].

Due to the fabric architecture, the stiffness is dependent on the direction of bending. In a positive bending case (right side of Figure 2.13), the longitudinal fibres on the upper face are loaded in the tensile direction, where the transverse fibres on the lower face are subject to a transverse compressive load. This gives the fabric a higher bending stiffness than when bent in a negative direction [71], as shown by the left side of Figure 2.13. This behaviour is quantified for a biaxial NCF in Figure 2.14, showing a simplified constant bending stiffnesses for both directions, determined using a cantilever bend test.
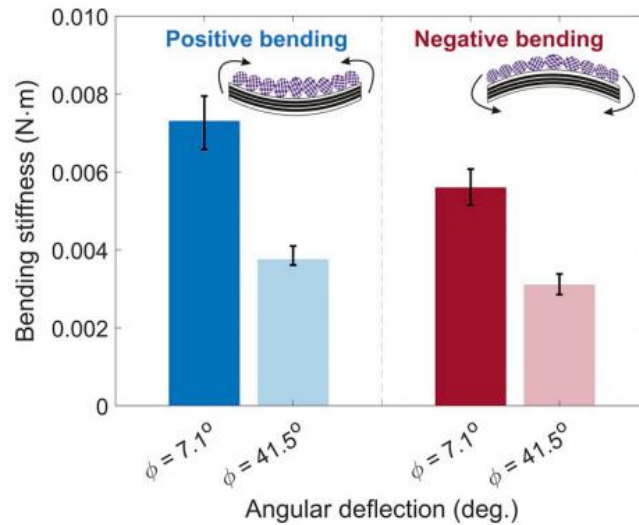
Figure 2.14 - Constant bending rigidities for positive and negative bending directions at two different angular deflections [71].

However, the bending stiffnesses of many composite fabrics are not linear [71–75]. Due to buckling and slippage of fibres and yarns, composite fabrics tend to exhibit decreasing bending stiffness as the curvature of the bending profile increases, as shown in Figure 2.15 [74], where the bending stiffness of the biaxial NCF rapidly approaches zero before stabilising into a linear profile. It can be seen that the positive and negative bending profiles are slightly different, indicating again how the mesoscale architecture of the fabric influences its bending behaviour [71]. It is also of note how the majority of the curve is significantly less stiff than the constant values obtained from the standard cantilever bend test, designated $B_{41.5°}^{NCF}$ on Figure 2.15, indicating the importance of considering the non-linearity of the bending behaviour during characterisation of anisotropic materials such as NCFs. Methods of characterising bending behaviours of NCF materials are discussed in further detail in Section 2.7.2.

Figure 2.15 - Non-linear bending stiffness versus curvature behaviour for a biaxial NCF [74].

Liang et al. [76] considered the non-linear bending behaviour of a dry multi-ply stack of twill carbon fibre woven fabric, the results of which can be seen in Figure 2.16. Like the aforementioned biaxial NCF, the bending behaviour of a single ply is non-linear (Figure 2.16c). The bending stiffness of a 20-ply stack of the same material is significantly larger than the sum of its parts and exhibits increased non-linearity. This is attributed to frictional forces between the plies as they slide over one another, producing a "friction moment", as shown in Figure 2.16d, and is a phenomenon that can be observed in the bending of other laminate materials, such as a stack of paper [76].

Figure 2.16 – a) 20-ply bending sample. b) Single ply bending sample. c) Bending moment versus curvature of single ply sample. d) Bending moment versus curvature of the multi-ply stack and the sum of its parts [76].

Bending behaviour of UD NCFs is less well documented in existing literature. Senner et al. [77] characterised the bending behaviour of a UD NCF with the aim of describing it with a constitutive model. It was found that the UD material studied exhibited very different bending characteristics to an isotropic material (polypropylene), as would be expected. It is concluded that the bending behaviour is highly anisotropic, being similar to that of biaxial NCFs in the fibre direction and minimal in the transverse direction. Schirmaier et al. [61] found that this anisotropic bending stiffness can produce a specific wrinkling mode during the draping of UD NCFs, highly dependent on the fibre direction. The authors conclude

that the bending behaviour of the UD NCF requires further investigation to complete a proper characterisation.

2.4.3. Frictional behaviour

The full effect of frictional behaviour on fabric forming is not yet fully understood, due to its complexity, and there is currently no testing standard available for characterising the frictional behaviour of fibrous materials (i.e., determining the static and dynamic coefficients of friction). A benchmark investigation [78] studied the influence of different factors on the frictional behaviour of a tool-ply interaction in an attempt to develop a precise characterisation method, but differences in results of dynamic coefficient of friction of over 50% were recorded by different research groups.

Frictional behaviour, and subsequently characterisation, of a composite fabric can be classified into three scales [79]: micro (individual filament level), meso (tow level) and macro (fabric or ply level). The scales are not independent of one another however, as changes on the microscale (i.e., movement of individual filaments) will affect the mesoscale behaviours, which will ultimately affect macroscale mechanisms by extension [80]. It is therefore important to understand the frictional mechanisms that contribute to fabric deformation at each of these scales, and how they can be evaluated differently.

A coefficient of friction can be static or dynamic, the former of which describes an initial resistance to relative motion, and the latter a resistance after movement has begun. Empirical laws of friction can be used to describe the frictional behaviour of most isotropic, non-deformable materials [81]:

1. Amontons' first law: the frictional force between two surfaces is proportional to the normal load applied to the surfaces.

2. Amontons' second law: the frictional force between two surfaces is independent of their apparent area of contact.

3. Coulomb's law: the frictional force between two dry surfaces is independent of the relative sliding velocity.

The first of Amontons' laws is commonly known as the Amontons-Coulomb friction law (or often simply Coulomb's law) [82], and is typically presented in the form $F_t = \mu N$, where F_t is the total frictional force resisting sliding between two surfaces, N is the applied normal force between the surfaces and μ is the ratio between them, known as the coefficient of friction. However, since dry reinforcement fabrics of all architectures are deformable when subject to an applied load normal through the thickness direction, the standard empirical laws of friction do not necessarily apply [83]. Research into tool-ply friction for dry fabrics considers many different processes, including matched tool forming [79,84–86], filament winding [87] and 3D weaving [88], among others. Tool-ply frictional behaviour of NCFs was investigated by Avgoulas et. al [89], who demonstrated that the coefficient of friction between ply and tool reduced by between 25% and 47% when subject to increased normal load. Mulvihill et al. [85] examined the effect of tool surface topography on tool-ply friction of individual carbon fibre tows, and found that the frictional forces obeyed a power law description shown in Equation (2.1), which agrees with previous work on tool-ply friction by the same authors [79].

$$F_t = kW^n \tag{2.1}$$

This power law is derived from the Amontons-Coulomb friction law and was originally described by Howell et al. [90], where k is an experimentally derived proportionality constant with units of N^{-n+1}, relating normal load

W to frictional load F_t. Index n is a dimesnsionless fitting parameter that describes the deformation mechanism of the fabric and is given in the range $\frac{2}{3} \leq n < 1$, where a value of $\frac{2}{3}$ represents a fully elastic deformation, and 1 represents fully plastic [91]. For non-deformable materials, $n = 1$ and Equation (2.1), reduces to a more typical Amontons-Coulomb Law.

It should also be noted that many studies investigating tool-ply friction of composite fabrics focus on the inclusion of viscous resin alongside that of fabric reinforcement. A common characterisation approach is that of a Stribeck curve [92–96], such as the example shown in Figure 2.17. A Stribeck curve shows the variation in coefficient of friction, μ, with the dimensionless Hersey number (sometimes referred to as the Stribeck number). The Hersey number is defined by Equation (2.2), where η is the dynamic viscosity of the resin, U is the sliding speed and W is the applied normal load at the interface [97].

$$Hersey\ Number = \frac{\eta U}{W} \qquad (2.2)$$
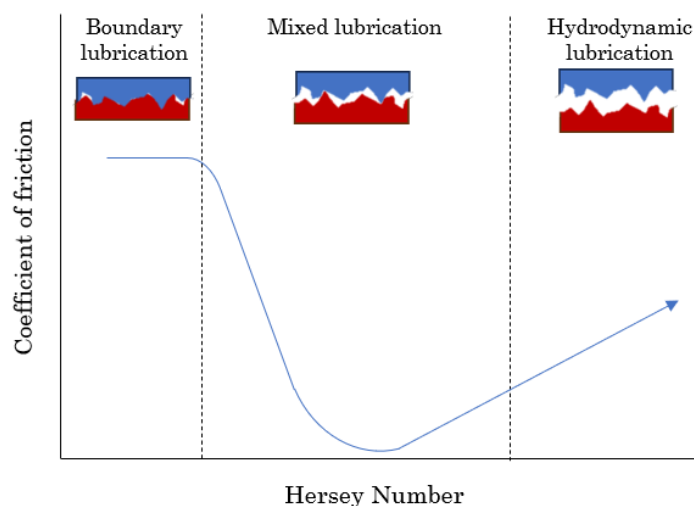
Figure 2.17 - Variation in coefficient of friction with Hersey number, known as a Stribeck curve. The three distinct lubrication regimes are indicated.

The Stribeck curve describes 3 distinct regions of lubrication. At very high slip pressures, or low slip rates and viscosities, the region is designated boundary lubrication. In this scenario, the support provided by the resin film is negligible, and large frictional forces are generated by the interactions of the tool surface and the fabric reinforcement. An increasing proportion of the load is supported by the resin as the mixed lubrication region is reached (sometimes referred to as the elasto-hydrodynamic region [98]), generating a substantial decrease in μ as fewer tool-ply interactions occur. When the Hersey number is sufficiently high, the lubrication region is considered to be hydrodynamic, whereby the applied load is fully supported by the hydrodynamic pressure within the resin film between the tool and the ply. This behaviour is also relevant for ply-ply sliding of prepregs, as well as ply-tool interactions. Larberg et al. [99] observed large differences in lubrication regime (and subsequent coefficients of friction) corresponding to material features such as volume fraction of fibres, fibre stiffness and inclusion of toughening agents. This highlights the significance of fabric structure when considering ply sliding, and how apparently similar materials can exhibit very different frictional behaviours.

However, the importance of tool-ply friction to the forming of NCF materials is perhaps of less consequence to the preform quality than other material and process parameters. Figure 2.18 shows the differences in macroscale wrinkle amplitude and location for a range of process parameters in a 2-ply DDF process, including tool-diaphragm friction and ply-diaphragm friction and ply-ply friction [100]. This enables analysis of which process parameters are most significant to the formability of this particular preforming case. It can be seen that, for this DDF preform, these two surface interactions are of little consequence to the formability of the hemisphere compared to ply-ply friction, each producing a < 8% difference in wrinkle amplitude and location.
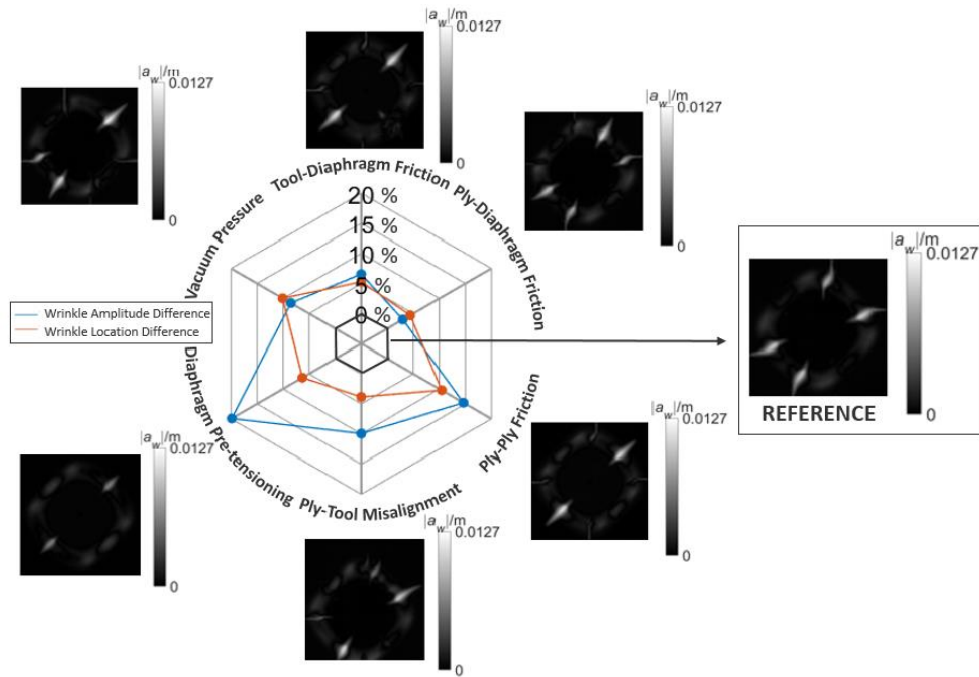
Figure 2.18 – A polar chart displaying the percentage change in wrinkle amplitude and location as a function of various experimental parameters of interest [100].

A similar relationship was observed by Yu et al. [45] for a similar 2-ply DDF preform using a biaxial NCF. It was found that for low inter-ply coefficients of friction (< 0.15), diaphragm-ply coefficients had no impact on the maximum wrinkle length of a C-spar preform. For higher levels of inter-ply friction, increasing diaphragm-ply coefficients produced only slightly longer wrinkles, and it is concluded that the influence of the inter-ply coefficient is likely to become even more dominant with an increasing number of plies. Therefore, the focus of the rest of this thesis will be on ply-ply interactions of biaxial NCFs, rather than ply-tool, due to their greater significance on the forming process.

2.4.4. In-plane tensile behaviour

In-plane tensile stiffness of a biaxial NCF fabric has the largest magnitude of the deformation modes (bending and shear), due to the high stiffness of the fabric reinforcement in the fibre direction. The tensile behaviour of an NCF is dictated by the reorganisation and elongation of fibre bundles at the meso and microscales within the fabric, as shown in Figure 2.19. In woven fabrics, this can cause non-linear tensile behaviour at small loads due to the undulations of warp and weft yarns [101,102]. Whilst some minor non-linearity has been observed in the tensile strain behaviour of biaxial NCFs (attributed to fibre misalignment or stitch pattern [103]), the tensile behaviour tends to be linear [104] and so this is generally ignored in process simulations for computational efficiency without significantly compromising precision when modelling tensile behaviour [40,105,106].
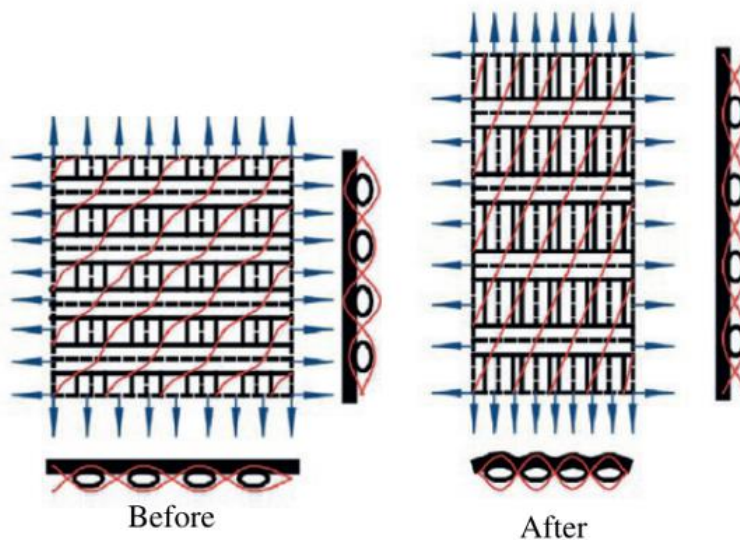
Figure 2.19 - In-plane tensile forming mechanisms of a biaxial NCF [43].

As biaxial NCFs are assumed to be effectively inextensible in the fibre directions, the formability of a preform is not typically affected by its

response to tensile loading. However, it has been shown that high levels of tensile stress within an NCF lead correspond to regions of fabric bridging in regions of complex geometry, such as concave areas [44].

For UD NCFs, tensile behaviour in the longitudinal fibre and transverse directions differs significantly when compared to biaxial NCFs. Along the fibre directions, the tensile stiffness is very high, and the fabric can be considered inextensible, in the same manner as biaxial NCFs. In the transverse direction however, the tensile load is transmitted by the stitch pattern and any additional materials used to hold the yarns together (such as supplementary glass fibres found in some carbon UD NCFs). Figure 2.20 [61] shows the large amount of fabric strain generated by the relatively weak stitching pattern during a uniaxial tensile test. Despite the tensile forces experienced by the fabric being fairly linear, fabric gapping causes macroscale transverse tensile behaviour that is very complex to model [107].
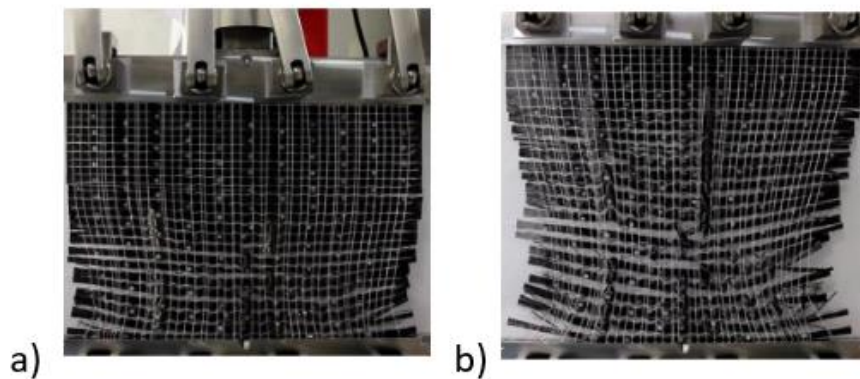
Figure 2.20 - Complex transverse tensile behaviour of a carbon fibre UD NCF demonstrating large amounts of fabric strain and resulting gapping between yarns a) before and b) after a transverse tensile test [61].

2.5. Multi-ply NCF deformation mechanisms

The following section of this literature review will consider the deformation mechanisms that occur in a stack of multiple plies during a forming process. These mechanisms can be more complex, due to additional dependency on both material and processing parameters, and often have subsequent effects on the aforementioned single-ply deformation mechanisms (such as inter-ply friction increasing multi-ply bending stiffness, as discussed in Section 2.4.2). Multi-ply mechanisms (friction in particular) are highly dependent on material properties and processing conditions, and consequently very few characterisation standards can be found in the literature.

As existing literature highlights inter-ply friction as being of significant influence on the formability of composite fabrics [45,108–110], it will be the main focus of this thesis.

2.5.1. Inter-ply frictional behaviour

Macroscale sliding between plies (inter-ply slip) is a deformation mechanism that is critical to creating 3D preforms from 2D fabric architectures [111] (the influence of inter-ply friction on the quality of preformed composite fabrics and how it can generate defects is discussed in detail later in this literature review, in section 2.6). The amount of slip that occurs during a forming process is dependent on the tool geometry, the material being formed [108] and the process parameters that the material is subject to, and as a result characterisation of inter-ply frictional behaviour has proven difficult to standardise [78]. Despite this, many investigations have been undertaken to better understand inter-ply friction and its effects on the formability of composite components [112–116]. However, most existing studies in the literature focus on the inter-

ply friction of saturated fabrics (i.e., prepregs), which can sometimes exhibit different frictional behaviours to dry counterparts.

Multiple parameters have been reported to influence inter-ply frictional behaviour, coefficients of which are typically much higher than those for tool-ply friction [108]. Sourki et al. [109] examined the inter-ply frictional behaviours of a thermoplastic prepreg, and found that both static and dynamic coefficients of friction were statistically dependent on both lay-up orientation and applied normal load, despite the inclusion of a lubricating resin. This anisotropic behaviour is also exhibited by dry fabric yarns at the mesoscale [117–119], where it has been shown that the surface topography of both mesoscale yarns and microscale filaments causes the ply orientation to dominate frictional behaviour. Inter-tow angles close to 0° can produce coefficients of friction up to twice as high as those at 90° [120]. This is corroborated in work by Dutta et al. [121], who demonstrated large variations in coefficients of friction with fibre orientation combinations during the inter-ply sliding of UD prepreg. Tourlonias et al. [118] used a nanotribometer to measure coefficients of friction between individual fibres at a range of relative angles, finding that the coefficient decreases as the angle increases. In particular, a step increase in frictional forces were observed when fibres were interacting parallel to one another. Sugimoto et al. [122] observed that the kinetic friction of a single carbon fibre interacting with a fibre bundle was strongly affected by the compression stress due to changes in the packing states of the bundles.

Anisotropic and pressure-dependent frictional behaviour at the macroscale can be attributed to a change in contact area between the plies as the fabric deforms. Yarns and fibres are able to commingle and nest at low inter-ply contact angles [123] (discussed in more detail in section 2.5.2). Likewise, increased normal load increases the contact area between plies as the fabric deforms. As the area between the plies increases, the more microscale asperities from each ply are forced into contact with one another

[124]. This real contact area (referred to as A_{real}) is typically much smaller than the apparent contact area between two surfaces, reportedly up to 1:10,000 when considering contact at the nanoscale [125].

The influence of micro-asperities on the microscale contact and frictional behaviour of surfaces has been widely studied, such as in the early work of Greenwood and Williamson [126]. The mechanism of asperity contact is also what defines the difference between adhesion and friction of two interfaces, where the former is a measure of the tensile strength of micro-asperities, whereas frictional forces are created by their shear strength [127]. Additionally, changes in contact area between asperities is the cause of static and dynamic frictional behaviours. At the onset of sliding at the interface, asperities shear and deform and are subsequently replaced by new, smaller asperities [128], leading to a further reduction in A_{real} [129,130]. This reduction in area causes a drop in measured values of μ when in motion, defining the dynamic coefficient of friction (μ_d) [131]. However, as normal load is not borne by a directly proportional number of asperities (due to the non-linear deformation of the fibre bundles [84]), the frictional forces produced by the shear strength of the asperities will not be directly proportional to the applied load. Unlike relatively un-deformable materials, such as metals, the inter-ply coefficient of friction of a deformable fabric is subsequently dependent on the normal load applied to the sliding interface.

The consideration of asperities leads to the introduction of a generalised model of adhesion and friction as proposed by Derjaguin [132], often referred to as an extended Amontons' law [82,133], where A_{real} is defined as the real contact area between asperities:

$$F_t = \mu(N_0 + N) = \mu A_{real}(p_0 + p_n) \qquad (2.3)$$

In Equation (2.3), $p_n := N/A_{real}$ is an averaged normal pressure, and $p_0 := N_0/A_{real}$ is an adhesion parameter. Introducing a material specific critical shear stress, $\tau_0 := \mu p_0$, the equation becomes:

$$F_t = \mu N + \tau_0 A_{real} \qquad (2.4)$$

At low normal loads, the total frictional forces generated by the surface interactions (F_t) are dominated by the contribution from the second term in Equation (2.4), which is known as adhesion-controlled friction. At higher normal loads, the first term (the traditional Amontons-Coulomb law) dominates, and the friction can be considered to be pressure or load-controlled [134]. The influence of either case on frictional forces produced by a given scenario is highly material and scenario dependent [82]. Due to the relatively high loads that composite reinforcement materials are subjected to during preforming, this thesis will use the standard Amontons-Coulomb law to describe inter-ply frictional behaviour, which is common practice in similar friction focused studies.

2.5.2. Through-thickness compaction behaviour

Compaction and nesting behaviour of multi-ply laminates changes the fabric geometry and inter-tow voids [135], which not only affects the laminate permeability during moulding and the fibre volume fraction post moulding [123,136], but also the inter-ply frictional behaviour during forming. Nesting of fabrics is considered to be the intermingling of individual tows and fibres between plies in surface-to-surface contact with one another, changing the compressive response of the fabric stack [137].

Potluri et al. [138] defined nesting in terms of a "nesting factor", shown in Equation (2.5) (where t_s is the total thickness of a stack of n plies, and t_i is the thickness of an individual ply) which is a useful indicator to the level of inter-ply commingling during a compression stage.

$$NF = \frac{t_s}{\sum_{i=1}^{n} t_i} \qquad (2.5)$$

Nesting of adjacent plies has been examined in multiple contexts in the literature, but typically in the role of determining permeability and resin flow through woven laminates under normal load [123,135,136,138–141]. Yousaf et al. [135] used computed tomography (CT) to capture geometrical changes in a single glass fibre woven ply subject to transverse compression, using digital element methods. The high x-ray contrast between glass fibres and air produced high fidelity images under different levels of loading. It was found that an absence of intra-ply friction in the subsequent simulation caused greater tow deformation than observed in the experiment, as tows could more easily slide relative to each other. Follow-up work [139] used the same methods to examine meso-scale nesting in multi-ply dry glass fibre woven preforms. It was found that the degree of nesting has a significant impact on meso-scale geometry changes, which in turn affects laminate permeability.

A noteworthy study on fabric compaction behaviour is that of Robitaille et al. [123,141,142]. It was observed that as the number of plies in a stack increases, so too does its initial V_f, but the compaction stiffness decreases for both woven materials and random mats. It was also observed that relaxation responses decrease as the applied pressure rises. Viscoelastic stress relaxation of a wide range of reinforcement materials has been reported in existing literature [141,143–148], and is a phenomenon that

should be taken into account when considering any method of compaction characterisation.

In NCFs, nesting and compaction behaviours are highly dependent on material architecture and orientation. In work by Yousaf et al. [149], a biaxial $[0°/90°]_4$ NCF laminate exhibited a 14% thickness reduction at 600 kPa, whereas a $[\pm45°]_4$ laminate only produced a 4% reduction. This was attributed to the different stitching patterns and tow shapes of the two different NCFs. The influence of the fibre architecture and the layup sequence on the compaction of NCFs was also investigated by Grieser et al. [150,151]. The effect of a variety of material and process parameters on the compaction behaviour were reviewed, including number of plies, testing speed, cyclic compaction and stitching types. It was found that higher testing rates resulted in increased compaction resistance, and the alignment of stitches had an influence on compaction behaviour until the superficial density of the stack exceeded 300 g/m^2, where the deformation of carbon yarns became the dominant mechanism in dictating compaction behaviour.

2.6. Fabric forming defects

Semi-automated preforming of composite fabrics can regularly produce defects in the fibre architecture that would be traditionally removed by hand. These defects can reduce the strengths and stiffnesses of a finished component by up to 40% [152,153], and therefore understanding how specific deformation mechanisms can produce these undesirable defects is critical to mitigating their effect. Examples of some common defects found in semi-automated forming processes are shown in Figure 2.21.

Wrinkling
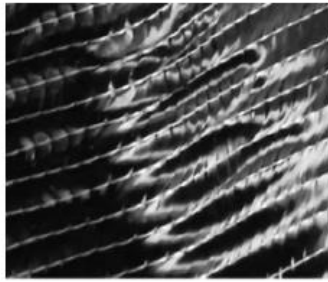
a) Macroscale ply folds   b) Mesoscale bundle loops
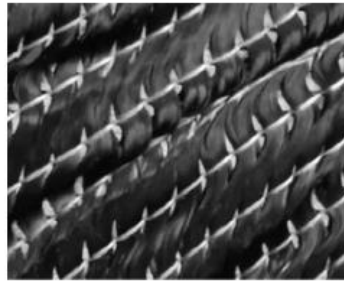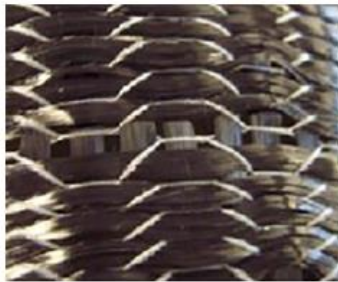
c) Laddering   d) Stitch damage
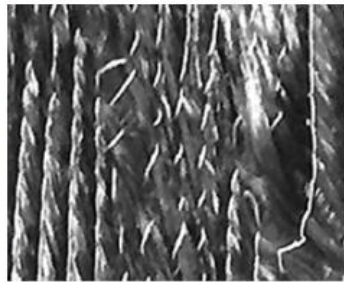
Figure 2.21 – Some common defects found when preforming dry composite fabrics.
Images from [43].

2.6.1. Defect modes

Arguably the most common defect mode [154], out-of-plane or macroscale
wrinkling (Figure 2.21a), typically occurs when local in-plane shear and
compressive stresses increase with shear angle [43], which is often used as
a measure of macroscale wrinkle initiation [66]. These stresses are then
dispersed as the fabric wrinkles out-of-plane when the shear locking angle
is reached, a region known as "over-shear". However, regions of high shear
do not always correspond with areas where defects are found [155] and
over-shear is not the only cause of macroscale wrinkling. High coefficients
of friction (both inter-ply and tool-ply) have been shown to generate local
regions of compressive strain, forcing the material to bend out of plane
[45,156–158]. In these cases, reducing the coefficient of friction was

observed to increase the formability of the preform. The material bending stiffness has been observed to be the driving factor of macroscale wrinkle amplitude and wavelength [159], so high quality bending characterisation is necessary when attempting to predict ply folds with accuracy. The severity of these large wrinkles can also be dependent on processing parameters, such as tool geometry [160,161], implying that material parameters alone (such as shear angle) may not always be sufficient to accurately predict macroscale ply folds.

Mesoscale wrinkling, sometimes known as bundle looping, is produced when yarns experience longitudinal compressive loads [43]. Depending on processing conditions, this load can either generate out-of-plane fibre bundle loops (if there is insufficient normal load to constrain the tows in-plane), or in-plane fibre waviness (if the normal load is adequate) as shown in Figure 2.21b. Research has shown that regions of negative shear are more likely to produce in-plane fibre waviness in biaxial NCFs, since the stitch yarns are subjected to compressive forces. Tensile loading of the stitches in the positive shear regions tends to resist further deformation, preventing in-plane waviness from occurring [160]. Mesoscale wrinkling can be mitigated by applying tensile loads to the system to reduce the magnitude of compressive loads in both diaphragm [162] and matched tool forming [163].

Laddering defects (Figure 2.21c), also known as gapping defects, are generated by transverse tensile load, causing yarns to spread and open which can result in undesirable resin rich regions in a finished component [164]. Laddering behaviour is dictated by the mesoscale architecture of the fabric, and the localised tool-ply, inter and intra-ply frictional forces that inhibit one fibre direction from moving relative to the other [165]. Tensile strain and stress along the principal fibre directions can be used as a measure or predictor of the likelihood of laddering occurring [43].

Stitch damage or rupture (Figure 2.21d) is a defect unique to NCFs (as woven fabrics are not stitched). It occurs in positive shear regions when the stitch fails under tension, causing areas of the fabric to then severely over-shear [62]. Stitch failure does not necessarily affect the mechanical properties of a finished component as the behaviour of each primary yarn is unaffected [43]. Instead, constraints on each yarn are relaxed, reducing stability and allowing for additional translation and rotation, increasing the likelihood of other defect modes occurring.

Poor tool conformity (fibre to tool bridging, see Figure 2.22) is almost entirely dictated by frictional forces present within a forming process. Friction prevents material draw in, either at tool-ply, tool-diaphragm or ply-ply surface interfaces, reducing conformity to the tool surface [43]. The distance between the preform and the tool surface is typically used to quantify bridging, a metric that can also be used to measure out-of-plane wrinkling defects. However, the principal difference between wrinkling and bridging defect formation is the tensile forces that are needed for the latter to occur, as opposed to compressive forces [44].
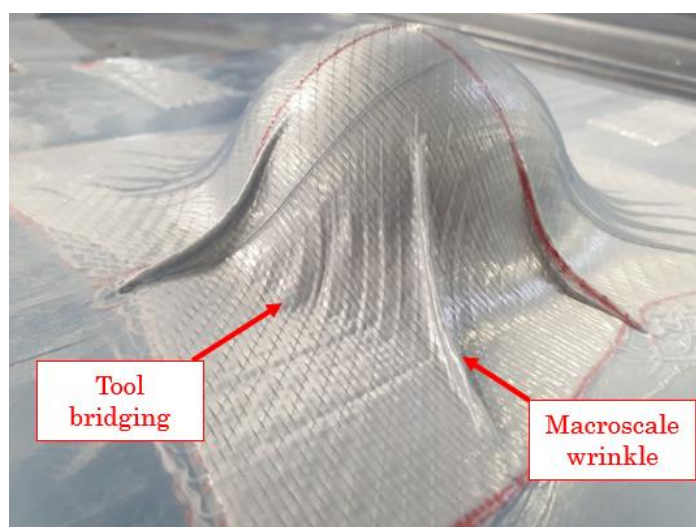
Figure 2.22 - Example of a glass fibre NCF hemisphere preform, produced using DDF, exhibiting tool bridging and large macroscale wrinkling defect modes.

2.6.2. Influence of the forming process on defect formation

The principal process parameter that causes differing defect modes in matched tool and diaphragm forming is the normal load applied to the surface of the fabric blank during the material draw-in stage. Through-thickness fabric compaction is limited to 1 bar (vacuum pressure) during diaphragm forming, much lower than that of a matched tool equivalent. A comparison between the two methods [42] demonstrated how the reduced constraints in DDF enables local thickening of the material when shearing, reducing out-of-plane buckling relative to a matched tool forming process. As the larger compressive loads in matched tool forming inhibit the change in thickness that arises with shear close to the locking angle, both woven and NCF fabrics are more likely to buckle out of plane [166]. However, tool bridging defects are much more common in DDF, as once again the draw-in forces are limited by vacuum pressure [44].

2.7. Material characterisation methods

A broad range of techniques exist to characterise the deformation modes of different textile materials subject to different processing conditions. Consequently, few of these methods have been standardised [167] and their results must be carefully considered.

2.7.1. Shear characterisation methods

Existing literature most commonly presents two different methods for characterising in-plane shear behaviour – the bias extension test and the picture frame shear test.
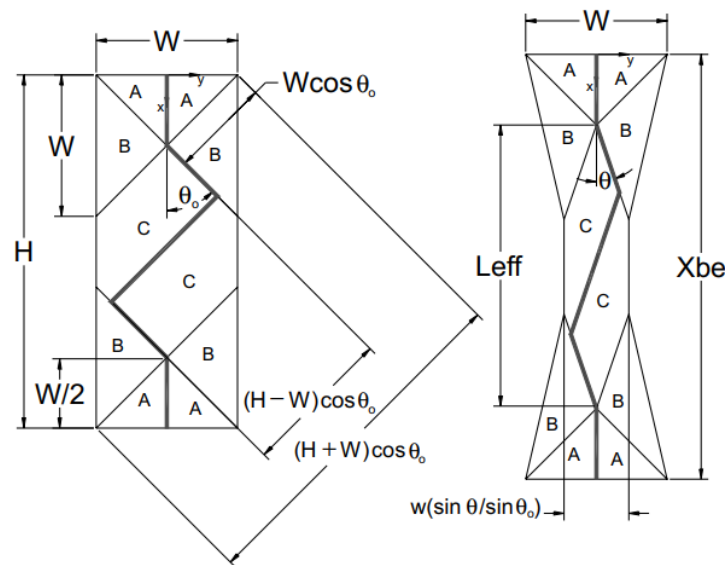
Figure 2.23 - Schematic of undeformed (left) and deformed (right) bias extension test, highlighting three distinct shearing zones labelled A, B and C [168].

The bias extension test is conducted using a rectangular fabric sample (with an aspect ratio of 2:1 or greater), constrained along its short edges. The fibre orientations are at ±45° to the loading direction [167], to avoid direct tension in the fibres. Similar to a uniaxial tensile test, a constant displacement is applied to the upper edge and the force required is recorded. Digital image correlation (DIC) is used to accurately measure shear angle in the ROI during a bias extension test [167,169–171]. Lebrun et al. [168] describe a method of calculating the global shear angle based on the assumption of three distinct areas of shear, as shown in Figure 2.23. Zone A is assumed to have zero shear, Zone B is an intermediate shear region and Zone C is subject to pure shear. The shear force is calculated using the same assumptions, and can be derived using a kinematic analysis [167].

The picture frame shear test uses a specialised trellis fixture to induce homogeneous, pure shear in the ROI of a fabric sample, as shown in Figure 2.24. The samples are clamped on 4 sides at a ±45° orientation to the

loading direction (labelled *F*). In practice, the 4-sided frame means only orthogonal biaxial fabrics (woven or NCF) can be characterised using the picture frame test, as otherwise the pure shear region may not be fully isolated from any tensile components. Care must be taken to maintain a constant tension through the fabric when clamping across samples, as this can have a significant effect on the final shear behaviours observed by inducing a tensile force component [172]. A constant vertical displacement is applied to the upper corner of the trellis frame, causing the fixture and affixed sample to shear in-plane. Results are then normalised using a variety of methods in order so to compare against picture frames of differing geometries [167].
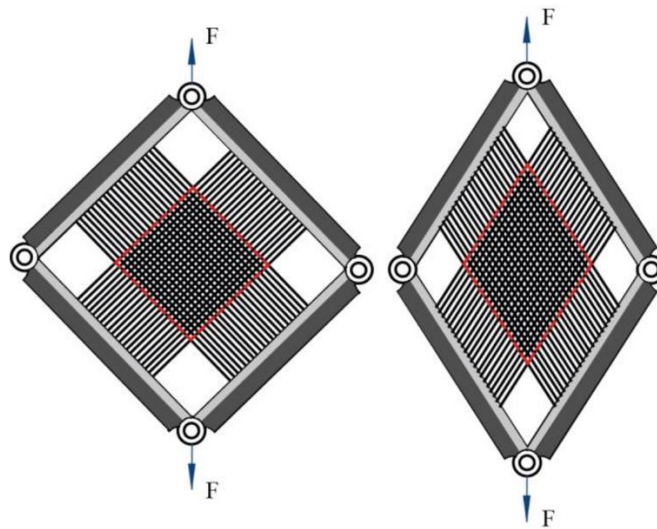
Figure 2.24 - Schematic of picture frame test undeformed (left) and deformed (right) [173]. The ROI subjected to pure shear is highlighted in red.

Numerous comparisons between these two principal shear characterisation tests can be found in existing literature. Harrison et al. [174] claimed that the deformation mechanisms generated in picture frame tests are closer to those experienced during actual component forming, but argue that the bias extension test is a rapid and robust method of

determining locking angle. However, above certain shear angles (~35° for a thermoplastic prepreg) the bias extension test is more liable to inter-tow slip and the ROI is no longer subject to pure shear. Additionally, the high likelihood of out-of-plane wrinkles forming in the bias extension test can further limit the range of shear angles for which it is valid [71]. Likewise, the picture frame test is not without its drawbacks. It is particularly sensitive to fibre misalignments when mounting samples in the frame, so higher accuracy is required when cutting and mounting material [175].

Taha et al. [176] conclude that results obtained from both methods are comparable when normalised, but suggest that where the bias extension test presents a simple and fast experimental procedure with more complex post-processing, the picture frame test is more time consuming but generates pure shear deformations.

In summary, selection of the most appropriate shear characterisation method should be undertaken on a case-by-case basis, considering both material and process parameters, ease of use, and the ultimate goals of the experiment.

2.7.2. Bending characterisation methods

The most common methods for characterising the bending stiffnesses of composite reinforcing material are the cantilever bend test [71,73,177], the Kawabata Evaluation System (KES) [72,178,179] and multi-point bending tests. Each have their benefits but are likely to be more appropriate for a given material or load case.

A cantilever bend test typically uses gravity to generate a bending moment in a fabric sample of known dimensions and is the subject of two testing standards (ASTM D1388-14 and BS EN ISO 9073-7). In the conventional experiment, normally used to measure stiffnesses of materials with linear bending behaviour, a specimen is placed on a flat surface with a ruler on

top, as shown in Figure 2.25. The ruler and specimen are slid forward, over the edge of the surface, until a specified deflection angle (ϕ) in the specimen is achieved. The overhang length is noted using the ruler, enabling calculation of a constant linear bending stiffness.
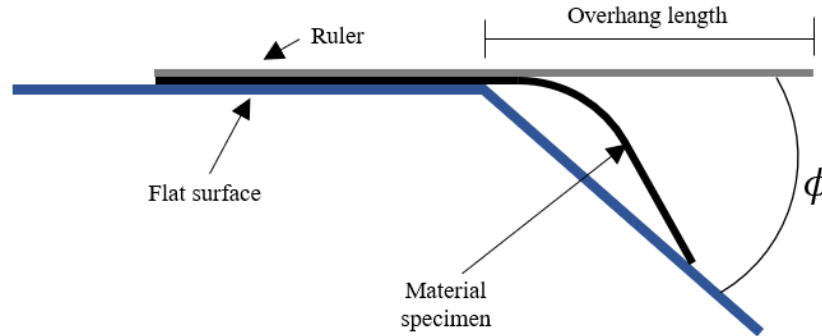
Figure 2.25 - Schematic of a traditional cantilever bend test as devised by Peirce et al. [177]. Image adapted from [71].

To characterise non-linear bending stiffness, such as that exhibited by NCF materials, the cantilever bend test can be adapted to digitally capture the full bending profile of the fabric specimen. This has often been accomplished using two-dimensional imaging methods (i.e., cameras) [72,73,76], but also with three dimensional laser scanning [71]. The non-linear bending behaviour is typically described using a plot of curvature κ versus bending moment M, from which the bending stiffness (Equation (2.6)) can also be determined.

$$EI = \frac{M}{\kappa} \tag{2.6}$$

A KES bending test uses a specific bending meter (known as KES-FB2) to characterise both standard bending and recovery behaviours. The parameters that can be evaluated from the resulting bending chart include

bending modulus and hysteresis width [179]. The immediate disadvantage of KES-FB2 compared to a cantilever bend test is the need for a specialist and complex flexure rig to perform the experiment, so the KES method is less common in the literature.

Multi-point bending tests, such as the three and four-point bend tests, apply a bending moment using an automated mechanism, usually a universal testing frame. They require sufficiently large bending rigidity of the specimen [180] and so are only employed to characterise the bending behaviour of stiffer materials, for example resin cured composites [181,182], and not normally dry fabrics.

2.7.3. Friction characterisation methods

Characterisation methods of frictional behaviour within a forming process are highly dependent on the scale at which the frictional forces are being considered (i.e., micro, meso or macroscale). Since the macroscale frictional behaviour is dictated by the micro and mesoscales, it is important to understand how to measure frictional forces across a wide range of scenarios.

When using low loads with individual fibres at the microscale, adhesive properties of individual fibres are significant and an extended Amontons' law (Equation (2.4)) becomes more relevant. One method to characterise friction between fibres is by suspending a single tensioned fibre in a carrier, and then applying a small load (< 0.1 N) between two carriers before sliding to generate a frictional force [118,183]. Figure 2.26 shows an example setup in a nanotribometer, investigating the influence of fibre angle on fibre-fibre friction. The fibres are tensioned to around 0.15 mN and glued in place on the carriers.

Sugimoto et al. [122] used pull-through test to determine kinetic coefficients of friction, whereby a single fibre was placed on a paper

template and pulled between two fibre bundles. Once again, the forces involved were very low, in the order of a few mN, and a custom testing apparatus was used.
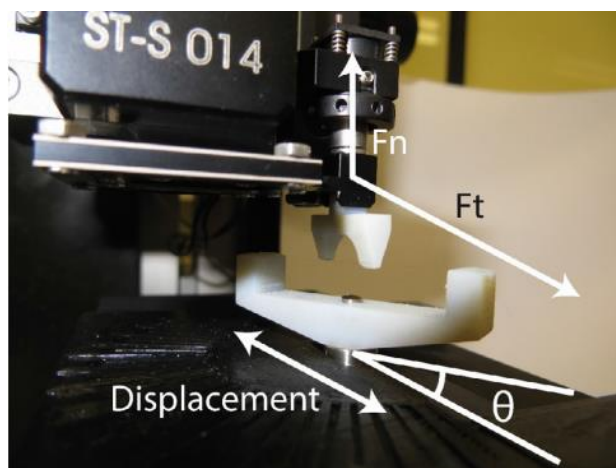
Figure 2.26 - A nanotribometer friction testing rig with two single fibre samples at a relative inter-fibre angle of 45° [118].

Meso and macroscale friction characterisation is more prevalent than microscale in the literature, partially because the tests are less complex than when observing single fibre interactions. Existing tests tend to be common at both scales and take one of 3 forms: sled tests, pull-out or pull-through tests, and capstan tests.

The sled test is the simplest of the three; evidence exists of the test originally being developed by Leonardo da Vinci in the $15^{th} - 16^{th}$ centuries [184], and little has changed since then. A relative motion is induced between material affixed to a stationary base plate and a weighted sled, ideally through the use of a line with very high axial stiffness. The force required to move the sled is recorded, and an Amonton-Coulomb friction law ($F = \mu N$) is used to calculate the coefficient of friction between the two surfaces. The sled test was previously standardised for use with plastic film

and sheeting (ASTM D1894-14 [185]), but it was withdrawn from circulation in March 2023 and has not been reinstated at time of writing. An example test set up is shown in Figure 2.27.
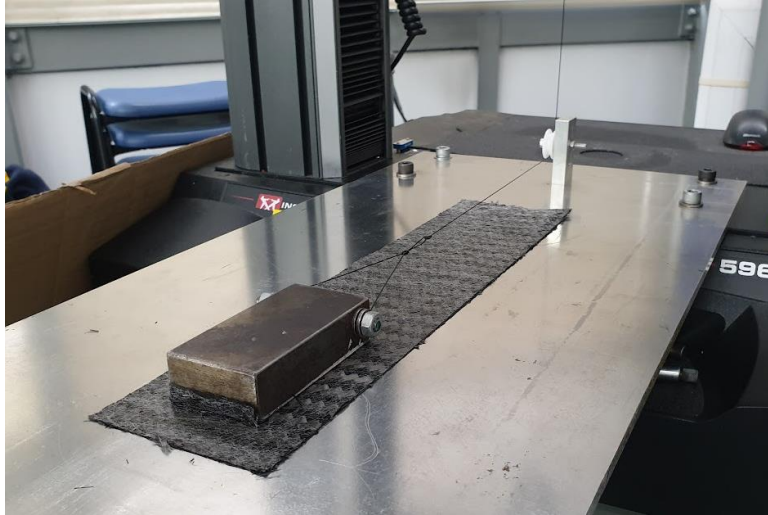
Figure 2.27 - Image of a typical sled test setup, measuring frictional forces between two samples of dry woven carbon fibre fabric reinforcement.

A significant disadvantage of the sled test is its maximum weight capacity. As mass is added to the sled and frictional forces increase, the tow cable is subject to increased strain, subsequently invalidating the load measurement. Additionally, the test is very liable to stick-slip motion, causing large oscillations in frictional forces that are not present in actual manufacturing processes [186]. This makes it a suboptimal test for calculating coefficients of friction of deformable materials over a range of pressures, as the results become less reliable as pressure increases. Despite this, the sled test can be found in friction studies of composite fabrics for both inter-ply and tool-ply interactions [45,84,117].

Pull-through and pull-out friction tests [78,92,187–189] use the same principle – a material specimen (sometimes supported by a scaffold) is

clamped between two platens, upon which more material samples are affixed (Figure 2.28). A load is applied normal to the surface of the platens, typically using a hydraulic or pneumatic cylinder for precise load control [78], but the use of calibrated springs is not uncommon [190]. The difference between a pull-out and pull-through test is one of relative sample size – in a pull-out test the central samples are shorter than the outer, so that they are pulled out of the clamping region (as shown in Figure 2.28). In a pull-through test, the central samples are much longer than the outer samples, so that when a relative displacement is applied a constant supply of material is moved through the clamps. In general, a pull-through test provides more reliable results as the influence of any edge effects of the specimen are eliminated.
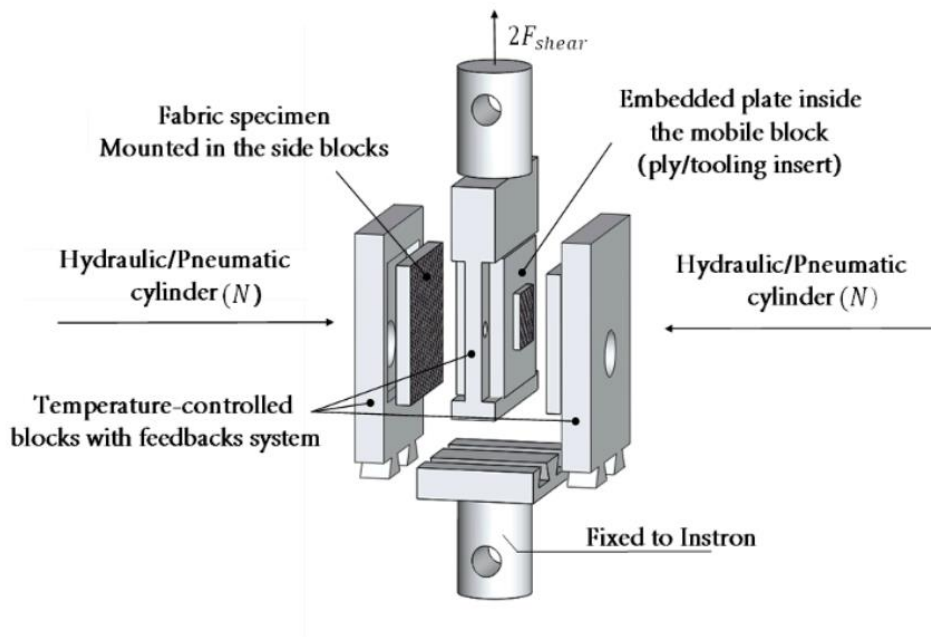
Figure 2.28 - An example schematic of a pull-out friction characterisation test using actuated normal load [97].

Pull-through tests are adaptable to a range of normal loads (and temperatures if platens are heated) but do have some drawbacks. There is

no testing standard at the time of writing, making comparison between tests difficult. Additionally, the test itself requires a custom-made rig, which does not usually have any method of containing fluids, such as resins if the fabric is saturated, or additional surface modifiers included in the test.

1: Fibrous tow specimen (with tow ends a and b)
2: Rotating metal drum with shaft ends
   (supported by ball bearings on both sides; ⌀ 12 mm shaft)
3: Coupling: KTR BoWex M 14 double cardanic coupling
4: Motor-gearhead combination
   (Maxon RE35-118778 / Maxon GP 42C-203129)
T_1: Force in tow end b (pre-tensioned or dead weight loaded)
T_2: Force in tow end a (clamped in a load cell)
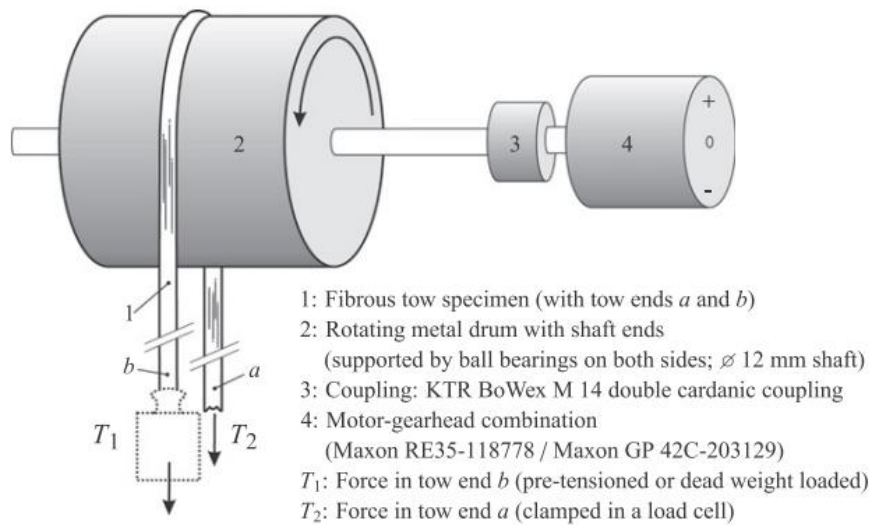
Figure 2.29 - Schematic of a capstan friction test for fibrous tows [191].

Capstan friction tests are arguably the least common of the main friction tests and are typically reserved for mesoscale characterisation. As shown in Figure 2.29, a tow specimen is draped over a drum and tensioned at either end. The drum is rotated about a centrally aligned shaft, and resistance to its motion is generated by frictional forces from the tow. The apparent coefficient of friction can be calculated as a function of the tensional forces and the wrapping angle of the tow around the drum.

Capstan tests have been used for both tool-tow [191] and ply-tow [119] dry friction characterisation. The rotational motion of the capstan makes it an ideal test for measuring wear on textile materials [192], as the sliding

distance has effectively no limit (particularly for tool-tow tests) and can be carefully controlled. Cornelissen et al. [119] found that the capstan results were comparable to that of a sled test. In this case, the limiting factor of the normal load is the tensile strength of the tow and its attachments, which is likely to be dependent on the test set-up. Additionally, the drum material needs to be changed to account for any different surface pairings, which is inconvenient when considering the influence of many different parameters.

In summary, each friction test set-up has its merits, but none seem entirely capable of characterising a composite fabric under conditions fully representative of a preforming process. To improve understanding of the macroscale contact behaviours, friction must be carefully isolated and tested under temperature, pressure and slip rates closely depicting a specific process. Additionally, underlying micro and mesoscale mechanisms must be separately investigated to fully appreciate component-scale frictional behaviour.

2.7.4. Tensile characterisation methods

Tensile characterisation of composite fabrics is typically undertaken in either uniaxial or biaxial loading cases. In a uniaxial tensile test, fabric samples are clamped at both ends, usually in the principal or transverse fibre directions (depending on the material being tested). A displacement is then applied to the specimen, usually with a universal testing frame, and the load required is recorded.

Biaxial loading is especially preferable for woven fabrics, as non-linear stiffening caused by de-crimping of yarns under uniaxial load can affect tensile behaviours in the secondary fibre direction [101,102]. For a biaxial tensile test, fabric samples are produced in an X configuration by removing transverse yarns where not required. The central square region where both

yarn directions are present is considered to be the region of interest (ROI), as can be seen in Figure 2.30. A range of tensile loads can be applied in both fibre directions, and the fabric response is recorded to establish a "tension surface" to describe the behaviour. To fully characterise and understand the response of the material under tensile load, the ratio between the two loads can vary between zero and infinity so as to consider the influence of any asymmetry in the fabric architecture, such as stitching in a biaxial NCFs [193].
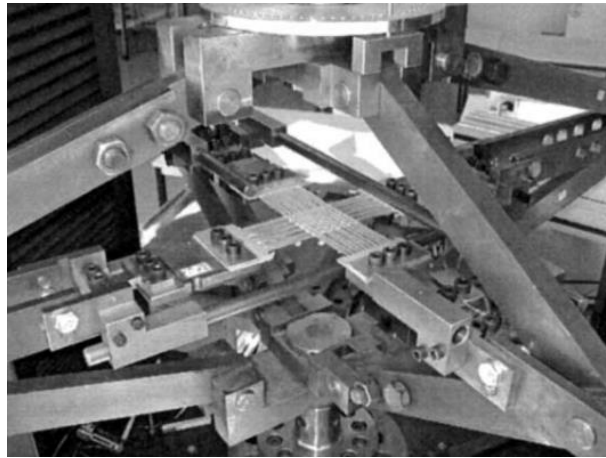
Figure 2.30 – A biaxial tensile test rig using glass fibre "X" shaped specimens [101].

It is difficult to accurately characterise transverse tensile behaviour of UD NCFs as the tensile response is highly dependent on the clamping conditions and sample sizes [61]. This behaviour is described in Figure 2.31, where the transverse stiffness is dominated by the tensile stiffness of the supporting glass fibres in the carbon fibre fabric when clamped, but the much weaker frictional force generated between the carbon and glass fibres if they are not.
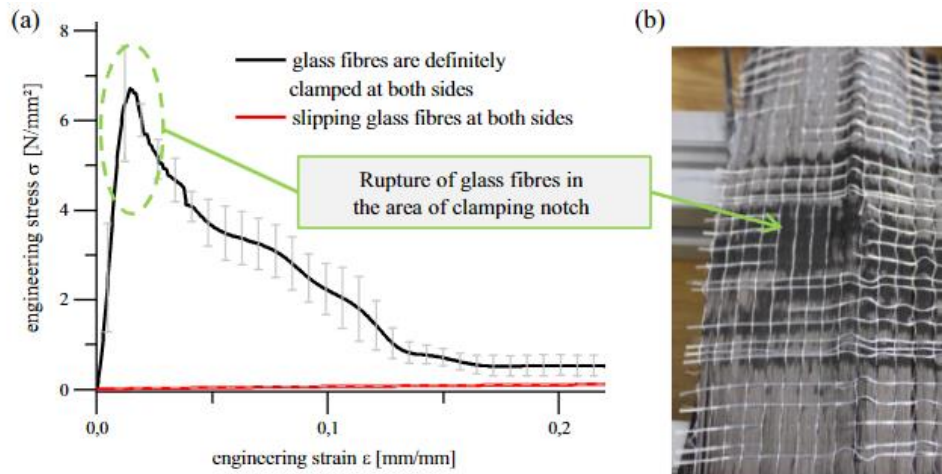
Figure 2.31 - Transverse tensile behaviour of a carbon fibre UD NCF [61].

2.8. Fabric forming simulations

The final section of this literature review will briefly consider forming process simulations for composite fabrics. Whilst the aim of this thesis is not to construct entirely new simulation tools, it is still important to understand their structure and capabilities in order to effectively facilitate their use.

2.8.1. Kinematic models

Kinematic modelling is a relatively computationally inexpensive method of simulating fabric draping behaviour that does not consider any physical properties or boundary conditions [194]. Instead, kinematic draping simulations (KDSs) use geometric approximations to make predictions of draping behaviour, improving run time at a cost of severely reduced accuracy [195].

A KDS considers a textile fabric to be a pin-jointed net of inextensible rigid bars, and as such it can only deform using an in-plane shear mechanism

[196]. As a result of this, defect prediction can only be estimated via comparison of local shear angles to a pre-determined shear locking angle. "Mapping methods" [197] are used to fit the two-dimensional net to a three-dimensional tool geometry, as shown in Figure 2.32. A popular mapping method is known as the fishnet algorithm [198], which can be conducted very quickly but considers yarn paths between nodes to be a straight line, causing reduced accuracy.
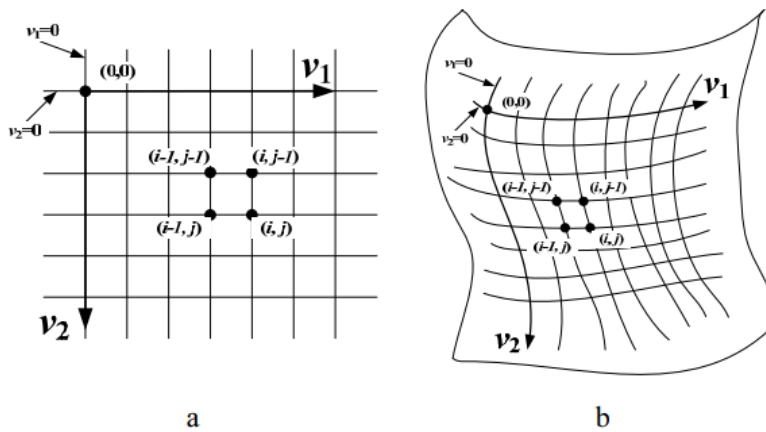
Figure 2.32 - An illustration describing fabric mapping methods – a: undeformed fabric blank. b: Fabric mapped to a geometric surface [198].

In particular for this thesis, critical disadvantages of KDSs is their inability to consider any friction or compaction mechanisms during a forming process [197]. When considered alongside their relative inaccuracy compared to FE methods [199], this makes them unsuitable to predict the forming response of multi-ply-based preforms, despite their relative computational efficiency. Therefore, KDSs will not be pursued further as a method of analysing forming behaviour of multi-ply preforms in this work.

2.8.2. Finite element models

As commercial computational power has advanced, the popularity of utilising three-dimensional FE models for fabric draping and forming simulations has increased. FE methods enable the physical properties of the material and process parameters to be considered through the use of numerical modelling. As a result, they are much more computationally expensive than a KDS, but can consider non-linear effects derived from anisotropic material behaviour, as well as inter-ply interactions such as friction [200].

Fabric forming is a quasi-static process, and so can be simulated either implicitly or explicitly [201]. Implicit modelling requires the solving of a system of non-linear equations using a direct integration method, considering the entire time step simultaneously. This means that the time increment is not restricted by stability conditions, allowing for larger time steps to be used. However, convergence difficulties caused by deformation are common, reducing the stable time increment. Therefore, implicit analyses are not ideal for more complex forming simulations [200].

The same deformations do not produce convergence issues in explicit methods, which updates the solution incrementally. The solution to each time step depends on the solution of the previous, the size of which is limited by material properties and is significantly smaller than that of an implicit analysis. Mass scaling is often applied to increase the time step size, by artificially increasing the mass of elements in the system. However, mass scaling should be used with care, as changes to the global mass can cause erroneous results [202].

2.8.3. FE modelling scales

The scale of the system being considered by an FE model is critical to the modelling methods used. The main difference between micro, meso and

macroscopic simulations is one of geometry – how the fibres, yarns and plies (and their associated mechanical properties) are represented in a model.
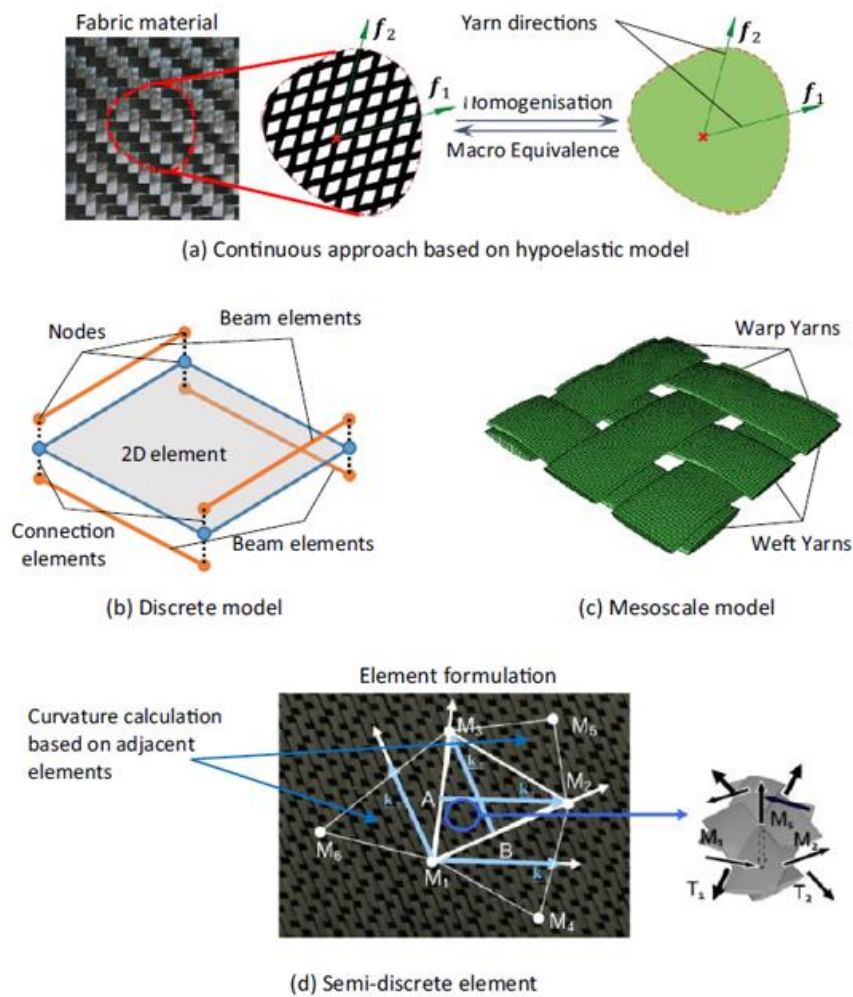
Figure 2.33 - Schematics of various modelling methods for 2D fabrics [200].

Microscale FE simulations consider fibres (or groups of fibres smaller than a yarn) to be individual components, typically modelled as deformable 3D beam elements [203]. Microscale modelling approaches are far from uncommon, but are considered out of scope for the purpose of this literature

review as the computational expense of using them at an industrial scale remains impractical [200].

Mesoscale (Figure 2.33c) FE methods consider each yarn as an individual component in a system, typically in the form of a periodic or repeating patterns of representative unit cells [204]. Stitches are sometimes included in mesoscale NCF models to accurately represent the fabric architecture [205]. Mesoscale FE geometries can be produced several ways, including manually modelling each yarn, reconstruction from CT data [204] or procedurally generated through a third party such as TexGen [53]. Mesoscale FE models are often used to accurately predict material behaviours, such as permeability [205,206], but not entire forming processes, as the precise geometrical descriptions required can be very computationally expensive [207].

The majority of FE forming simulations are undertaken at the macroscale [208] due to the decreased computation cost at component scale (but mesoscale forming models are not uncommon [209]). Mechanical properties are determined using the characterisation methods described in section 2.7, which can then be applied to a material model for use in the simulation using either continuous, discrete or semi-discrete element formulations [200]. A summary of the advantages and disadvantages of each approach can be found in Table 2.1.

The continuous approach (Figure 2.33a) has been widely used in forming simulations due to its ability to be implemented without the need to modify element formulations. Using homogenised material models to represent fabric plies can reduce computational time but typically cannot be used to represent meso or microscale mechanisms. Continuum models can be implemented in the form of a hyper or hypoelastic model to track non-orthogonal material deformation, which is necessary for accurate prediction of material responses [210].

A discrete macroscale approach [211,212] (Figure 2.33b) is essentially a large mesoscale analysis, where each yarn is described by simplified 1D beam or spring elements. This produces a very large number of components (and contacts between them), becoming very computationally expensive. As a result, discrete element formulations are not a popular solution in FE forming models. Similar to a fully discrete model, a semi-discrete model is also formulated from a mesoscopic approach, considering yarns as individual components [213]. A semi-discrete approach (Figure 2.33d) determines the component strain from the nodal displacements, leading to numerically efficient elements. Additionally, yarn directions are independent from the edge of the element, allowing for implementation of non-linear bending behaviour. However, this approach requires specialist element formulations that are not commonly found in commercial FE software packages [200].

Table 2.1 - Advantages and disadvantages of typical FE model approaches [200].

Modelling approach	Advantages	Disadvantages
Continuous approach	• Small number of DOFs • Applicable to classical FE model	• Requirement for specialised constitutive model • Cannot model deformation characteristics or defects at mesoscale
Discrete or mesoscopic model	• Close to the natural architecture of fabrics. • Can model the interaction between yarns and stitches • Can model occurrence of mesoscale defects	• Large number of DOFs • Limited to small structures • Needs specialised homogenisation procedure to determine material parameters in numerical model
Semi-discrete element	• Small number of DOFs • Applicable to classical FE model	• Needs specialised element formulation • Not readily available in commercial FE codes

2.8.4. FE process modelling

Full-scale forming processes such as DDF or matched tool forming are typically modelled using either membrane, shell elements or a combination of both [200]. Membrane elements are a popular choice [155,214–216] due to their reduced number of degrees of freedom, which reduces computation time. However, their principal drawback is that they neglect the bending stiffness of the fabric ply as they typically have translational degrees of freedom at each node, but not rotational. This produces results that give a good indication of shear behaviour (which can indicate likely defect areas) but cannot accurately determine the shape or size of wrinkles [155]. Some models combine the use of membrane elements with other element types to improve the quality of the simulation, such as those developed by Lin et al. [217] which uses additional truss elements to represent high tensile stiffnesses.

Shell elements are better placed to predict wrinkling defects due to their consideration of bending stiffness, giving a more accurate prediction of wrinkle amplitude and length [159] as well as tool bridging [218]. Shell models are often more computationally expensive than their membrane equivalents, as high-resolution meshes are necessary to ensure accuracy and small time increments are required to maintain stability. Boisse et al. [219] note that as classical plate and shell theories do not apply to composite fabrics, it is necessary to decouple the in- and out-of-plane stiffnesses. Additionally, using accurate non-linear bending data in a shell model produces more accurate wrinkle predictions, as shown in Figure 2.34 [74].
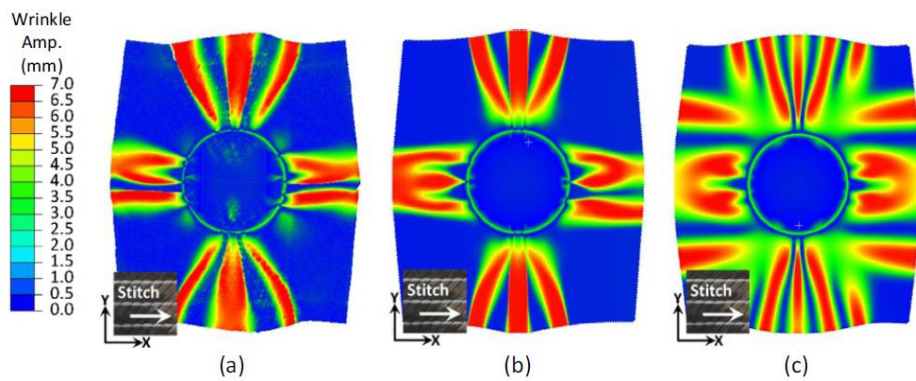
Figure 2.34 – Comparison of wrinkle patterns for a) experiment, b) Non-linear bending model and c) constant bending stiffness [74].

Since the fabric bending stiffness is much lower than the tensile stiffness, most commercial FE software cannot reproduce accurate bending behaviour, since the bending stiffness is calculated from the axial moduli of the ply [74]. Therefore, models that employ coupled membrane and shell elements are increasingly used to decouple the bending stiffness from the tensile stiffness [220–224]. These models often use layers of elements, as shown in Figure 2.35, employing very thin shell elements to account for the bending behaviour and lower-order elements to account for the in-plane behaviour to more closely resemble reality. Alternative solutions can be found in the development of specially formulated elements [225], but these are often complex to apply and may not be compatible with commercial FEA software.
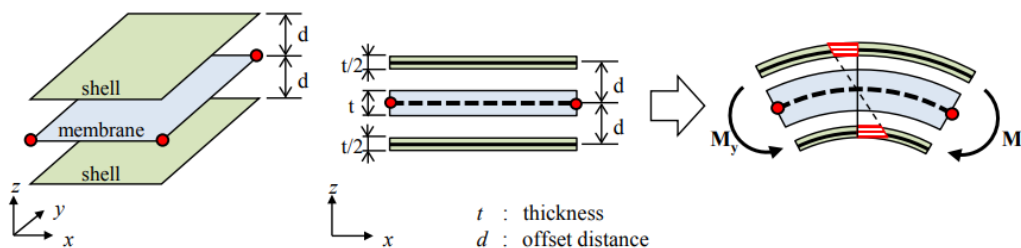
Figure 2.35 - Shell-membrane hybrid model for dry textiles [224].

2.8.5. Friction in multi-ply forming simulations

Simulating a forming process for laminates consisting of two or more plies increases the complexity of the simulation, not only because of the increased number of elements and contacts involved, but because the likelihood of defects is larger when compared to forming single layers (particularly when the plies have differing orientations) [45,108,114,226]. Modelling surface interactions precisely can be computationally expensive, and the main methods being node-to-node contact [227] and surface-to-surface contact [228], and occasionally specialist contact elements. These approaches tend to be similar across FEA packages, albeit with some minor differences.
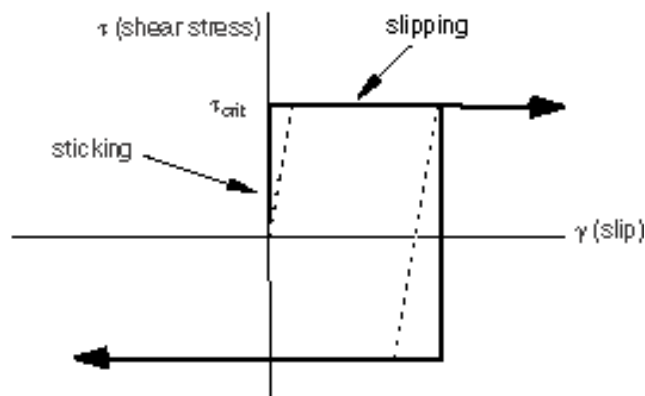
Figure 2.36 - Abaqus FEA Coulomb frictional behaviour [229].

Overwhelmingly the most common method of including frictional behaviour in process modelling is using the standard Amontons-Coulomb friction law to calculate frictional shear stress between contact pairs. Each contact pair is comprised of a primary (master) and secondary (slave) surface, the former of which generates contact forces. In Abaqus FEA, stick-slip Coulomb friction is implemented by disabling any relative slip until the shear stress across the interface is equalled or exceeded, as

summarised in Figure 2.36. It is possible to manually define more complex frictional behaviour in some FE software packages, such as through the use of a VFRIC or VFRICTION user-defined subroutine in Abaqus/Explicit [230] and USRFRC in LS-DYNA [187].

2.9. Chapter conclusions

To manufacture structural composites at volume using LCM processes, a forming stage is required to transform a two-dimensional fabric blank into a three-dimensional preform. In a semi-automated preforming process, such as DDF, this can often induce defects within the fibrous preform, such as wrinkles. Understanding the mechanisms that cause these defects to arise is critical to their prediction and mitigation, and these mechanisms are highly dependent on material architecture.

Biaxial NCFs will be the principal materials used for this study due to the recent surge in interest from industry. The single-ply shear, bending and tensile behaviours of biaxial NCFs are thoroughly researched and well understood, however, the role of multi-ply deformation mechanisms (compaction and friction) on the formability of thick structures are less well known. Several studies have observed that reducing inter-ply coefficients of friction by using lubricants can improve preform formability, but the inclusion of additional non-structural material into a composite is undesirable, as is introduces additional steps into an LCM manufacturing process.

Forming studies of NCF laminates consisting of many plies are found infrequently within the literature, generating an as-yet-unanswered question for forming of thick structures – how does non-Coulomb frictional behaviour in an NCF laminate affect its formability? To answer this primary research question and understand its implications, several others must be asked:

1. What are the mechanisms that dictate inter-ply frictional behaviour, and how are compaction and friction behaviours of NCFs connected?

2. How does inter-ply friction affect the bending and shear behaviours of a dry multi-ply NCF laminate?

3. Can friction induced defects be mitigated without the use of lubricants?

4. What does a predictive FE model need to consider to more accurately model NCF friction, and what is the significance of this accuracy?

The ensuing chapters will attempt to answer these questions using a variety of experimental and modelling techniques, including material characterisation at the macro and mesoscales, coupon-level and full-scale experimental forming studies, coupled with FE simulations.

3. Characterisation of macroscale frictional behaviour

3.1 Chapter outline and research aim

This chapter aims to understand the macroscale (ply level) frictional behaviour of biaxial non-crimp fabrics (NCF)s when subjected to compaction loads representative of a double diaphragm forming (DDF) process. To achieve this research aim, a method for characterising the macroscale frictional behaviour of composite fabrics subject to compaction loads up to vacuum pressure is presented. Referred to as an overlap friction test, this method is used to investigate the effect of applied normal force and inter-ply fibre orientation on the frictional behaviour of biaxial NCFs. It is demonstrated that the frictional forces generated by fabric-fabric interactions are highly dependent on both normal load and fibre orientation, a phenomenon driven by the compaction behaviour of a dry laminate.

3.2 Chapter methodology

The first section of this chapter will describe the materials used and introduce the testing methodologies employed to characterise the macroscale inter-ply frictional behaviour and a study to contextualise the characterisation results in an actual forming scenario.

3.2.1 Materials

The primary NCF material used in this thesis is a polyester pillar stitched biaxial fabric designated FCIM359, provided by Hexcel Reinforcements, Leicester UK. The relevant material properties of FCIM359 are shown in Table 3.1. Samples of FCIM359 used for the tests in this chapter were prepared and cut by hand using a rotary cutting knife.

Table 3.1 – Material properties of FCIM359.

Name	FCIM359	
Supplier	Hexcel	**Fabric surface**
Fabric type	Biaxial NCF	
Areal weight	441gsm	
Fabric thickness	0.4mm	
Stitching	Polyester pillar stitch, 4.5mm spacing	
Fibre	24k carbon tows	
On-roll fabric orientation	Stitch 0°, fibre ±45°	

Inter-ply friction characterisation tests were performed over a range of ply orientations and normal pressures. The nomenclature for capturing these parameters is described in Table 3.2. Whilst FCIM359 is a biaxial NCF, only the fibre bundle orientations and the fabric-fabric contact interfaces are considered for the naming convention. Interfacial fibre angles are used to name each interaction according to a clockwise positive direction when viewed from the front face of the test packet (as designated by yellow lines in Table 3.2) relative to the direction of sliding (as designated by red lines in Table 3.2). The direction of the polyester pillar stitching is also relevant to the results of the overlap friction test and are always 45° out of phase with the fibre angles (i.e., the stitch angle of the first ply is -45° from the fibre direction, and the stitch angle of the second ply is +45° when in face-to-face contact).

Table 3.2 - Example surface interactions and corresponding nomenclature for the friction characterisation tests.

Schematic of inter-ply interface	Laminate layup	Nomenclature (fibre angle at inter-ply interface)	Stitch angle at inter-ply interface	Inter-ply fibre orientation
	[+45/-45//+45/-45]	[-45°/45°]	0°/ 0°	90°
	[90/0//0/90]	[0°/ 0°]	-45°/45°	0°
	[90/0//+45/-45]	[0°/ 45°]	-45°/ 0°	45°

The vacuum bag material used in the overlap friction test was VACflexP, a nylon bagging film in a "sock" format (i.e., factory sealed along both long edges) typically used for vacuum infusion of long, narrow composite components. The VACflexP material was purchased from VAC Innovation UK, and the relevant material properties can be found in Table 3.3.

Table 3.3 - Material properties of VACflexP [231].

Name	VACflexP
Thickness	0.05 mm ± 10%
Density	1.13 g/cm^3
Tensile strength Machine direction	95 MPa ± 10%
Tensile strength Transverse direction	90 MPa ± 10%
Elongation at break Machine direction	320 % ± 10%
Elongation at break Transverse direction	370 % ± 10%

3.2.2 Overlap friction test methodology

During DDF processes, vacuum pressure is applied normal to the tool surface, often producing undesirable compressive forces that inhibit inter-ply fabric sliding where it is required to produce a high quality preform. This out-of-plane compression consolidates the laminate stack, changing the surface topography of each ply at the inter-ply interfaces.

A sled test (ISO 8295:1995 and ASTM D1894 [withdrawn at time of writing]) was considered unsuitable for effectively capturing the frictional behaviour when subjected to representative compaction loads, due to the generation of undesirable stick-slip behaviour and strain in the testing apparatus. As shown in Figure 3.1, stick-slip behaviour can produce very large oscillations in measured force which increase in severity as more load is applied to the sled, reducing the accuracy of the force recorded. Additionally, strain in the cable used to tow the sled leads to an inaccurate measurement of the static coefficient of friction, as shown by the progressive linear increase

before the vertical dashed line in Figure 3.1 (which also demonstrates minor stick-slip motion).
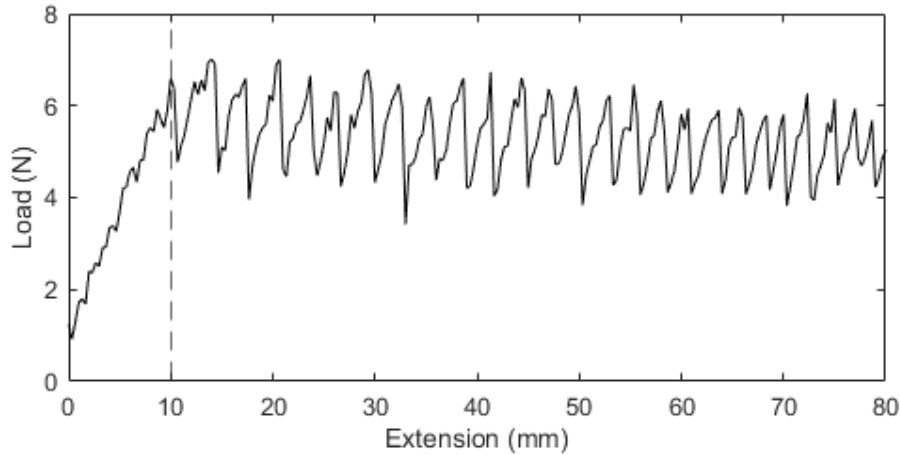
Figure 3.1 – Example of a frictional force versus extension graph of a 90° fabric-fabric FCIM359 interaction, produced using a traditional sled test with an additional mass of 2kg. Severe oscillations produced by stick-slip motion are exhibited.

The overlap friction test seeks to overcome the drawbacks of a conventional sled test so that in-situ inter-ply frictional behaviour can be characterised effectively. As with diaphragm forming, the test uses vacuum pressure to generate a normal load over one or more surface interactions. Similar to existing ply pull-through or pull-out tests, fabric samples are affixed to opposing faces of rigid support plates (as shown in Figure 3.2a), using 3M double-sided adhesive tape, the shear strength of which was observed to be considerably higher than the transverse shear strength of FCIM359. A maximum load of 2.7 kN was observed when conducting the test with just the 3M tape in place, with no fabric. This was approximately 2.5 times larger than the maximum crosshead forces recorded when the fabric was in-situ. The

plates were made of 5 mm thick BDMS with dimensions of 200 mm x 50 mm.

The support plates are used to isolate the frictional behaviour of the fabric from the in-plane deformation of the plies, which is particularly important when the fibre orientations are off-axis to the sliding direction. Spacer tabs are used at the ends of the support plates to compensate for the thickness of the fabric plies to ensure the sliding plane is central to the assembly when the plates are clamped in the testing frame, avoiding any unwanted bending. This resulted in a final total sample length of 175 mm and an initial contact area of 8750 mm² (Figure 3.2c).
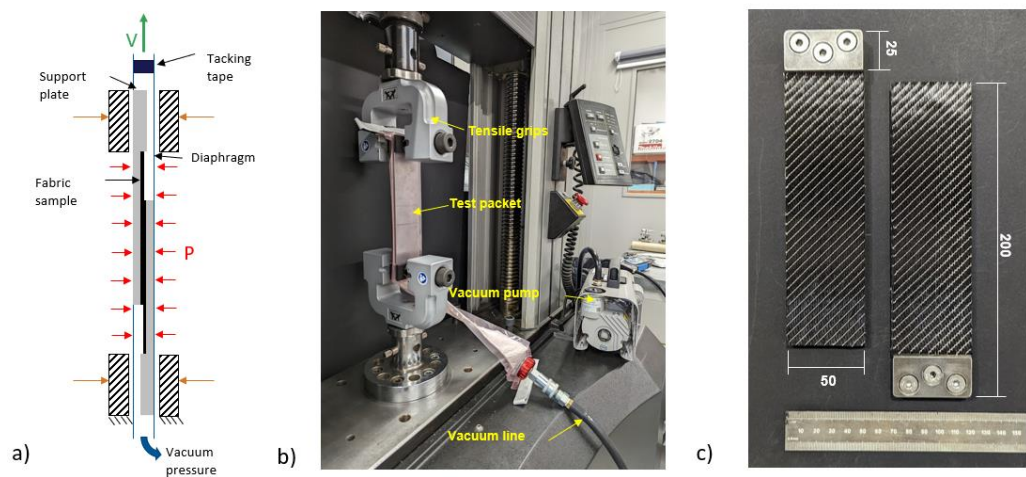
Figure 3.2 - (a) Schematic of the overlap test. (b) Test packet containing fabric samples and support plates loaded in universal testing frame. Key components of the test are labelled. c) FCIM359 fabric samples affixed to support plates with dimensions labelled for a [0°/0°] test.

The support plates, with samples affixed, are loaded into the vacuum bag (with a small amount of breather material placed below the lower clamp location to prevent lock-off), which is sealed at either end using tacky tape to form a test packet (see Figure 3.2b). The test packet is

connected to a vacuum pump using a through-bag bayonet fitting, through which the air in the packet is evacuated, simulating the consolidation stage of a DDF process. A quarter-turn ball valve and a pair of digital vacuum gauges are used to regulate the vacuum pressure applied. A gauge was placed at each end of the test packet to ensure uniform distribution of the normal load across the plates. Additionally, Fujifilm Prescale pressure measurement film was used in a trial prior to testing to confirm this uniform distribution across the entire overlap sample area.

The test packet is loaded into rubber-faced jaws, fixed to 10kN side action grips, clamping through the diaphragm material onto the ends of the support plates, as shown in Figure 3.2b. The grip faces are the same size as the spacer plates (25 mm x 50 mm), aiding alignment of the test packet within the universal testing frame and a torque wrench is used to maintain a consistent clamping force, at 30 Nm. A constant vertical displacement is applied via the crosshead at a velocity of 50 mm/min, extending the test packet and causing the fabric samples to slide over each other. The force required to generate this displacement is recorded via a 50 kN load cell which is calibrated to within 1.00% error in tension and 1.06% error in compression. The extension of the test packet was observed to have no effect on the quality of the vacuum applied, as determined by a digital vacuum gauge positioned below the lower clamp. The vacuum gauge and the tacky tape seals at the ends of the vacuum bag were positioned outside of the deformed area, avoiding any influence on the measured frictional force.

Adhesive targets placed on the steel support plates on the inside of the vacuum bag were tracked by a video extensometer to validate the crosshead displacement by ensuring there was no additional compliance within the system. The average displacement error

between the crosshead data and the video extensometer was 0.16% over a sliding distance of 50 mm. Multiple pairs of video extensometer targets were used to confirm that the plates slipped linearly with no rotation during the test. The circular targets used to track the displacement were approximately 5 pixels in diameter (0.47 mm), representing a systematic error of 0.93% in a displacement distance of 540 pixels (50 mm) over the course of the test.

3.2.3 Isolating frictional forces

The force required to extend the test packet is influenced by not only the friction at the inter-ply contact surface, but also the tensile stiffness of the diaphragm material and additional frictional forces from the surface interactions between the diaphragm and the support plates. Therefore, it is necessary to process the raw data measured by the load cell to isolate the frictional force of interest at the inter-ply interface. The unwanted effects from the diaphragm and the additional frictional forces are isolated by testing a non-deformable material with a known coefficient of friction.

Friction data for non-deformable baseline materials was obtained from a sled test, which was used to calculate a theoretical frictional force over an extension range, using Coulomb's law of friction ($F = \mu N$). This theoretical friction data was then subtracted from the original crosshead force from the overlap test to determine the unwanted load contribution from the vacuum bag extension and any other interactions within the test packet. The coefficients of friction were measured for two different non-deformable materials using the overlap test, which were compared to reference values measured by the conventional sled test. Both materials produced identical calibration curves for the data reduction process when a normal pressure of 100 kPa was applied. The results from the overlap test for

dry steel (plate on plate) (CoF of 0.35) and PTFE coated plates (CoF of 0.14) were found to be in good agreement with the reference data obtained from the sled test. This confirmed that the unwanted contribution from the stiffness of the vacuum bag and the additional friction surfaces between the bag and the plates could be effectively removed, validating the test setup. If the vacuum pressure, initial contact area and extension distance are kept constant over all experiments, the subsequent calibration curve can be assumed to be constant for any surface pairing.

This data reduction process is described in Figure 3.3, indicating results for a steel-steel interaction. The theoretical frictional force curve is calculated from the coefficient of friction obtained from the sled test. This force decreases since the overlap area decreases with increasing extension (for a given constant applied pressure). No change in coefficient of friction was observed as the applied pressure was increased for the steel-steel interaction, which confirms the robustness of the approach. Additionally, the repeat-to-repeat variability in the test proved to be low, exhibiting minimal variation in calculated coefficients of friction.
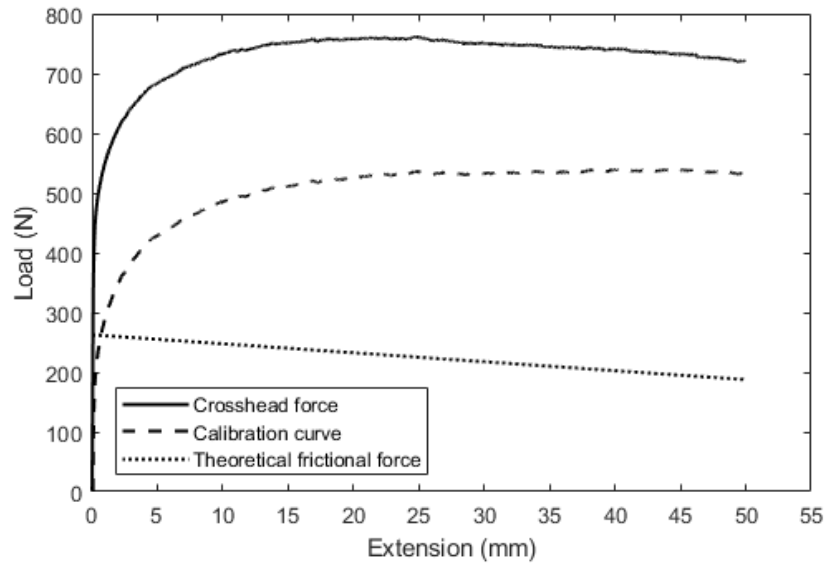
Figure 3.3 – Data reduction process for a steel-steel interaction using a known friction coefficient of 0.35. The linear theoretical friction is subtracted from the measured crosshead force to produce a calibration curve containing the additional load data that is not of interest.

Figure 3.4 shows the data reduction process applied to a fabric-fabric interaction for a pair of FCIM359 plies. The calibration curve obtained from the steel-steel interaction is used to isolate the frictional force from the crosshead load curve, which is based on an average of 3 repeat specimens. The resulting isolated frictional force decreases, since the applied pressure is constant, but the specimen overlap area decreases. This isolated load can subsequently be used to obtain the coefficient of friction for any given extension point.
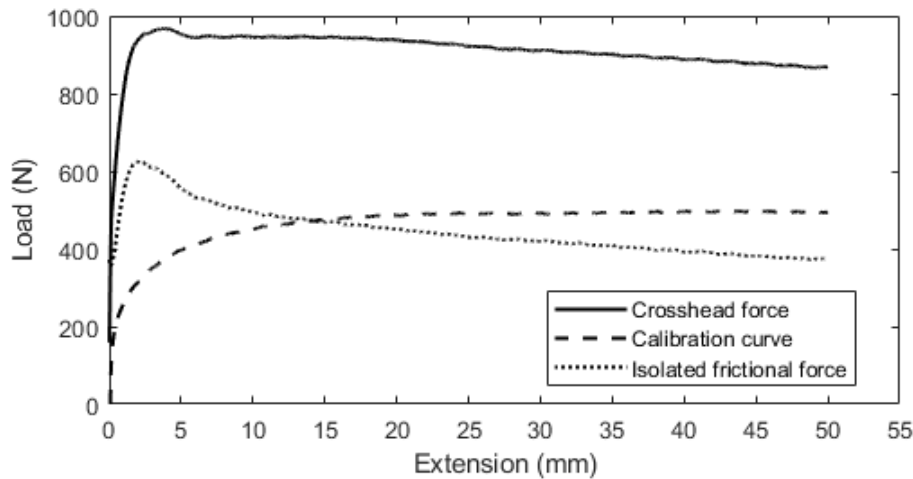
Figure 3.4 - Data reduction process for an FCIM359 interaction with parallel
fibres at the fabric-fabric interface.

Figure 3.5 shows the variation in coefficient of friction for a pair of
FCIM359 plies using the overlap test, determined from the isolated
friction load using Coulomb's law. The normal load for every given
point of extension is determined using the remaining overlap area of
the plates to determine the coefficients of friction μ, as shown in
Equation (3.1), where P is the pressure within the test packet, A is the
overlap area and F is the isolated frictional force:

$$\mu = \frac{F}{PA} \qquad (3.1)$$

Whilst Coulomb's law is a simplification, it is considered to be
appropriate for this coupon-level test because the ratio between the
frictional and normal forces is assumed to be constant for each load
case, producing a steady state value for the dynamic coefficient of
friction, μ_{dy} [78], as indicated by the later linear portion of the curve
in Figure 3.5. A large peak can be seen at approximately 2.5 mm of
extension, indicating the static coefficient of friction, μ_{st}. Behaviour

before this peak is dictated by the initial contact of the fabric, as small sliding (<2 mm) likely causes increased nesting, and the elastic deformation of micro asperities. Additional information can be derived from the curve that may be useful for future surface interaction modelling, including the static to dynamic decay constant, β [187], which can be defined using Equation (3.2), where Δx is the sliding distance from the peak of the curve to its steady state:

$$\beta = \frac{\ln\left(\frac{\mu_{st}}{\mu_{dy}}\right)}{\Delta x} \tag{3.2}$$

The decay constant describes how the frictional behaviour transitions from static to dynamic and is dictated by the shear strength of the microscale asperities at the interface. For deformable composite fabrics, the fabric architecture and fibre orientation can have a significant influence on the number of asperities in contact and therefore the macroscale decay constant.
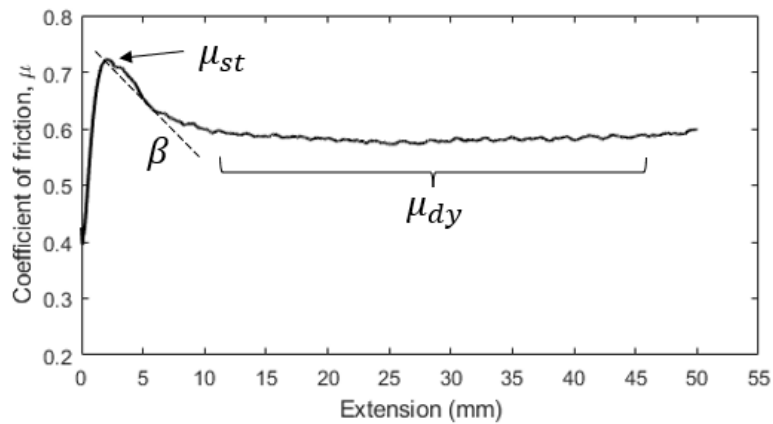
Figure 3.5 - Variation in coefficients of friction for an FCIM359 fabric-fabric interaction with stitch angles of [0°/90°] and parallel fibre angles of [-45°/-45°].

3.2.4   Hemisphere forming study

A matched tool forming case was used to simulate the effect of different inter-ply sliding conditions within a multi-ply preform, in order to contextualise the friction values obtained from the coupon test. A schematic of the forming set up is shown in Figure 3.6 demonstrating the inclusion of a vacuum bag to generate a 0.1 MPa clamping pressure on the preform, representative of the DDF process. Fabric samples affixed to aluminium plates (Figure 3.6 and Figure 3.7) were assembled about a central fabric blank to control the local coefficient of friction. Attempts were made to generate areas of high friction to inhibit uniform draw-in of the blank during the forming process, to create areas of fabric bridging, and to manipulate the shear behaviour in the final preform.
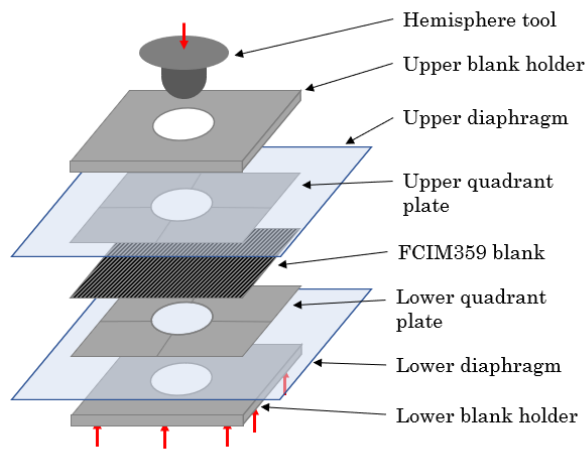
Figure 3.6 - Schematic of match tool forming test to simulate inter-ply sliding.

Two 300 mm × 300 mm FCIM359 plies were used to produce the preform blank, between which additional Epikote 05390 powder binder was applied between the plies to stabilise the geometry once it had been formed. A layup of [0°/90°// 90°/0°] was used to produce the

preforms for two reasons: to minimise slip at the interface between the two central plies, and to ensure symmetry of the frictional forces about the mid-plane of the laminate. The forming process was conducted at ambient temperature to avoid the binder influencing the friction. The hemispherical punch and the blank holders were heated to 100 °C once the form was complete, in order to activate the powder binder. The punch force was recorded using a 50 kN load cell on a universal testing machine. The force required to deform the vacuum bag was subtracted from the measured punch force to isolate the force required to enable the fabric plies to slip.

Figure 3.7 - Image of hemisphere forming test quadrant plates, in-situ of sealed diaphragms.

Two of the configurations used fabric plies fixed to friction plates (see Figure 3.6) to create fabric-fabric interfaces of perpendicular and parallel fibres respectively. A simplified distribution of the initial local coefficients of friction produced by these layups can be seen in Figure 3.8. This illustration only considers the coefficients of friction prior to any sliding or shearing of the fabric blank, as the fabric

structure is known to change locally during forming. Slip generated at the perpendicular fibre interfaces in Figure 3.8a was expected to produce a low, uniform frictional force due to the consistent orthogonal fibre arrangement between plies. According to Section 3.3.2, the coefficient of friction (μ_1) for this case was expected to be ~ 0.5 for full vacuum clamping pressure (0.1 MPa).
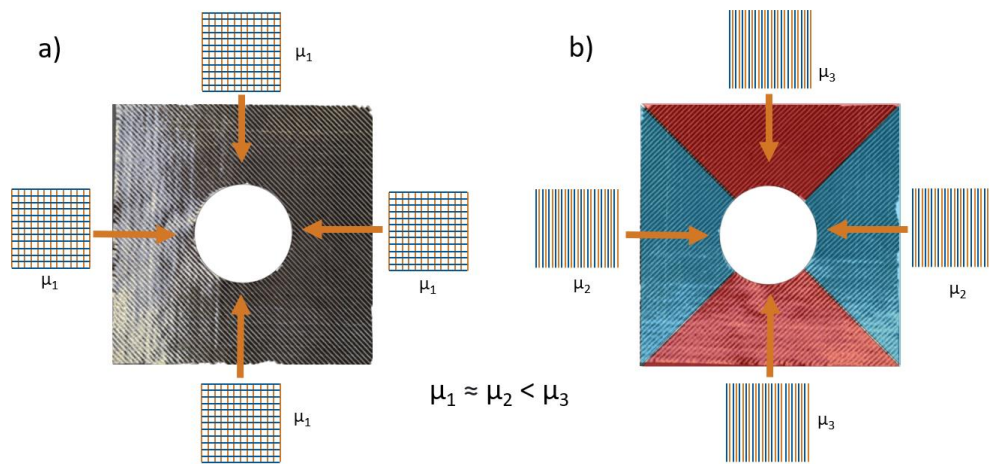
Figure 3.8 - Simplified diagram describing the initial distribution of local coefficients of friction prior to forming, generated by a) perpendicular fibres and b) parallel fibres.

The parallel interfaces highlighted in red and blue in Figure 3.8b were expected to produce higher frictional forces than the perpendicular fibre case. Whilst the interface fibres are generally parallel, the slip direction differs between the red and blue regions. According to the results from the overlap friction test in section 3.3.2, the coefficients of friction are similar for μ_2 (slip in the transverse fibre direction) and μ_1 (a perpendicular fibre interaction) at approximately 0.5. μ_3, however, was estimated to be closer to 0.72, as per the results of the overlap test. The third configuration used only the polished aluminium friction plates, offering a surface with a low coefficient of

friction at the interface (approximately 0.23, as determined by the sled test), which served as a benchmark.

The required punch force to create the preform at the end of the 50 mm stroke was chosen as the dependent variable to assess the formability of each test set up. A higher punch force indicates lower fabric formability, which can be problematic for processes such as DDF, where forming forces are often limited. If the frictional forces in the system outweigh the forming forces, then fabric draw in will be limited and bridging can occur.

3.3 Results and discussion

The following section of this chapter presents the results of the methodologies and materials introduced in Section 3.2. First, the influence of normal load on macroscale friction behaviour is discussed. Following this, the effect of ply stacking sequence, or ply orientation, is presented. The relationship between ply orientation and applied normal load is then considered, which is contextualised using the aforementioned compaction tests for two biaxial materials. Finally, the results of the hemisphere forming study are presented.

3.3.1 Effect of normal load

Results from the overlap test indicate a pressure dependency for the frictional behaviour of FCIM359. Figure 3.9 shows the variation of the coefficient of friction over the 50 mm sliding distance during the overlap test for a range of applied pressures, where each curve represents an average for a minimum of 3 repeats. The surface interaction was [-45°/- 45°] in each case. Data were obtained using the sled test for the lowest applied pressure of 4 kPa, producing static and dynamic coefficients of friction of approximately 0.29 and 0.25

respectively. Once again, stick-slip motion can be seen in the calculated coefficients of friction, even at a relatively low compaction pressure.

It can be seen that both the static and dynamic coefficients of friction are much higher when the fabric plies are subjected to higher normal loads. At 50 kPa (half vacuum pressure) the static and dynamic coefficients were found to be 0.50 and 0.38 respectively. These values increased further to 0.55 and 0.48 at an applied pressure of 75 kPa, and to 0.73 and 0.58 at full vacuum pressure (100 kPa). An increase of 60% is therefore observed for the static coefficient of friction and 57% for the dynamic coefficient of friction when the applied normal pressure increases from 4 kPa to 100 kPa. These values are significantly larger than those reported in the literature (0.18 to 0.3 [71,155,232]), which are commonly used as input parameters for forming simulations for similar materials. Higher values for the coefficient of friction can be attributed to the deformability of the fabric plies using this approach, as an increase in applied load causes a reduction in ply thickness and a subsequent flattening of the yarns [150,233]. The change in surface topography of the fabric causes an increase in the number of asperities in contact with one another [234], increasing the real contact area between the plies. In addition, yarns and individual fibres from each ply can become nested together (commingled) for certain ply layups, further enlarging the apparent contact area.
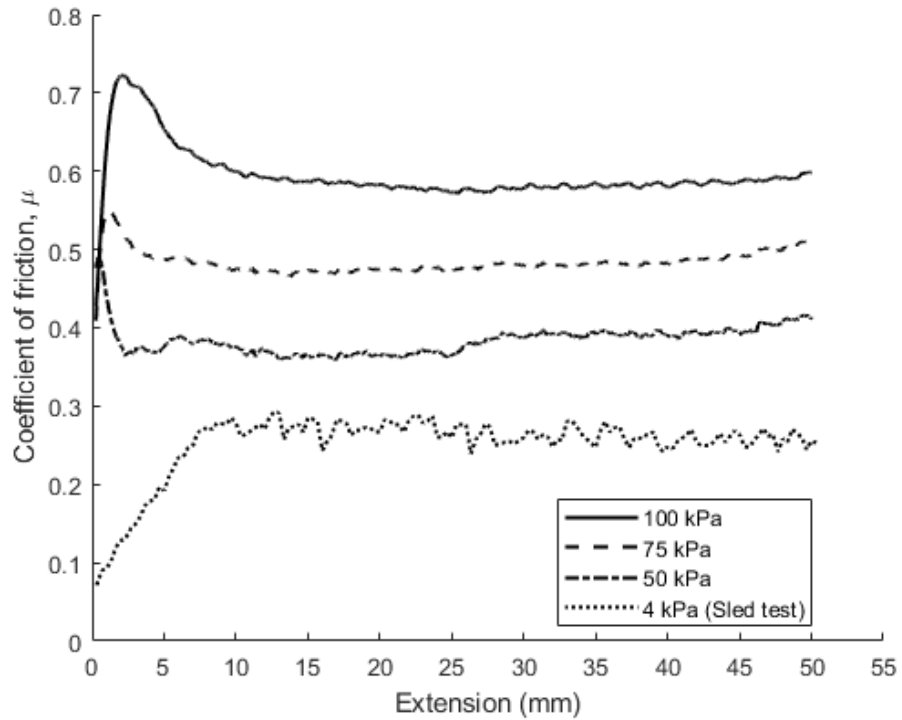
Figure 3.9 - Variation in the coefficient of friction of a [-45°/-45°] fabric-fabric surface interaction over a 50 mm sliding distance for 4 different applied pressures.

3.3.2 Effect of ply stacking sequence

Figure 3.10 shows contour plots for the static (left) and dynamic (right) coefficients of friction, where each axis of the plot corresponds to the fibre angle of each ply relative to the slip direction. The contour colours refer to the magnitude of the coefficient of friction. Each orientation pairing was repeated at least 3 times with new fabric samples applied for each repeat. Both plots are diagonally symmetric, as mirrored test configurations (i.e., [0°/15°] and [15°/0°]) produced consistent coefficient of friction values within 4% of one another.
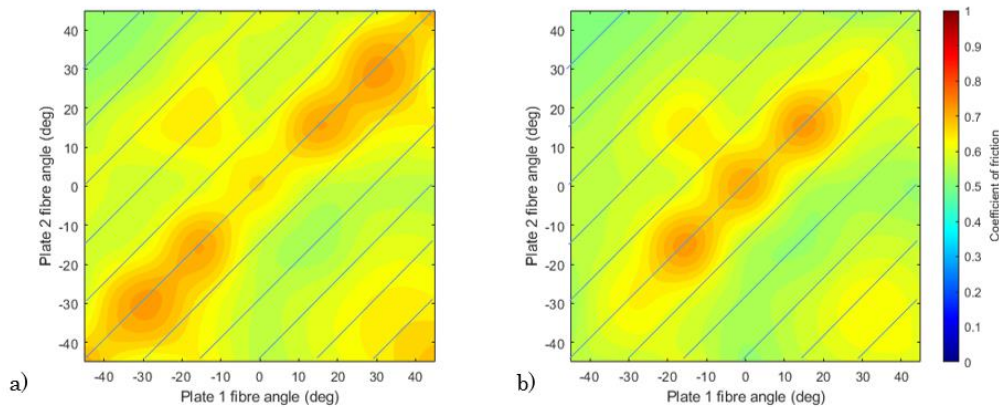
Figure 3.10 - Contour plots of coefficients of friction as determined from the overlap test at vacuum pressure. (a) Static coefficients of friction. (b) Dynamic coefficients of friction. Diagonal lines have been added to each plot to highlight the trend in coefficients with parallel fibre angles, and additional data points have been determined using linear interpolation to smooth the contour plot.

The observed trend is similar for both the static and dynamic coefficients of friction. It is also apparent that the range of friction coefficients produced as a result of varying the fibre orientations under a full vacuum load is smaller than those produced by varying the applied pressure (Figure 3.11), indicating that ply orientation is less significant than the applied compaction pressure. The static coefficient of friction ranged from 0.521 with a [-45°/45°] interaction, to 0.731 at a [-30°/-30°] interaction. Similarly, the dynamic coefficient range started at 0.500 for a [-45°/45°] interaction and increased up to a maximum value of 0.732 at [-15°/-15°]. Peak coefficients for both static and dynamic friction were observed when inter-ply fibres were parallel, and stitches were perpendicular. Diagonal lines have been added to the contour plots in Figure 3.10 to highlight this trend. Coefficients at orientations other than 0° were observed to be less dependent on inter-ply fibre angle, producing a more uniform coefficient distribution, with the exception of [45°/-45°], which

produced a higher static coefficient due to interfering parallel stitches at the interface.

Fibre orientations where the inter-ply fibre angles were the same, but the stitch angles were different, did not produce the same coefficients of friction. For example, [45°/-45°] with a 90°/-90° stitch angle pairing (top left corner of Figure 3.10b) produced a dynamic coefficient of 0.617, and [-45°/45°] with a 0°/0° stitch angle pairing (top left corner of Figure 3.10b) produced a dynamic coefficient of 0.500. Whilst the inter-ply fibre angle has a dominant effect on the fabric-fabric friction, the stitch angle also contributes to the sliding behaviour for this fabric.

Large oscillations in frictional forces are observed when the stitch direction of both fabric surfaces is perpendicular to the direction of slip, such as for a [45°/-45°] ply pairing. Opposing stitches are forced to slide over each other, which is also reflected in the coefficients of friction, as shown in Figure 3.12. The wavelength of the oscillations agrees closely with the pitch between the rows of stitches (4.5 mm) when both plies are perpendicular to the direction of slip. This is similar to the 'shock' phenomenon that has been observed during inter-ply sliding of plain weave fabrics [234]. Oscillations were also observed for additional orientation pairs with parallel stitch angles, such as [0°/90°] (45°/45° stitch interaction), with the wavelength of the oscillations increasing as the stitch angle approached 0°. The amplitude of the oscillations was observed to decrease over the course of the test when the sliding distance was greater than 50 mm, due to a reduction in the number of stitch interactions within the overlap area.
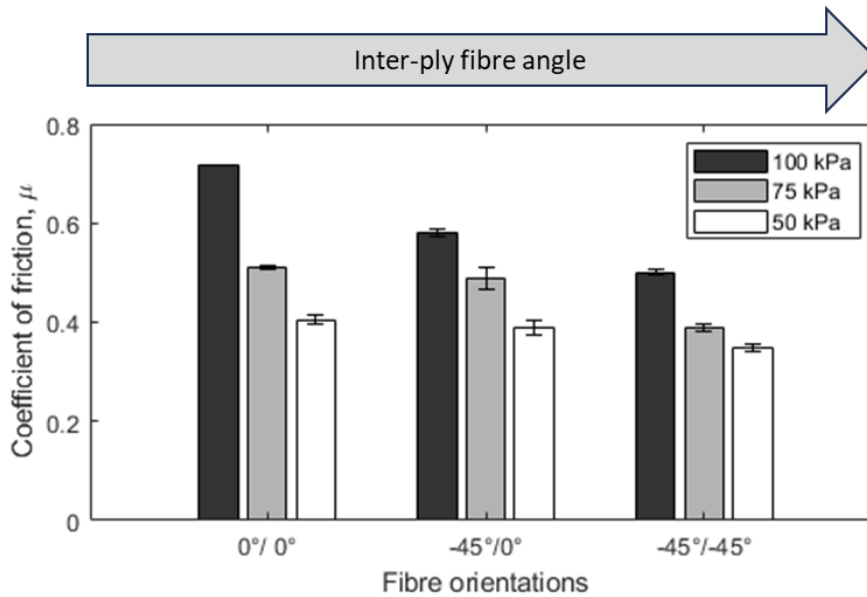
Figure 3.11 - Variation in dynamic coefficient of friction for 3 surface interaction orientations over 3 applied pressures. Error bars displayed indicate ± 1 standard deviation from the mean. The relative inter-ply fibre angle increases from left to right.

3.3.3 Relationship between fibre orientation and normal load

Figure 3.11 shows the interaction between the applied normal pressure and the relative fibre angle, in terms of the dynamic coefficient of friction measured by the overlap test. The influence of the fibre angle is relatively small at low applied pressures (50 kPa), as the coefficient of friction is reduced by 17%, from 0.41 to 0.35, as the relative inter-ply angle is increased from 0° (parallel fibres) to 90° (orthogonal fibres). The influence of the relative inter-ply angle becomes more significant as the applied normal pressure increases (i.e., at 100 kPa). The dynamic coefficient of friction reduces by 30%, from 0.72 to 0.5, as the relative fibre angle is increased from 0° (parallel fibres) to 90° (perpendicular fibres). This reduction is caused by the nesting behaviour of the fabric, as the fibre-to-fibre contact area at the mesoscale (tow level) decreases for larger relative fibre

angles (i.e., perpendicular fibres). The highest levels of fibre nesting occur between plies when the fibres on both sides of the interface are parallel (an inter-ply fibre angle of 0°). The relationship between normal load and macroscale inter-ply friction behaviours is discussed in more detail in Chapters 4 and 5.
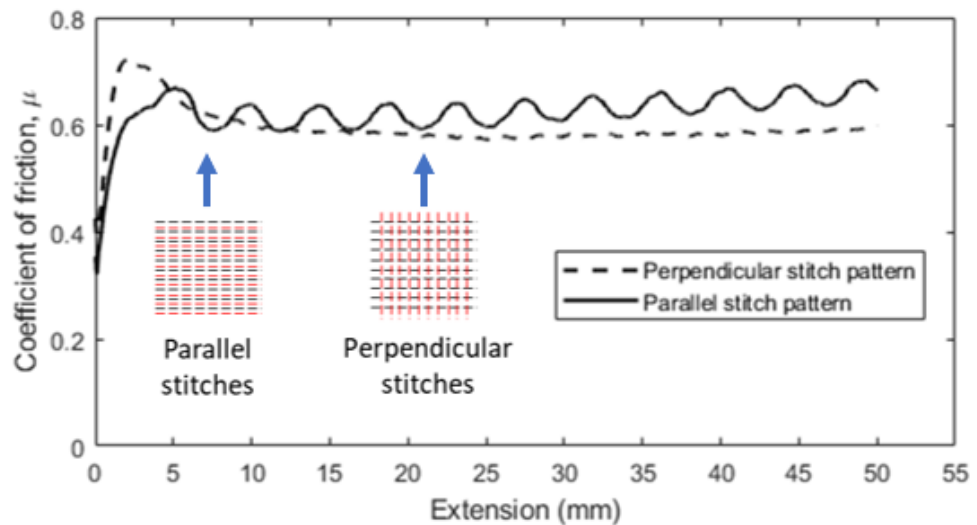
Figure 3.12 - A comparison of the variation in coefficient of friction for a [-45°/-45°] surface interaction with a perpendicular stitch orientation, and a [45°/-45°] surface interaction with a parallel stitch orientation. Blue arrows indicate direction of sliding.

3.3.4 Effect of slip direction

The effect of slip direction (relative to the global fibre direction) has also been studied. The frictional behaviour has been investigated for cases where the relative fibre angle at the inter-ply interface were the same (i.e., parallel fibres), but the loading direction was varied relative to the fibre direction. Thus, the slip direction varied by the same angle for both fibre directions at the interface respectively. All samples were subjected to a normal pressure of 100 kPa.

Figure 3.13 shows the effect of slip direction on the static and dynamic inter-ply coefficients of friction. As the angle between the fibre orientation and the slip direction increases, the dynamic coefficient of friction decreases, while the static coefficient increases. When the fibre orientation is perpendicular to the direction of slip (transverse fibre slip), fibres must roll over one another across the radial direction, creating a large initial resistance to motion and producing a high static coefficient of friction. When in motion, however, the fibres are not able to nest as effectively, reducing the real contact area between plies and therefore reducing the dynamic coefficient of friction.
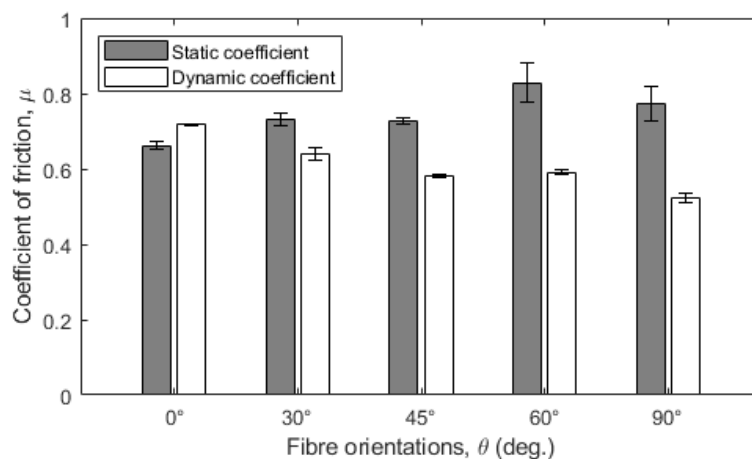
Figure 3.13 - Effect of slip direction on inter-ply static and dynamic coefficients of friction. Error bars show ± 1 standard deviation from the average.

This phenomenon is also captured by the variation in the decay constants between the static to dynamic coefficients of friction (see Equation (3.2) for definition), as shown in Figure 3.14. As the fibre orientations become perpendicular to that of the slip direction, the decay constant increases (i.e., the sliding distance required to achieve

a linear coefficient of friction decreases). This behaviour is interesting from a surface interaction modelling point of view, as it is questionable whether the static coefficient of friction is more relevant than the dynamic coefficient of friction when the inter-ply slip distances are low.
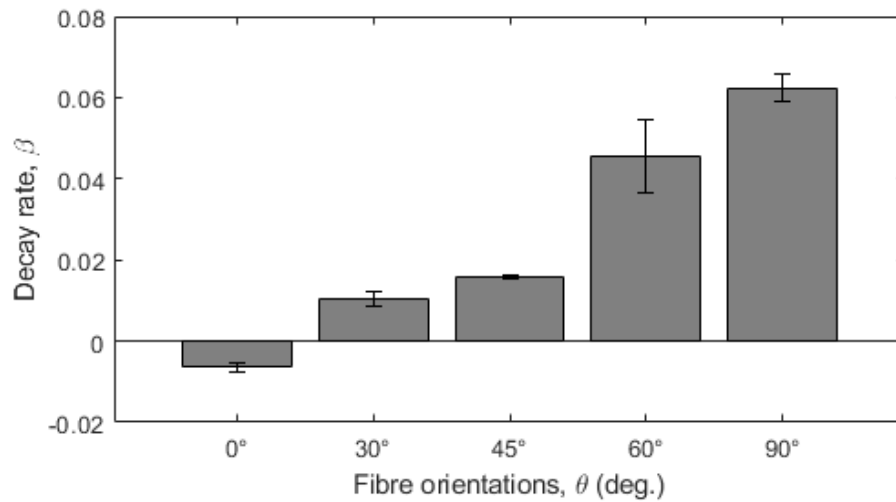
Figure 3.14 - Effect of slip direction on the decay constant of static to dynamic coefficients of friction. Error bars show ± 1 standard deviation from the average.

It can be seen in Figure 3.14 that the decay coefficient at a parallel fibre interface is negative, due to the static coefficient of friction being lower than the dynamic (shown in Figure 3.13). A full investigation into the cause of this is considered beyond the scope of this thesis, but it is likely caused by the microscale contact mechanisms at the ply-ply interface – as sliding begins to initiate fibres find positions to nest and the number of asperity contacts increases.

3.3.5 Significance of inter-ply frictional behaviours on formability

In general, friction, shear, bending and tensile deformation mechanisms all contribute to forming behaviour. To highlight the contribution of the friction and to analyse the effect of the fibre orientation dependency, a hemisphere forming case was designed to induce controlled levels of inter-ply slip. Three of the layups used during the overlap friction test were selected to investigate the influence of the local coefficient of variation on the magnitude of the frictional forces generated during forming.

Results from the hemisphere forming study in Figure 3.15 indicate that the measured punch force had a high dependency on the applied clamping pressure, with the peak force increasing from 0.75 kN to 8.2 kN as the applied pressure on the friction plate was increased from 15 kPa to 100 kPa. Similar to the findings from the overlap friction test, the influence of the fibre orientations at the slip interface was less significant in terms of the forming force, but a trend could be established.

Figure 3.15 shows that the punch force was higher when all fibres were parallel at the inter-ply interface between the blank and the fibres attached to the friction plate, compared with the perpendicular fibre case. This difference is more significant when full vacuum pressure is applied, which is also in agreement with the results from the overlap test. The punch force required to form the preform increases from 6.3 kN to 8.2 kN when the fibres are rotated at the inter-ply interface to become parallel with one another.
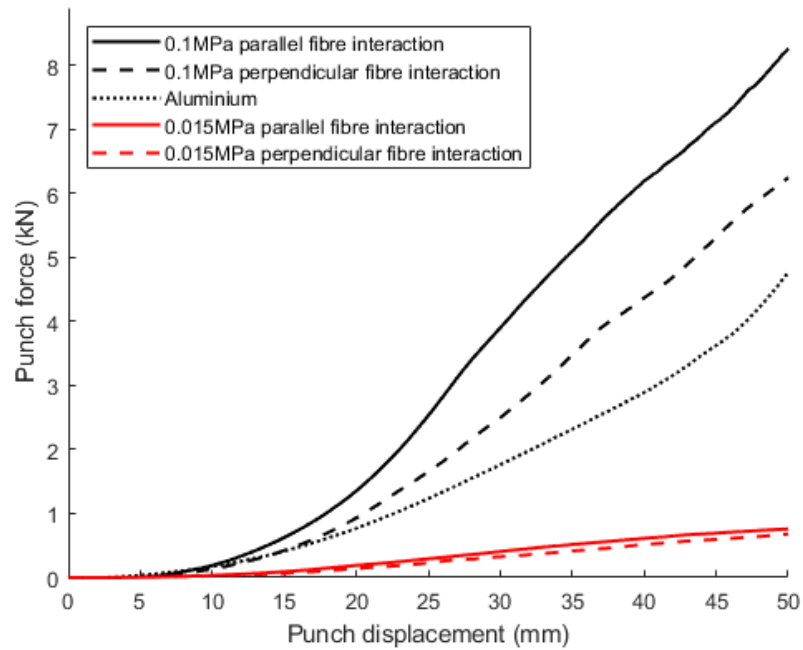
Figure 3.15 - Frictional force vs punch displacement results for hemisphere forming study.

In addition to variations in measured punch force, anisotropic friction behaviour resulted in some additional forming defects on the surfaces of the preform. Figure 3.16 shows an example of in-plane fibre distortion, caused by failure of the stitches. This laddering phenomenon is only observed where parallel fibres at the interface slip transversely relative to one another (i.e., the blue shaded areas in Figure 3.8b). As the transient fibres on the blank draw in to form the hemisphere, the stationary fibres attached to the friction plate try to resist the motion, resulting in local bunching of the primary yarns and large tensile stresses in the stitches. This is indicative of the different slip mechanisms that occur during transverse slip of parallel fibres and longitudinal slip of parallel fibres, as this type of defect is not visible in the other quadrants (shaded blue in Figure 3.8b).

Figure 3.16 - Example of in-plane fibre distortion caused by anisotropic friction in the forming process.

3.4 Chapter summary and conclusions

A novel characterisation test for capturing inter-ply frictional behaviours under normal loads representative of a DDF process has been presented. The test uses vacuum pressure to apply compaction to a fabric-fabric interface, where samples can be fixed at any orientation to enable investigation of anisotropic friction mechanisms. The test showed that inter-ply frictional behaviour of FCIM359 is anisotropic; interactions with parallel fibres at the interface generated higher static and dynamic coefficients of friction than those of any other angle, which was attributed to fabric-fabric nesting behaviour.

The influence of normal pressure on the friction of FCIM359 was also demonstrated. Results have shown that coefficients of friction commonly used for DDF forming simulations are much lower than real-world values, due to the assumption that the fabric plies are non-

deformable. Increasing the applied normal pressure during the overlap test from 25 kPa to 100 kPa increased the measured coefficient of friction by up to 43%, due to increased ply-ply nesting and fabric deformation, which will be explored in the next chapter.

The significance of the variation of friction was evaluated using a matched tool forming test to induce controlled inter-ply sliding. It was found that inter-ply sliding of fabric-fabric interfaces with parallel fibres required significantly higher punch forces to create a preform, and hence these architectures have lower formability (i.e., higher potential for defect formation) and should be avoided from a Design for Manufacture point of view. However, in a typical DDF or matched tool forming process, slip between plies with parallel fibres at the interface is expected to be minimal. As they deform in a very similar manner, any relative motion would be caused by geometrical features, such as laminate thickness increasing corner radii.

4. An investigation of multiply compaction and nesting behaviour

4.1 Chapter outline and research aims

The aim of this chapter is to investigate the macroscale compaction and nesting behaviours of dry multi-ply biaxial NCF laminates, in the context of the inter-ply frictional behaviours discussed in the previous chapter.

A traditional through-thickness compaction test is employed as the primary characterisation method and is first used to investigate the typical response of a dry multi-ply stack to through-thickness compressive load. This data is used to calculate a consolidation stiffness of the laminate for later inclusion in finite element analysis of DDF processes. The effects of ply orientation and the inclusion of a polymer veil material are investigated to quantify inter-ply nesting through the stack, which is visualised using optical microscopy.

Additionally, the viscoelastic relaxation behaviour of the laminate stack is examined, considering the effect of compressive strain rates and ply orientations to inform studies in later chapters of this thesis.

4.2 Chapter methodology

The first section of this chapter describes the materials and methodology used to characterise the multi-ply compaction behaviour of biaxial NCF fabrics.

4.2.1 Materials

The primary material used in this chapter is the same biaxial pillar stitched NCF as described in the previous chapter, FCIM359. The relevant material properties for FCIM359 can be found in Table 3.1.

A second biaxial NCF was used to study the influence of the use of the inclusion of a polymer veil material on the inter-ply compaction and subsequent frictional behaviours. HiMax® MBB00 (also provided by Hexcel Reinforcements) was selected as a comparison to FCIM359, due its similar biaxial architecture and areal weight. The non-woven PPS thermoplastic polymer veil is commonly included in composite materials to improve the inter-lamina fracture toughness of a finished component. The relevant material properties of MBB00 are shown in Table 4.1, and the nomenclature for its usage is the same as for FCIM359, as described by Table 3.2.

Table 4.1 - Material properties of HiMax® MBB00.

Name	HiMax® MBB00	
Supplier	Hexcel	Veiled fabric surface
Fabric type	Biaxial NCF	
Areal weight	536gsm	
Fabric thickness	0.52mm	
Stitching	Polyester pillar stitch	Non-veiled fabric surface
Fibre	12k carbon tows	
On-roll fabric orientation	Stitch 0º, fibre ±45º	

4.2.2 Fabric compaction tests

Both biaxial fabrics were analysed using a through-thickness compaction test (Figure 4.1) fitted to a universal testing machine, to understand the nesting behaviour of the plies. Fabrics with lower

through thickness stiffnesses are more susceptible to fibre nesting about the inter-ply interface and are therefore likely to exhibit higher coefficients of friction. The test rig platens were aligned before the test using a steel plate, and two lateral LVDTs were used to confirm there was no rotation between the platens. Baseline tests were conducted at a rate of 1 mm/min, as the effect of compressive strain rate was not investigated for this initial study. The applied force was measured by a 50 kN load cell.
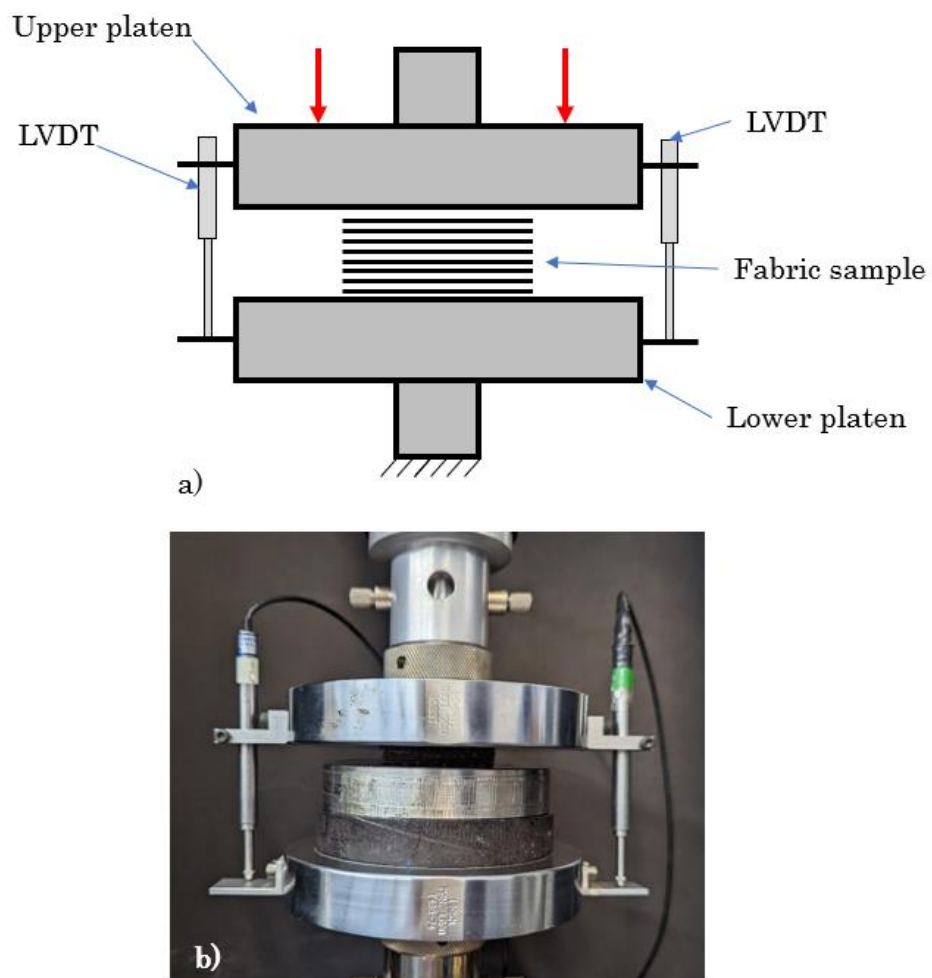
Figure 4.1 - a) Schematic of compression test set up, showing bilateral LVDTs to validate the compressive displacement measurement. b) Image of test set up.

To present the resulting data from these tests, the crosshead force was used to calculate pressure over the sample area, and the LVDT displacement was used to estimate the fibre volume fraction (V_f) of the stack using data from the material data sheet. This is described by Equation (4.1) where m is the areal mass of the fabric, ρ is the density of carbon fibres, n is the number of plies and d is the absolute distance between the platens. Representing the data in this manner enables comparison with many similar tests and materials in the literature.

$$V_f = \frac{n \cdot m}{d \cdot \rho} \qquad\qquad (4.1)$$

4.3 Results and discussion

The following section of this chapter presents the results of the compaction tests undertaken and evaluates their significance when compared to the macroscale frictional behaviour presented in the previous chapter.

4.3.1 FCIM359 nesting behaviour

Fabric coupons were cut to 50 mm × 50 mm and stacked to create 2, 4, 8 and 10 ply laminates. The ply orientations were chosen to produce parallel, perpendicular and 45° inter-ply fibre orientations for every inter-ply surface interaction through the stack, ($[0°/90°//90°/0°]_{n/2}$, $[0°/90°]_n$ and $[0°/90° //\pm45°]_{n/2}$ respectively, where n refers to the total number of plies in the layup).

Results from the compaction tests for laminates of increasing numbers of plies are shown in Figure 4.2. It can be seen that parallel

fibre interactions exhibit a lower compaction stiffness than non-parallel fibre interactions, which can be attributed to the microscale nesting behaviour of the filaments. At parallel inter-ply fibre orientations (0°), yarns and individual fibres of contacting plies can slide past one another in the through-thickness direction, and therefore a higher fibre volume fraction is achieved for a given compaction pressure. If the inter-ply fibre orientation is anything other than 0° however, this nesting is inhibited, as the fibres from opposing plies prevent one another from commingling. This can be seen in every graph for the increasing number of plies shown in Figure 4.2, as the perpendicular (90°) and 45° fibre orientation interactions exhibit very similar compaction behaviour.
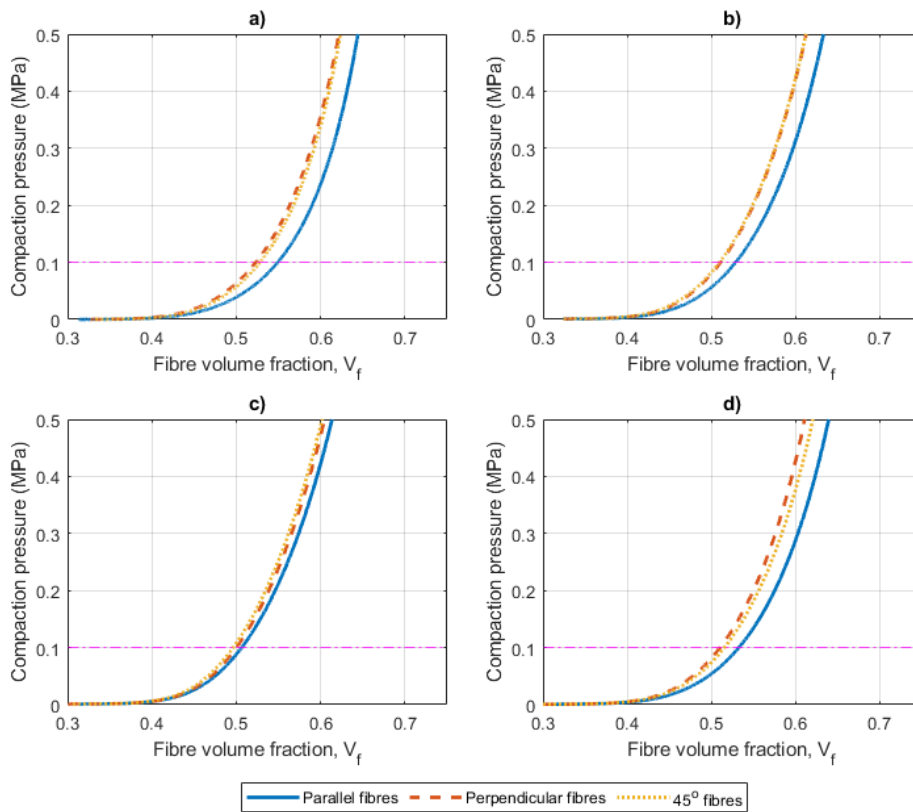
Figure 4.2 - Fibre volume fraction versus compaction pressure of FCIM359 laminates. a) 10 ply laminates. b) 8 ply laminates. c) 4 ply laminates. d) 2 ply laminates. Each curve represents an average of 3 repeats, and a horizontal magenta line indicates vacuum pressure, representative of a DDF process.

This compaction orientation dependency aligns closely with the results seen in the overlap friction test described in Section 3.3. A larger coefficient of friction is measured when the inter-ply fibre orientation is at 0°, due to the relatively large contact areas from increased fibre nesting along the length of the fibres. For all other inter-ply angles the nesting behaviour is reduced, as the tows only make local contact with one another at common high points along the length of the fibres, yielding lower, more uniform coefficients of friction when compacted during forming.

The anisotropic compaction behaviour can be examined further using optical micrographs, such as those shown in Figure 4.3. Images

indicate that the laminate with perpendicular fibres at the interface ($[0°/90°]_8$) exhibits minimal intra-ply deformation through the cross section, with the yarn shapes and spacings remaining consistent throughout. Conversely, large deformations of the ply surface can be observed when the fibres are parallel at the inter-ply interface (see Figure 4.3b for the $[0°/90°//90°/0°]_4$ laminate). Yarns from each ply are forced into the available gaps between the yarns of the contacting ply, deforming the fabric at the mesoscale. Individual fibres from different plies become commingled, dramatically changing the surface topography of the plies.

a)

b)
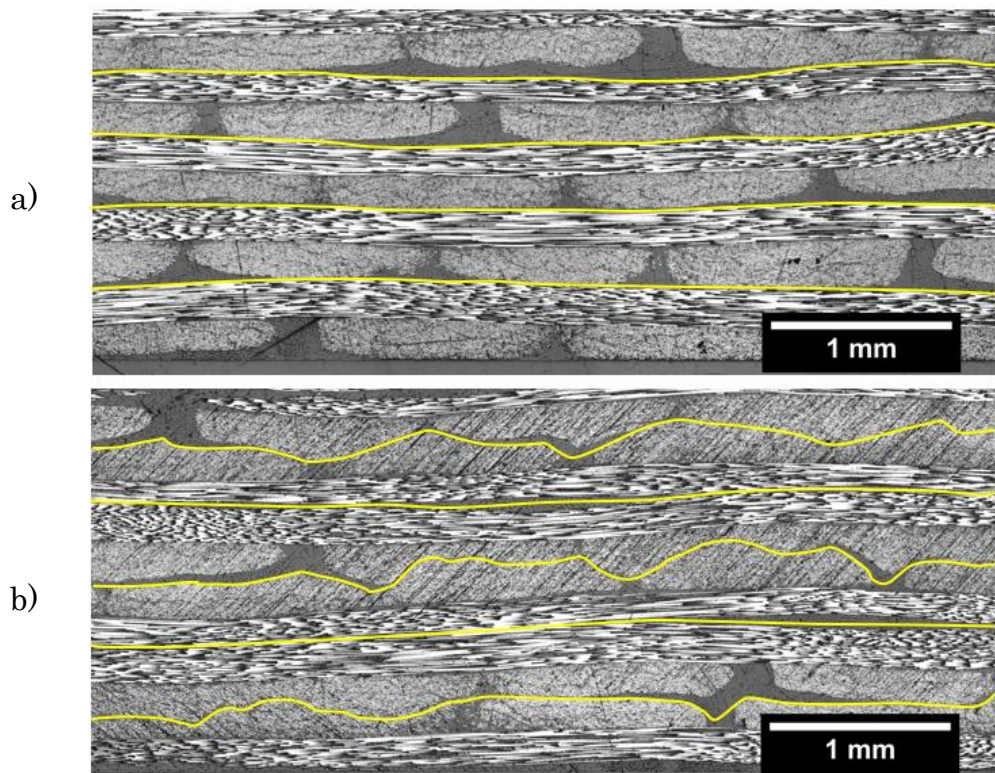
Figure 4.3 - (a) Optical micrograph of a $[0°/90°]_8$ laminate under vacuum load showing consistent yarn shape and spacing. (b) Optical micrograph of a $[0°/90°//90°/0°]_4$ laminate under vacuum load showing yarn deformation along the parallel fibre interfaces between plies. Yellow lines indicate approximate ply interfaces.

When considering the macroscale inter-ply frictional behaviour discussed in Chapter 3, this deformation contributes to the change in friction in both the longitudinal and transverse slip directions. For slip in the longitudinal fibre direction, the contact area between the plies is increased as additional yarns and fibres are pushed against each other. Transverse slip is impeded by yarn deformation, as nested yarns and fibres must shear or deform during the test for the plies to move relative to one another. Similar behaviour has been observed for woven fabrics [235]. As a result of these two independent slip restriction mechanisms, any fabric-fabric surface interaction with parallel fibres will exhibit larger coefficients of friction when under load than perpendicular fibres, regardless of the relative angle of the fibres to the direction of slip.

A trend in the compaction stiffness and number of plies was observed, whereby laminates with more plies were slightly less stiff than those with fewer. Figure 4.4 shows the average values of fibre volume fraction for each laminate at vacuum pressure (also represented by the horizontal magenta line on Figure 4.2). The largest V_f value (for a 10-ply stack) when fibres were parallel was 8% larger than the smallest value (a 4-ply stack), suggesting that thicker laminates are more compliant than thinner laminates. Once again, this is likely due to increased levels of nesting within the stack – more yarns and fibres are available to comingle, allowing a greater fibre volume fraction to be achieved for a given compaction pressure. This results aligns with the results presented by Lomov et al. [136], who demonstrated that, for a given compaction pressure, relative ply thickness decreases with an increasing number of layers.
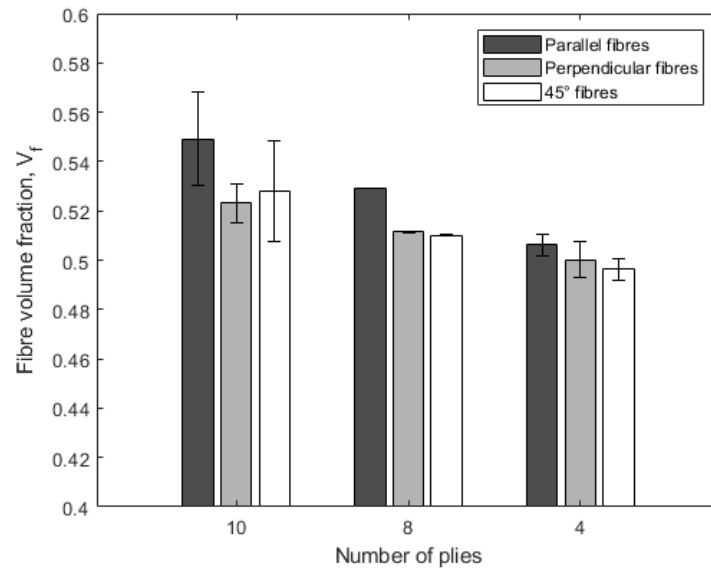
Figure 4.4 - Fibre volume fraction at vacuum pressure for FCIM359 laminates of 4 different numbers of plies. Error bars represent ±1 standard deviation from the mean.

4.3.2 MBB00 nesting behaviour

Inclusion of a polymer veil material was observed to reduce the anisotropy of the nesting behaviour of biaxial NCFs. Figure 4.5a, b and c show the compaction curves for 10, 8 and 4 ply layups of MBB00 NCF respectively, with plies orientated to generate parallel (0°), perpendicular (90°) and 45° fibre orientations at every inter-ply interface. The difference in compaction stiffness between orientations was negligible, implying that the inclusion of the veil material significantly reduces inter-ply nesting of fibres. Figure 4.5d shows the difference in compaction behaviour between the 10-ply MBB00 and 10-ply FCIM359 laminates. Whilst the MBB00 material exhibits slightly stiffer compaction behaviour because of the inclusion of the veil, the orientation dependency is negligible compared to that of the FCIM359 plies. All three curves for the MBB00 samples lie on top of

one another, indicating that the compaction behaviour is independent from the inter-ply fibre orientations.
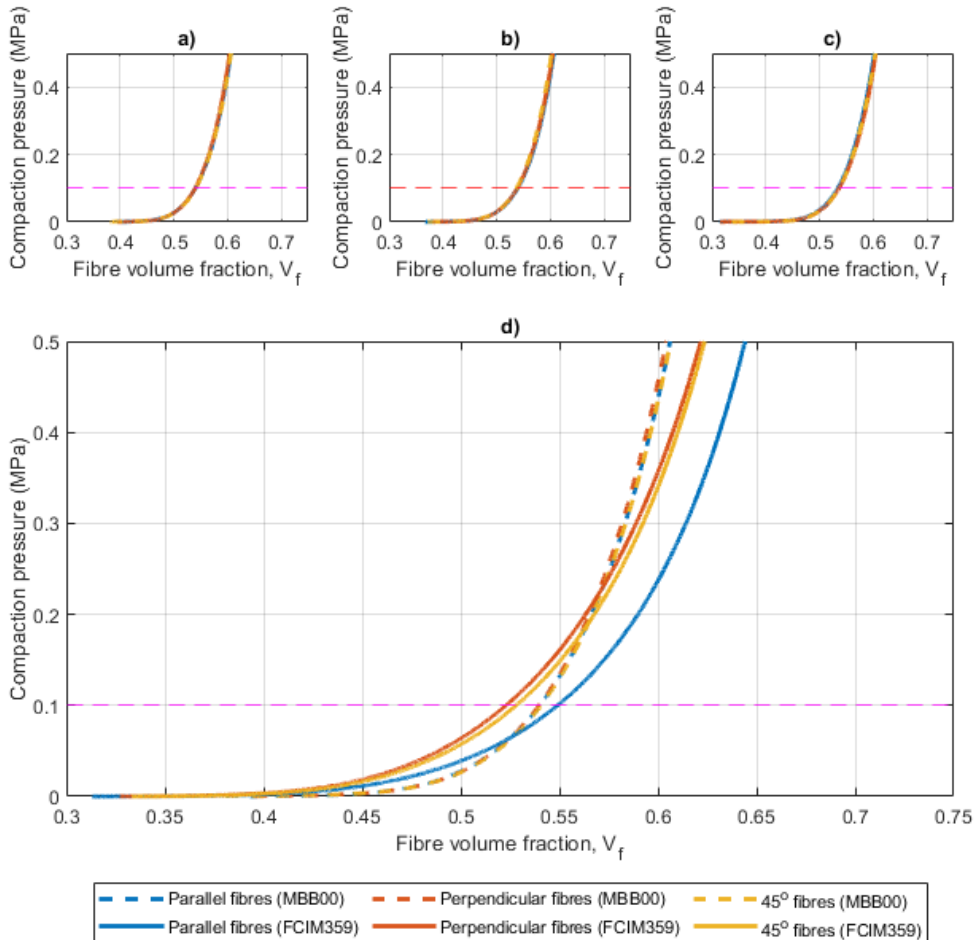
Figure 4.5a) 10 ply MBB00 laminate compaction curves. b) 8 ply MBB00 laminate compaction curves. c) 4 ply MBB00 laminate compaction curves. d) Comparison of 10 ply compaction curves for MBB00 and FCIM359 NCFs. Each curve represents an average of 3 repeats, and the horizontal magenta lines indicate vacuum pressure, representative of a DDF process.

Examining the fibre volume fractions of MBB00 laminates held under vacuum pressure reinforces this. Figure 4.6 shows a much weaker correlation between orientation and volume fraction when compared to the equivalent data for FCIM359. Likewise, the effect of reducing

the number of plies is less significant, as the amount of inter-ply nesting is reduced.
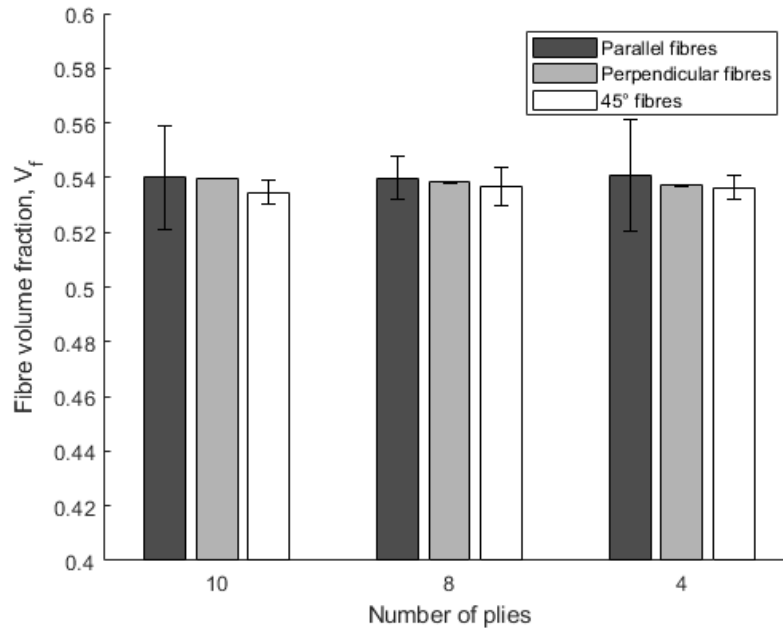
Figure 4.6 - Fibre volume fraction at vacuum pressure for MBB00 laminates of 4 different numbers of plies. Error bars represent ±1 standard deviation from the mean.

Figure 4.7 shows optical micrographs of two 8-ply laminates constructed using the MBB00 NCF containing the non-woven polymer veil, which are directly comparable to the micrographs in Figure 4.3 for the FCIM359 material. For the perpendicular fibre case (Figure 4.7a), the laminate architecture is much the same as FCIM359, maintaining a yarn structure with consistent size and spacing. Inclusion of the polymer veil between the plies clearly reduces the penetration of fibres across the inter-ply interface for the parallel MBB00 fibre orientation case, as can be seen in Figure 4.7b, compared with the equivalent FCIM359 laminate (Figure 4.3b). Whilst the yarns are still able to deform, microscale fibre commingling

is entirely prohibited, and material from each ply remains in discrete layers.
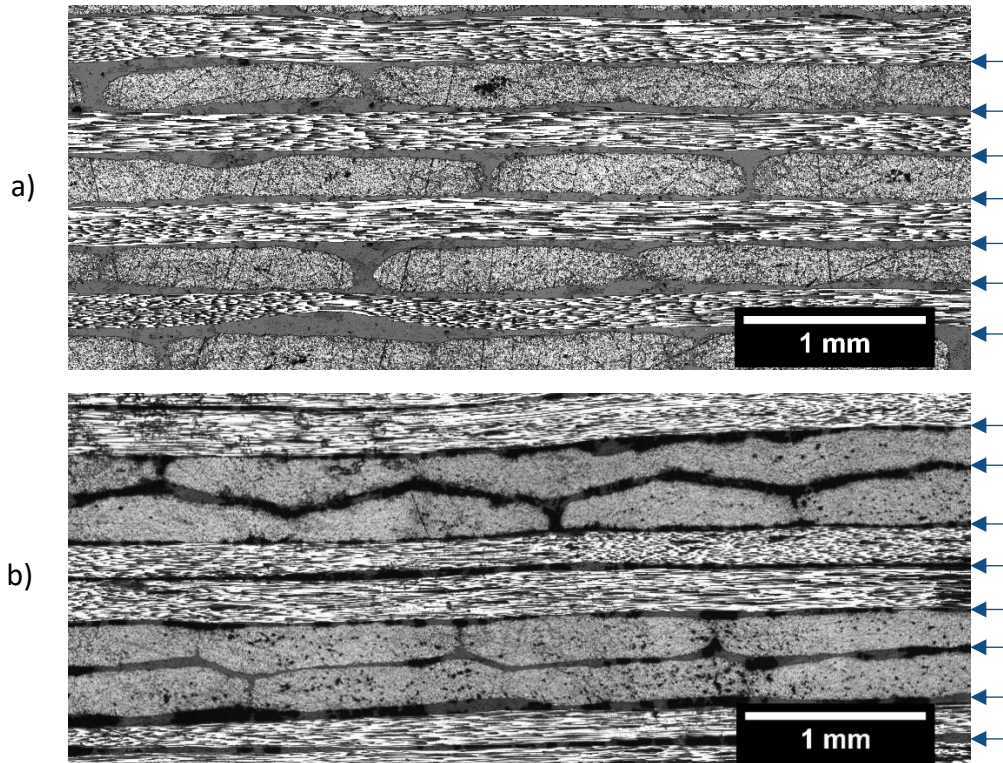
Figure 4.7 - Optical micrographs of 8 ply laminates with interleaved polymer veil under vacuum load. (a) [0/90]8 laminate. (b) [0/90//90/0]4 laminate. Arrows to the right indicate the locations of the polymer veil between each MBB00 ply.

The absence of nesting behaviour in the MBB00 material has the subsequent effect of changing the inter-ply frictional behaviour of the NCF. Figure 4.8 shows a comparison of the dynamic coefficients of friction obtained using the overlap test (see Chapter 3) for both FCIM359 and MBB00 NCFs. The FCIM359 plies exhibited a 28.8% difference in dynamic coefficient of friction between the parallel and perpendicular fibre interactions, but the same orientations for the MBB00 NCF produced a much smaller difference of 10.9%. The coefficients for the MBB00 (0.49 – 0.52) are both similar to the

perpendicular value for the FCIM359 (0.55), as the veil prevents nesting of the fibres between plies.
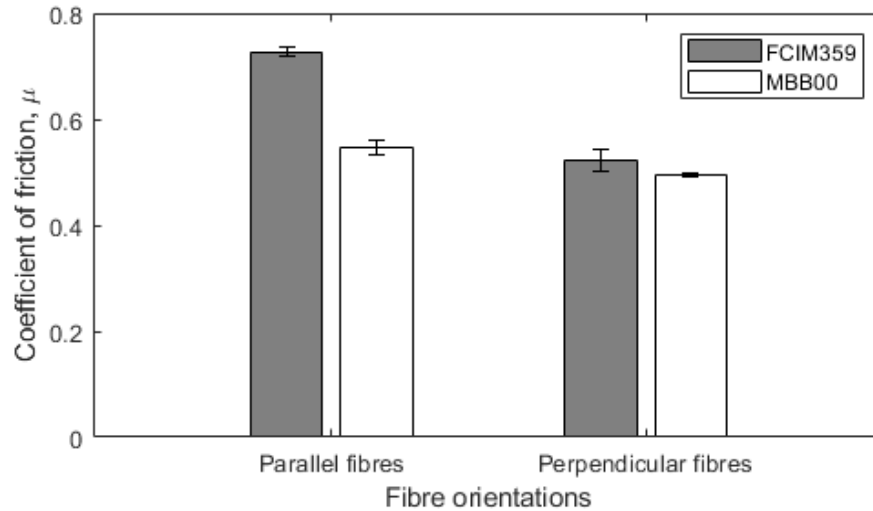
Figure 4.8 - Comparison of dynamic coefficients of friction for a biaxial NCF (FCIM359) and a biaxial NCF with a non-woven veil (MBB00), for both parallel and perpendicular fibre orientations. The error bars shown display ± 1 standard deviation.

Figure 4.9 shows the deformation of the veiled material as a result of the overlap test. The veil is initially distributed uniformly over the surface of the sample but becomes distorted during the test by the raised stitches, causing the non-woven material to tear and agglomerate. In addition, some damage to the carbon tows was observed below the veil. As the primary purpose of the veil is to improve the inter-lamina fracture toughness, it may be important to consider how this damage influences the final mechanical performance of the component if large slip distances are expected during the forming process.
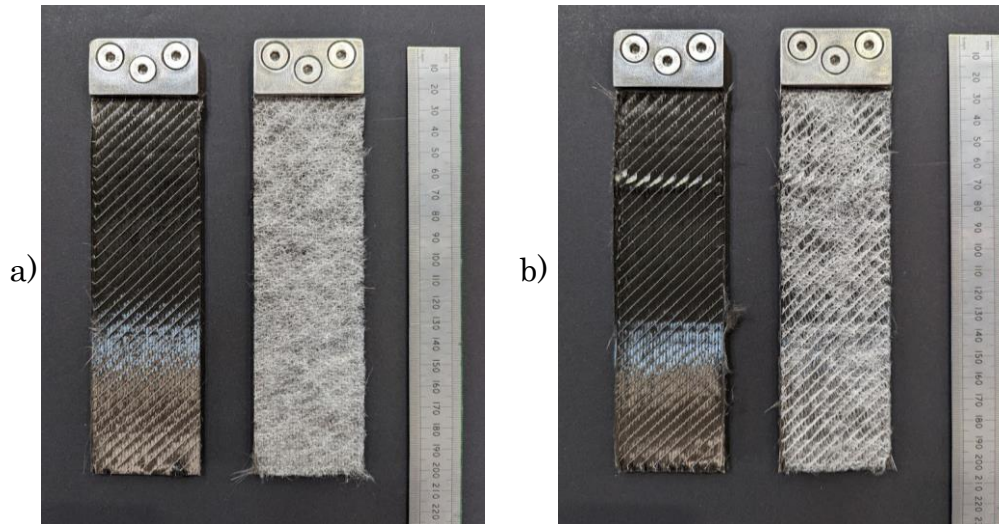
Figure 4.9 - (a) MBB00 NCF samples before conducting overlap test and (b) after conducting overlap test.

4.3.3 Viscoelastic stress relaxation

Characterisation of the stress relaxation behaviour of multi-ply FCIM359 laminates was conducted using the same experimental test set up described in Figure 4.1. It is important to consider viscoelastic stress relaxation when predicting the compaction response of dry multi-ply preforms, and it is difficult to accurately calculate time-dependent spring back [236]. The data gathered from the relaxation tests will primarily be used to inform the in-situ X-ray computed tomography (CT) work presented in the next chapter.

Figure 4.10 shows the relaxation profiles of dry laminates subject to 3 different compressive strain rates; 10 mm/min, 1 mm/min and 0.5 mm/min. Each laminate used a $[0°/90°]_{10}$ layup and was compressed to a maximum load of 150 N (equivalent to 166 kPa) before being allowed to relax for 10 minutes. It can be seen that the rate of compression has a significant influence on the load at the end of the allowed relaxation period, wherein larger rates result in a much lower final compressive load. This behaviour agrees well with that of other

textile reinforcement materials in the literature (such as the work conducted by Robitaille et al. [142], who note that compaction rate is the most significant influence on the relaxation process) and can be attributed to reorganisation of the fibre structure within the laminate. A 10 mm/min compressive strain rate produced the largest drop in compressive stress, with a 74% reduction in measured load. A 1mm/min compressive strain rate exhibited a 59.1% reduction, whilst a 0.5mm/min rate exhibited a 49.6% reduction. This behaviour aligns with what can be found in existing literature, and can be attributed to the complex time-dependent movement and rearrangement of fibres at the microscale [146,148,237].
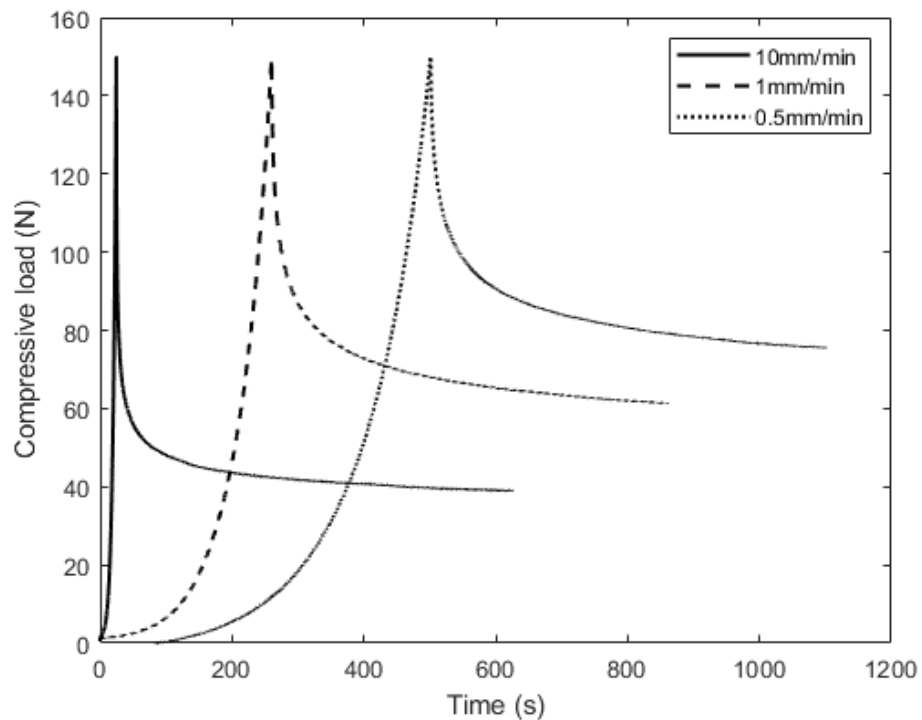
Figure 4.10 – Relaxation profiles of a dry FCIM359 NCF stack subject to 10 mm/min, 1 mm/min and 0.5 mm/min compaction rates.

The cyclic compaction response of dry fabric laminates was also investigated with the aim of determining the appropriate load cases

for the in-situ CT scanning presented in Chapter 5. The test was conducted by applying a constant displacement to the upper platen until a pre-determined load was achieved, followed by a 10-minute relaxation period. A 1 mm/min strain rate was used for the test; whilst a slower strain rate may have produced less relaxation, a 1 mm/min rate was selected as it was the minimum stable rate possible to be applied by hand when using the screw-action compression rig described in Section 5.2.2.

As a 1 mm/min rate produced a load relaxation of approximately 60%, the target load profile was achieved by exceeding the desired load by 50% (as the target load profile was considered to be an ideal minimum desired compaction force). This is presented in Figure 4.11, which shows an example cyclic compaction curve for a single dry laminate sample of FCIM359, using a layup sequence of $[0°/90°]_{16}$.

The load profile was selected to give an evenly spaced range of pressures up to and including vacuum pressure, representative of DDF processes. Each peak of the curve indicates 150% of the subsequent target load. It can be seen that with each additional cyclic load, the time taken to achieve a stable compressive load increases, quickly becoming larger than the allocated 10 minutes relaxation period. Despite this, the compressive force at the end of each relaxation period was within 20% of the target load with an average of 15%, which was deemed a sufficient approximation for the purpose of the tomography work in Chapter 5.
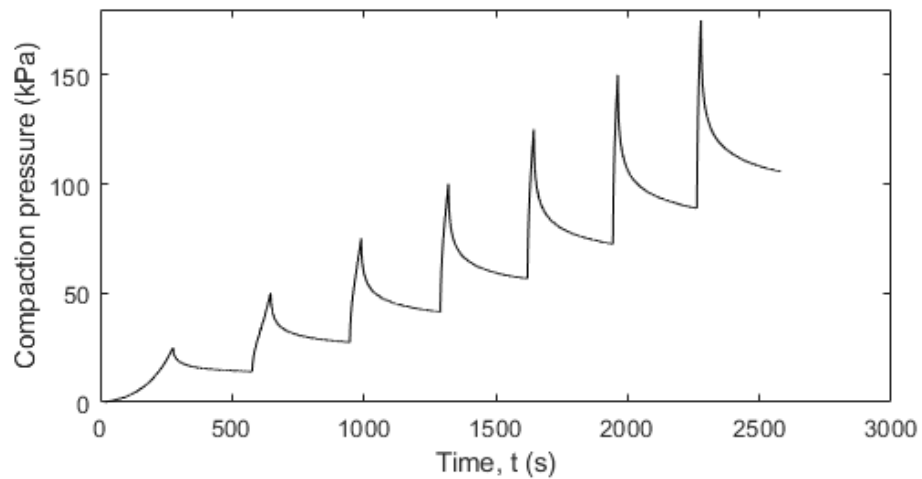
Figure 4.11 - An example loading profile used to investigate cyclic compaction behaviour of FCIM359.

Layup sequence was found to have little influence on the cyclic compaction response of FCIM359. Two laminates were tested, $[0°/90°]_{16}$ and $[0°/90°//90°/0°]_8$, which were selected to generate perpendicular and parallel fibre interactions at the interface respectively. Figure 4.12 shows the relaxation percentage from the initial load for each of the cyclic load targets and layup sequences. Over the entire load case, a gradual reduction in the magnitude of relaxation can be seen as the applied load increases, from 45.2% to 40.3%.

This decrease can be attributed to the rearrangement of the fabric architecture, as described in existing literature [142,237,238]. Intra-ply friction causes the applied compaction energy to dissipate further over each applied normal loading cycle. Very little difference in relaxation behaviour can be seen between the two layups, however. This suggests that the inter-ply nesting (or lack of) does not have a significant influence on the fibre re-organisation, as both laminates appear to be equally able to re-distribute the accumulated

compressive strain energy. Additional work, such as high-resolution imaging in a synchrotron may be able to investigate this phenomenon further in real-time, but unfortunately this is outside the scope of this thesis.
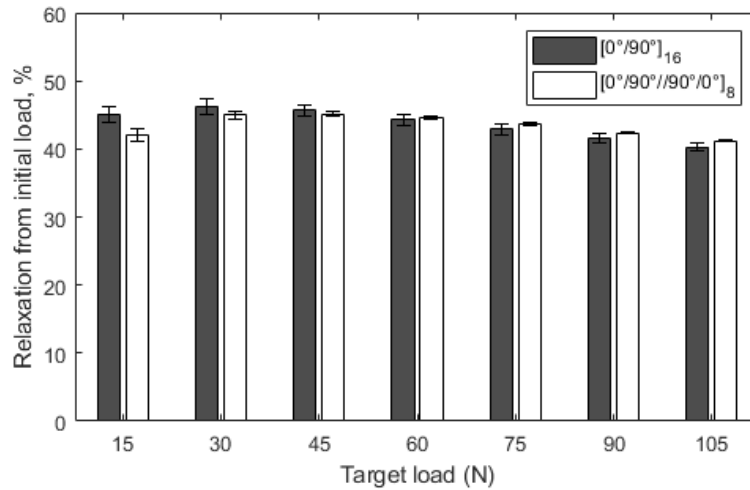
Figure 4.12 – Change in stress relaxation percentage across a 7-cycle load profile.

4.4 Chapter summary and conclusions

The compaction and nesting behaviours of a biaxial non-crimp fabric have been characterised using a standard through-thickness compression test. Results demonstrated that inter-ply fibre orientation has an effect on the compaction stiffness of a dry stack. Layups with parallel fibres at ply-ply interfaces exhibited lower compaction stiffness than those at any other angle, which presented very similar compaction responses. The effect of the number of plies was also investigated, showing that as the number of layers in a stack increases, the compaction stiffness decreases, because more nesting can be achieved.

Introducing an inter-lamina polymer veil eliminated the anisotropic compaction response of the fabric by way of inhibiting nesting. Consequently, inter-ply friction of the fabric was also observed to be isotropic, confirming the initial anisotropic behaviour is a function of nesting. Inter-ply sliding was seen to degrade the quality of the veil material, which should be of consideration when forming a component where such a material is expected to improve fracture toughness.

Optical microscopy was used to capture the nesting behaviour, having infused fabric samples with resin whilst held under vacuum pressure. This gave a representation of the nesting behaviour, further demonstrating that the surface topology of a ply-ply interface is highly dependent on fibre orientation.

The viscoelastic relaxation behaviour of the laminate was analysed, finding the relaxation behaviour to be highly dependent on strain rate. Slower rates produced less relaxation, as fibres were able to reorganise within the structure. The effect of cyclic loading on relaxation was investigated, but longer relaxation periods are required to fully explore the relaxation behaviour during a cyclic loading profile.

5. An investigation of the relationship between friction and compaction behaviours

5.1 Chapter outline and research aims

This chapter aims to establish the relationship between the multi-ply deformation mechanisms analysed in the previous two chapters: macroscale inter-ply friction and multi-ply compaction. The former presented that the frictional behaviour of a biaxial NCF was anisotropic due to the nesting mechanisms presented in the latter. Whilst important to understand, this phenomenon is of only minor significance to an actual DDF process, as it is unlikely that substantial levels of inter-ply slip will occur between plies of the same orientation. The pressure dependency of the ply-level friction, however, is of much greater import, and an improved understanding of how biaxial NCFs deform under load will assist with mitigating and designing against frictionally induced defects in the future.

This chapter uses in-situ X-ray computed tomography (CT) to capture the mesoscale (yarn level) deformation of 16-ply laminates subject to a normal compaction load. To process the large quantities of data produced from the CT scans, a supervised segmentation model is used to identify, segment and classify the two yarn directions. The output of the model is then processed to extract parameters of interest to describe the deformation of the fabric. Finally, a numerical model is presented to analyse the relationship between the measured mesoscale inter-ply contact area and the macroscale friction.

5.2 Chapter methodology

The following section of this chapter describes the methodology used to gather CT data and subsequently estimate fibre volume fraction (V_f), fibre bundle aspect ratio and mesoscale inter-ply contact area to quantify fabric deformation under normal load. An analysis of the

model's training and efficacy is presented, and some strengths and weaknesses of using this process are discussed. Finally, the methodology for extracting the parameters of interest from the segmentation model output data is presented.

The in-situ compaction rig used in this study was developed and used in collaboration with Dr. Andrea Codolini at the University of Cambridge. The instance segmentation model used was an "off-the-shelf" model produced by Ultralytics. The implementation of the model, preparation of training data, and post-processing analysis was undertaken by the author.

5.2.1 Materials

As per the previous chapters, the reinforcement fabric used in this study was FCIM359, a pillar stitched biaxial NCF provided by Hexcel Reinforcements, UK. The relevant material properties for FCIM359 can be found in Table 3.1.

5.2.2 X-Ray CT procedure

To apply the required compressive load in-situ of the X-Ray CT microscope, a custom-made test rig was designed, as shown in Figure 5.1. The rig uses acrylic rather than aluminium for many of the components, to minimise X-ray attenuation (and subsequent image noise) in the CT data. For example, the fabric specimens were sandwiched between spacers within the platens, both of which were made of acrylic. The rig was designed as an isolated unit, and so the compaction load was applied using a screw mechanism on a bench top before the rig was transferred to the microscope. An integrated load cell was used to measure the compaction load applied, which was calibrated using a certified Instron universal testing frame. The load was applied manually, using a stopwatch to approximate a 1 mm/min

compressive strain rate. When the relaxation of the fabric was estimated to have stabilised based on the data gathered in Chapter 4, the rig was transferred for subsequent scanning. Defined by time restraints on access to the CT microscope, the applied loading regime is shown in Table 5.1.
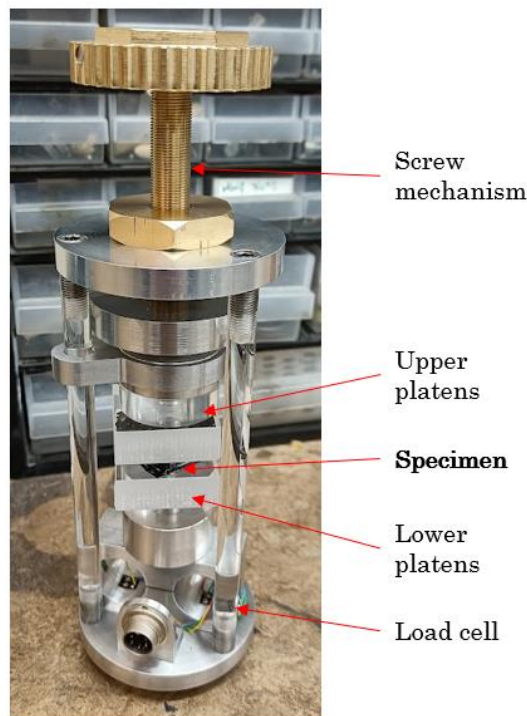
Figure 5.1 – Diagram of compaction test rig designed to apply compressive load to a fabric sample in-situ of an X-Ray CT microscope.

Table 5.1 - Loading regime for CT scans, shown in load applied and resultant pressure on the fabric samples.

Scan #	1	2	3	4	5	6	7
Load (N)	15	30	45	60	75	90	105
Pressure (kPa)	16.67	40	62.22	84.44	112.2	134.4	164.4

A Zeiss Xradia 510 Versa 3D X-ray microscope (XRM) was used to conduct the in-situ computed tomography work, support and access to which was provided by a Royce@Cambridge external funding grant. For each tomograph, the XRM acquired 1024 projections, having an exposure time of 2 seconds. The effective pixel size of the images was approximately 13.25µm. To capture large volume scans at such high resolution, a wide-angle optical lens of 0.4x magnification was coupled to the detector (2000 x 2000 pixels). Figure 5.2 shows the set up within the XRM, with key components indicated.
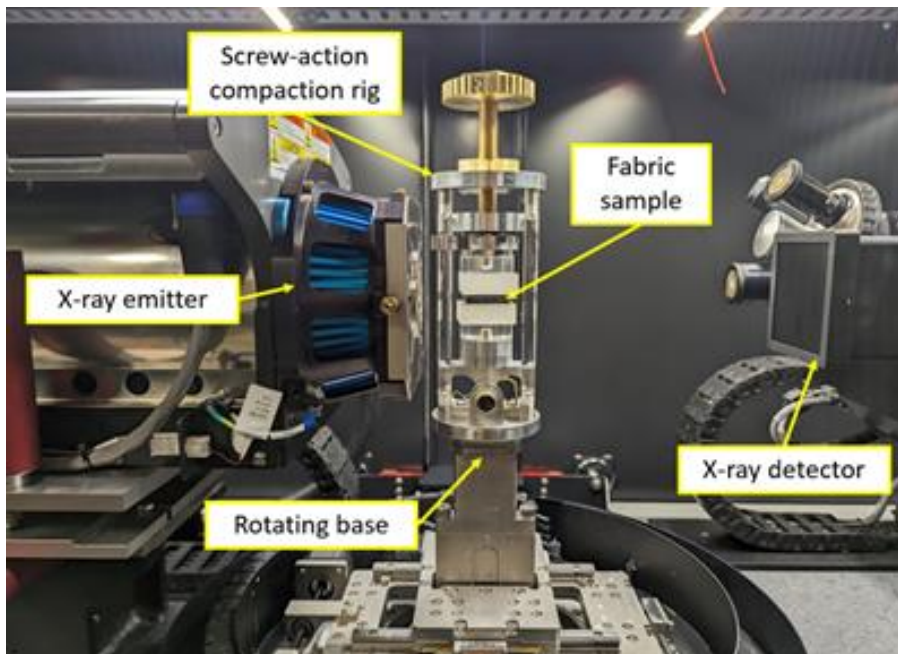
Figure 5.2 - Image of the test set up used for the CT work, with critical components labelled.

The 2D projections obtained were then reconstructed to create a three-dimensional representation. No nominal beam hardening correction was applied during the reconstruction process. The reconstructed data was exported as a stack of TIFF images, which was

then analysed using the commercial software VGStudioMax 2022.4. A Gaussian filter with a size of 3x3x3 voxels was applied throughout the volume to enhance the sharpness of the boundaries between the fibre bundles. The data was finally exported as 1000 slices along the loading plane. Figure 5.3 shows an example output of the post processing; fibre bundles that cross the image (left to right) are designated the longitudinal direction, with the opposing direction (into the image) being designated the transverse direction.
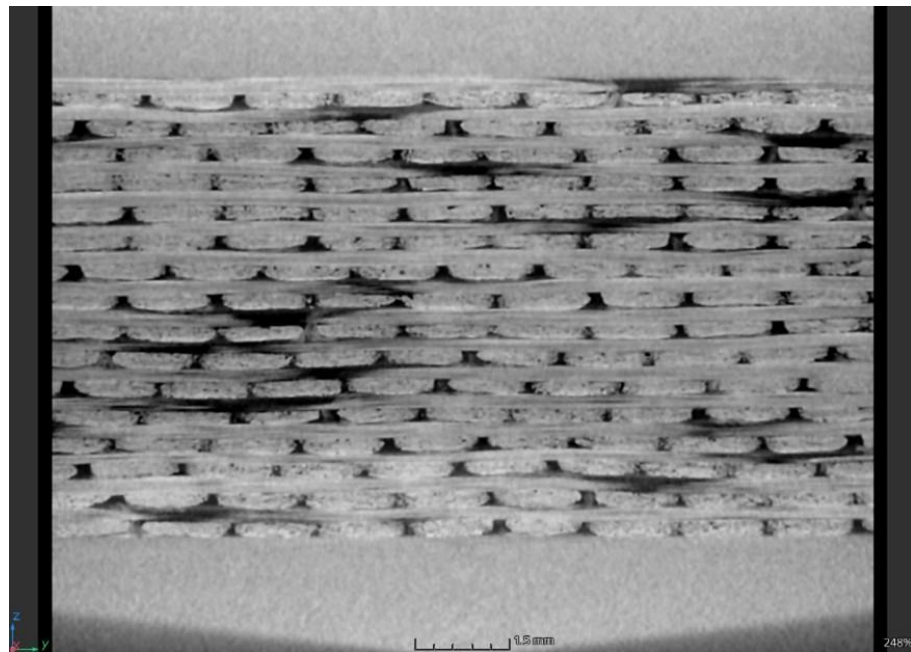
Figure 5.3 - A post-processed CT image of a $[0°/90°]_{16}$ laminate of FCIM359, subject to a 15N compressive load.

5.2.3 Instance segmentation model

Machine learning was used to process the CT data, as the similar X-ray absorption rate of carbon fibre and air produces images that are difficult to segment using more traditional methods, which are more suitable for glass fibres or resin infused composites [239–242]. An off-

the-shelf approach was taken to the computer vision work, in the interest of time and quality. The Ultralytics YOLOv8 framework [243,244] was used to identify, segment and classify the transverse and longitudinal fibres in the CT scanner images. YOLOv8 provides various model scales tailored to specific applications and hardware requirements, striking a favourable balance between speed and accuracy [245]. Moreover, it boasts a user-friendly implementation with Python integration and comprehensive documentation.

Figure 5.4 describes the process of training and implementing the model to extract the identified parameters of interest from each tomography scan. Following the post-processing of the raw images, 25 images were annotated manually using PyLabel to train and validate the model. This was a very time-consuming process, as the boundary of every fibre bundle in the image must be delineated by a polygon and classified with the appropriate longitudinal or transverse label. Each image was annotated by the author to eliminate the influence of any annotator bias [246]. The images were chosen at random across every load profile and thickness, in order to maximise the quality of the training dataset. To maximise the number of training images, the dataset was augmented by mirroring about the Y-axis, flipping about the X-axis and applying additional gaussian blur, producing a final training dataset of 200 images and associated annotations. 80% (160) of these images were designated for training use and the remaining 20% used for validation.
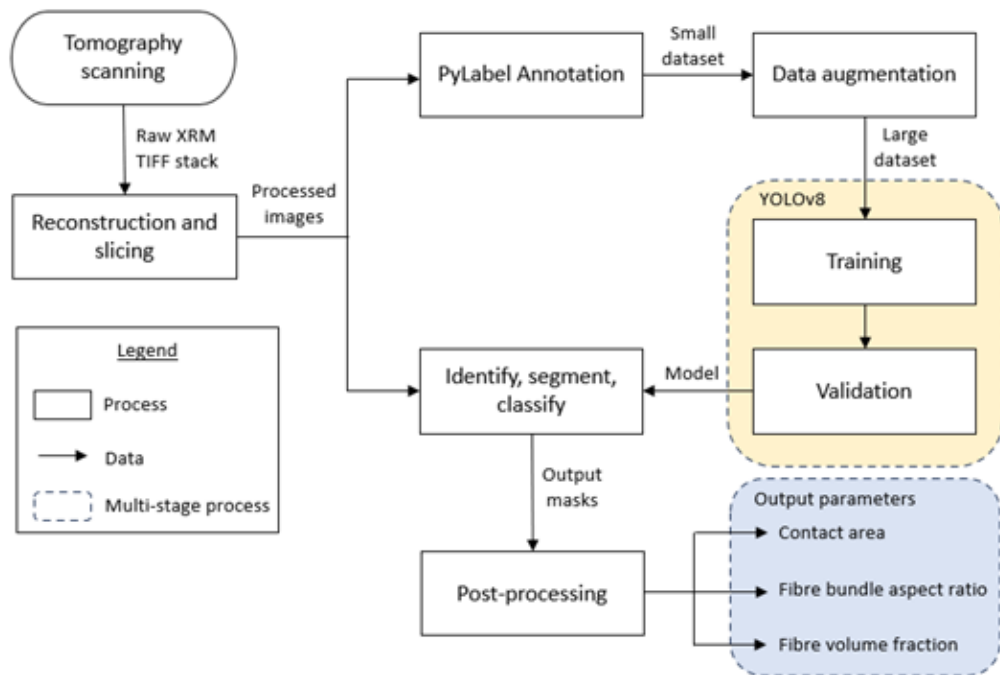
Figure 5.4 - Simplified workflow of the instance segmentation process used to extract parameters of interest from XRM data.

5.2.4 Model training and efficacy

The segmentation model was trained using the Google Colab Pro, which grants access to powerful NVIDIA A100 Tensor Core GPUs. The maximum resolution of the images Google Colab was able to use to train the model was only 800 x 800 pixels, which does limit the quality of the output data.

Figure 5.5 shows how the segmentation loss function improves with each epoch, quantifying the discrepancy between the predicted segmentation output and the ground truth segmentation of the validation dataset, providing a measure of how well the model is performing. The exponential decrease in both the training and validation loss curves signifies the model's ability to progressively learn and improve its performance throughout the training process.

The similarity between the two curves, along with their convergence to a plateau, indicates that the model is successfully generalising to unseen data and is not suffering from overfitting. This observation highlights the model's capacity to capture the intricate segmentation patterns present in the data, resulting in enhanced accuracy and similarity between the predicted and ground truth segmentations. The plateauing of the loss curves also assists in identifying the optimal epoch where the model achieves its peak performance without excessive training that could result in overfitting.
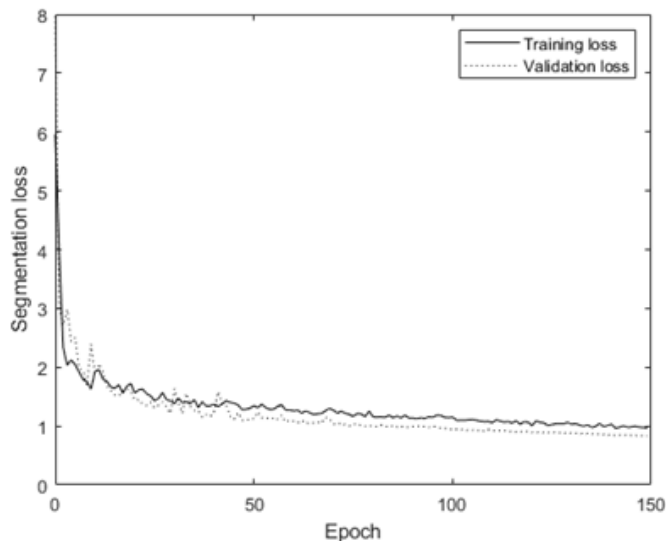
Figure 5.5 – Segmentation loss versus epoch for the YOLOv8 segmentation model.

To further analyse the efficacy of the model, the output segmentation masks can be investigated. Figure 5.6a shows the segmentation model applied to the same post-processed image shown in Figure 5.3. When once again utilising Google Colab Pro, the prediction model demonstrates commendable efficiency, with an average inference time of approximately 15 ms per image. This remarkable speed enables the model to process a substantial number of images within a

constrained timeframe, showcasing its capacity for high-throughput image analysis. The model is very effective at segmenting transverse fibre bundles, successfully identifying all complete bundles within this specific image.

Incomplete transverse bundles at the edges of each image were not included when annotating the training data, and are therefore not isolated by the model. Longitudinal fibre bundles are also well segmented; however, a small minority of regions have been missed and some appear to have been identified as multiple instances of slightly varying lengths. The latter issue is not considered significant, as post-processing is undertaken on a pixel-by-pixel basis, as shown in Figure 5.6. Each individual mask is coloured according to its associated label (blue for transverse fibre bundles and green for longitudinal fibre bundles) and saved to a composite image, isolating the fibrous structure from any complex background elements, such as stitching, tomography artifacts or the acrylic platens. This simple output can then be exported for later post-processing.
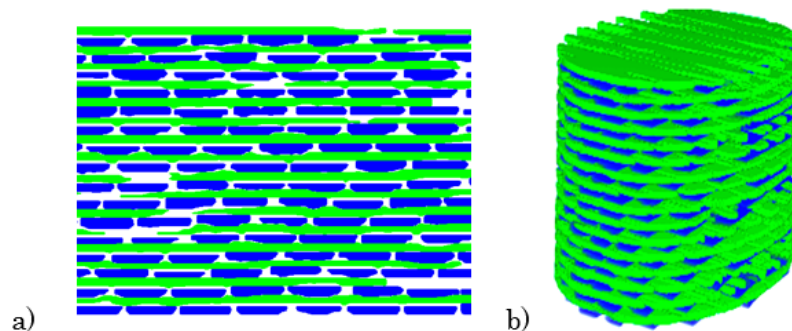
Figure 5.6 – a) Output from the segmentation model for the 15N load case. The masks are isolated from the unwanted background image and saved to a composite image according to their classification (blue – transverse fibre bundles or green – longitudinal fibre bundles). b) 3D reconstruction of machine learning output produced using 3D Slicer 5.2.2 software, where fibre directions are also colour-coded blue or green.

It is important to understand the limitations of the segmentation model to properly contextualise the output results. The model has more difficulty segmenting longitudinal bundles than transverse fibre bundles due to the unbalanced nature of the dataset - each CT image contains a maximum of $16 - 22$ longitudinal bundle sections but can contain up to 6 times as many transverse bundles due to the cross-sectional orientation. This results in the training dataset containing significantly more transverse instances than longitudinal, potentially causing the model to be biased towards the former when deployed. Consequently, detail is occasionally lost on longitudinal instances, or sections of the fibre bundle missed when segmenting. Future work on this topic may consider a method to reconstruct the laminate scan from both the coronal and sagittal orientations to re-balance the training dataset and improve the accuracy of the segmentation model, particularly when considering the quality of the longitudinal (green) fibre bundles.

Plotting the F1 score of each class (and the combined classes) against confidence thresholds, as shown in Figure 5.7, gives another indication that the model has more difficulty segmenting the longitudinal than the transverse fibre bundles. The F1 score is a metric that balances precision (how many predicted segments are actually relevant) and recall (how many relevant segments are correctly identified) by calculating their harmonic mean. It is particularly useful when the dataset is imbalanced, as it considers both false positives and false negatives. The confidence threshold represents the confidence value above which a prediction is considered positive. It can be seen that for any given confidence threshold, the accuracy of the longitudinal instances is lower than that of the transverse instances, which have a very high and consistent F1 score. The maximum F1 score of all classes was found

to be 0.88 at a confidence threshold of 0.43, where the transverse and longitudinal F1 scores were 0.96 and 0.80 respectively. However, this does not necessarily represent the optimum confidence threshold value for the segmentation model, as it is deemed more important that recall is maximised, rather than precision, capturing the greatest possible number of both transverse and longitudinal instances.
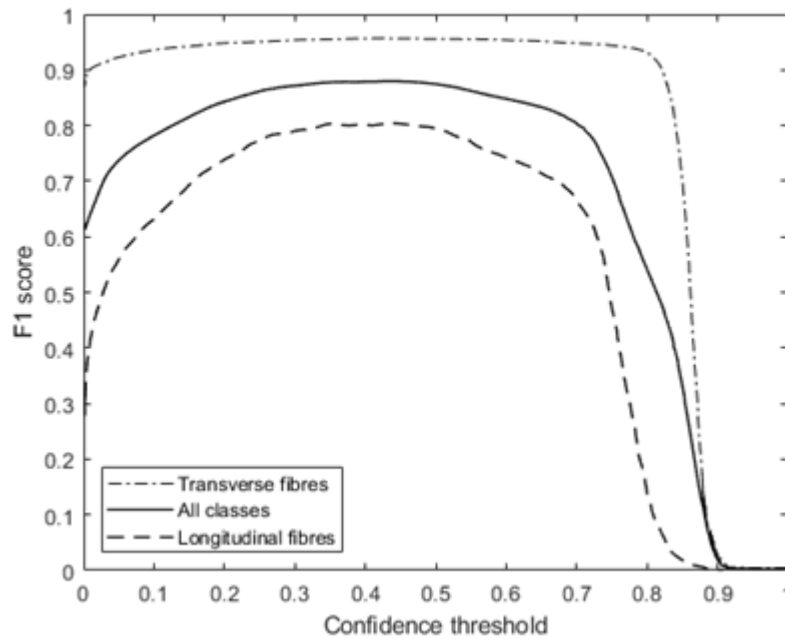
Figure 5.7 - F1 score versus confidence threshold for transverse fibre bundles, longitudinal fibre bundles and the mean of both classes combined.

A final drawback of the model that must be considered is one of human error as the training and validation dataset was annotated manually. Any systematic error introduced at this stage of the ML process will be carried forward into the final predictions. Future work may consider employing an increased number of researchers to annotate training data to reduce the significance of this systematic error.

5.2.5 Post-processing of model output

The aspect ratio of transverse bundle cross-sections, fibre volume fraction and inter-ply contact area were identified as measures of fabric deformation when under load. In particular, mesoscale inter-ply contact area was used to attempt to explain the pressure dependency of inter-ply friction observed in Chapter 3, as it is proportional to the number of asperity contacts that resist inter-ply sliding (see Section 2.4.3).

Post-processing of the output images (such as the one shown in Figure 5.6a) is conducted using MATLAB. Figure 5.8 describes the post-processing procedure. After determining the fibre volume fraction, each individual output image from the segmentation model is divided into the two respective fibre orientations (Step 2 in Figure 5.8). The aspect ratio of the transverse bundles is used as a measure of how the cross-section deforms as the load is applied. It is extracted from the isolated transverse masks by considering the dimensions of the bounding box of each polygon, which is determined using an in-built MATLAB function.

To calculate the contact length in each image, further processing is required. Now that additional noise and unwanted features have been eliminated, it is possible to use a traditional canny edge detection algorithm, another in-built function of MATLAB, to delineate each polygon (Step 3 in Figure 5.8). This produces a binary image where the boundary of each instance is represented by a white border with a width of a single pixel. Since FCIM359 is a biaxial NCF, the intra-ply contact area between the two fibre directions is not considered relevant to the inter-ply friction as it is assumed that no sliding occurs within each ply during a forming process. Therefore, only the contact length between each ply is of significance and edges of the polygons

that do not contribute to this can be discarded (Step 4 in Figure 5.8). For the orientation of plies used, this constitutes the top edge of the transverse instances, and the bottom edge of the longitudinal instances.
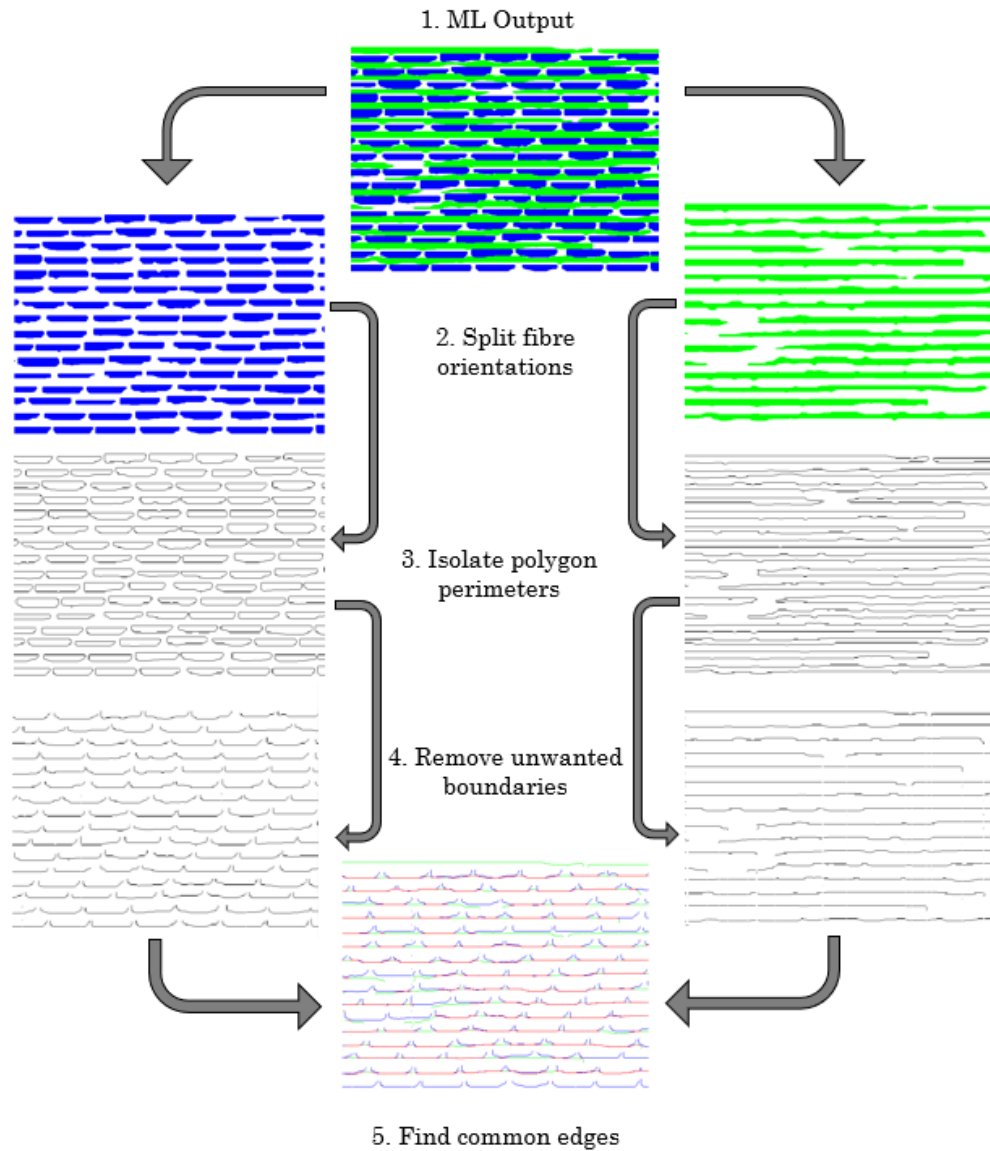
Figure 5.8 - Post-processing of ML output images to obtain estimated contact areas.

Finally, the remaining lines from both the longitudinal and transverse instances can be superimposed into a single image for comparison (Step 5 in Figure 5.8). A sensitivity analysis to determine how close a pixel from each fibre direction needs to be to be considered "in contact" is discussed in Section 5.3.3.

Figure 5.9 shows the complete number of transverse and longitudinal bundle instances detected by the post-processing method for each load case. A small negative gradient can be seen, suggesting the model has more difficulty defining the bundles as the applied compaction load increases. This is likely due to fibres within bundles commingling as their aspect ratios increase, therefore becoming more difficult to distinguish clear boundaries. The greatest total number of bundles (15 N compaction load) was found to be less than 6.7% larger than the smallest (105 N compaction load). To compensate for this small difference, the final inter-ply contact area values have been normalised according to the number of average bundles detected at each load increment to create an even dataset.
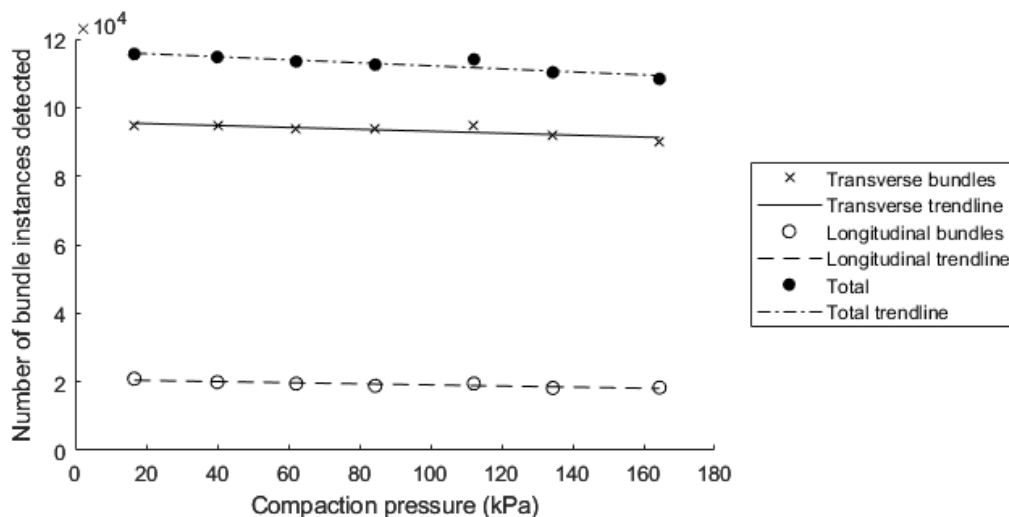
Figure 5.9 - Number of transverse and longitudinal instances captured by the complete ML process.

5.3 Processing and results

5.3.1 Fibre volume fraction

The fibre volume fractions of the laminate under varying compaction pressures are used to analyse the material deformation and to validate the ML approach. As the output of the ML model only considers the fabric structure at the mesoscale, estimations of intra-yarn (local) volume fractions are required to correct the macroscale V_f values. Some basic assumptions are made when estimating these values:

- Fibres are assumed to be parallel along the length of the yarn.
- All fibres are assumed to be perfectly cylindrical.
- The influence of stitches on V_f is ignored.
- Every bundle has the same V_f, and V_f is evenly distributed throughout each bundle.

Two packing arrangements are considered for the intra-yarn fibre arrangement [247] – square (as shown in Figure 5.10a) and hexagonal (as shown in Figure 5.10b). The maximum possible V_f for each case is 0.785 and 0.906 respectively [248]. The variation in V_f as a function of applied load was estimated using the trends and calculations presented in Section 4.3.1 of this thesis, as the project timescale did not allow for a full analysis, such as that conducted by Gommer et al. [249]. The estimated trend of increase intra-yarn V_fs obtained aligns with that seen in other work by Gommer et al. [250].
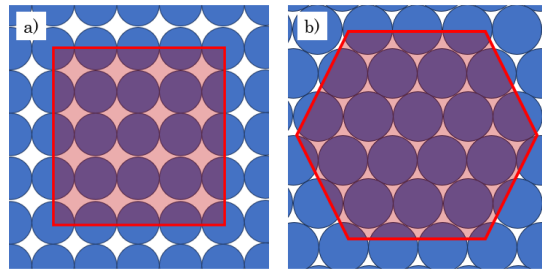
Figure 5.10 – Packing arrangements considered for intra-yarn V_f – a) square packing and b) hexagonal packing.

A final assumption is made that the intra-yarn volume fraction also increases with applied normal load, as observed with the macroscale compaction behaviour in the previous chapter. Using a basic exponential reduction informed by macroscale experimental data produces an estimated minimum V_f of 0.6 in the given pressure range. Further microscopy of the FCIM359 samples used in section 4.3 was conducted to confirm the validity of this range. Binarizing the image (as shown in Figure 5.11) enabled calculation of intra-yarn V_f by simple pixel count (i.e., comparing the number of white pixels to the total number of pixels). This method has limitations that should be used to contextualise the values of V_f calculated, principally the resolution of the microscope and the influence of the resin on the packing of the fibres. As a result, it is likely that the local V_f observed using microscopy is lower than in reality. However, the V_f values produced by optical microscopy ranged in value from 0.57 to 0.68, with a mean value of 0.64, falling within the lower end of the estimated range.
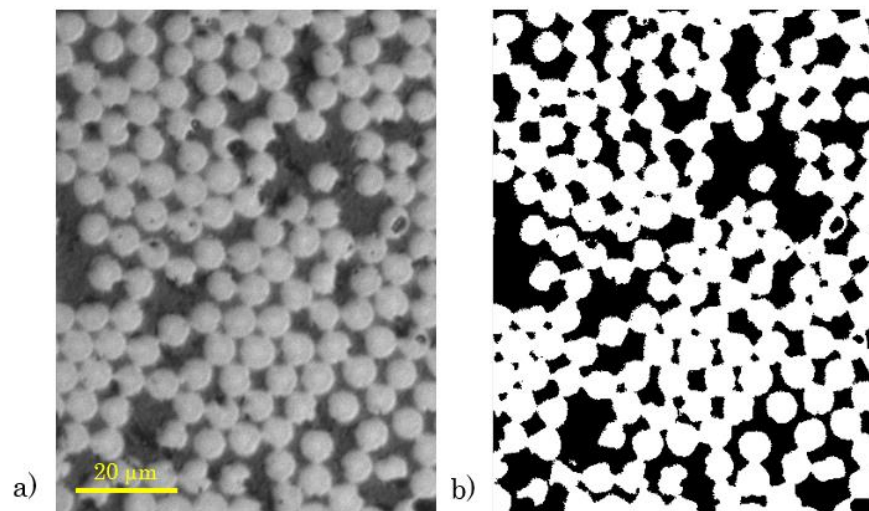
Figure 5.11 - a) Example microscopy image (20x) of FCIM359 fibres. b) Binarized image used to calculate intra-yarn V_f of sample.

The global fibre volume fraction of the laminate under each load is also determined from image by image on a pixel count basis. This is achieved by detecting the positive pixels at the upper, lower, left and right extremes, producing a global bounding box. The V_f of each individual image can then be defined as the ratio of the number of positive elements to the total number of pixels within the bounding box. Each global value is then adjusted to account for the intra-yarn V_f. Figure 5.12 shows the average volume fractions for both square packing (V_f^s) and hexagonal packing (V_f^h), alongside the values of V_f calculated numerically using Equation (4.1).
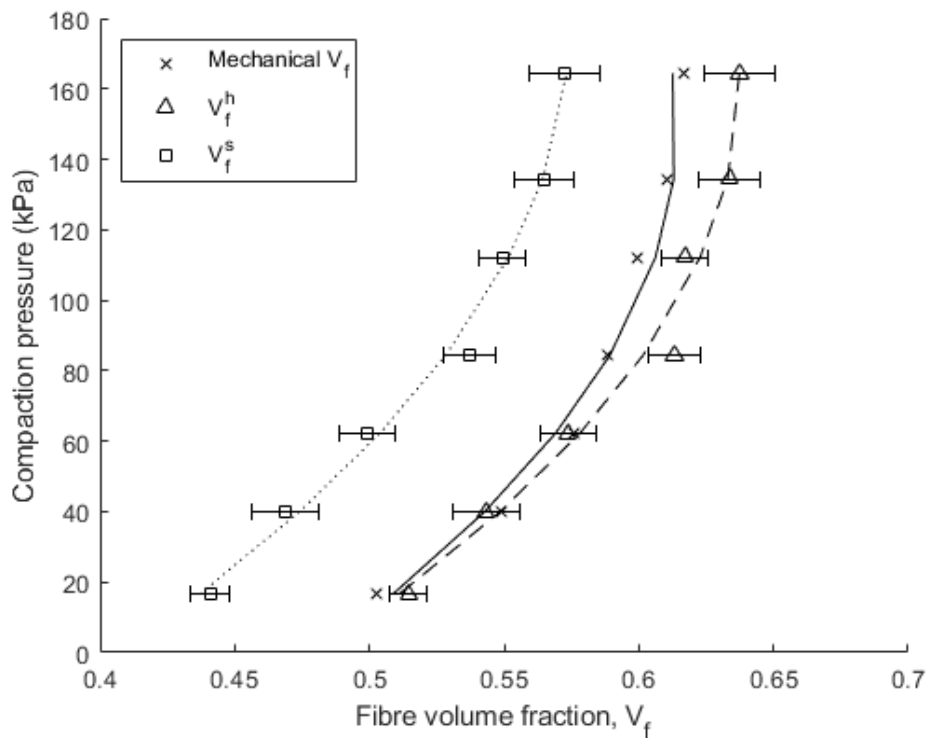
Figure 5.12 - Fibre volume fractions, calculated from platen displacement and estimated from ML output data using both square packing (V_f^c) and hexagonal packing (V_f^h). Error bars show ±1σ from the mean.

Assuming a square packing arrangement results in an underestimation of global V_f by an average of 10.3% (with a minimum of 7.2% and a maximum of 14.6%). Conversely, a hexagonal packing arrangement overestimates global V_f by an average of 2.1% (with a minimum of 1.1% and maximum of 4.0%). The smaller error suggests that assuming hexagonal packing may be more appropriate in this case. The slight overestimation in V_f^h may be a consequence of the low resolution of the bounding polygons that are used to segment each tomograph.

5.3.2 Aspect ratio of fibre bundles

To compare the deformation of transverse fibre bundles under different compaction loads, the change in aspect ratio (the width

divided by the height of a bounding box surrounding the bundle cross-section) is shown in Figure 5.13. Change in bundle height and width has previously been used as a measure of fabric deformation by Gommer et al. [249]. As the applied load increases, each transverse bundle widens and becomes thinner, increasing the aspect ratio and changing the cross-sectional shape. The increase in mean aspect ratio with compaction pressure follows a quadratic trend, as shown by the dashed trendline, producing an R^2 value of 0.91 indicating a very strong correlation between the two parameters. The entire data set was used to calculate each mean value, making the minimum sample size approximately 9×10^4 (as shown in Figure 5.9).

Like the observed behaviour of the fabric volume fraction, the rate of change of the transverse aspect ratios decreases as the applied compaction load decreases. This is caused by the increased compaction of the individual fibre bundles resisting further deformation; as the bundle Vf increases there are fewer spaces available in which fibres can restructure to disperse strain energy, and therefore the aspect ratio change decreases whilst the normal load rapidly increases.
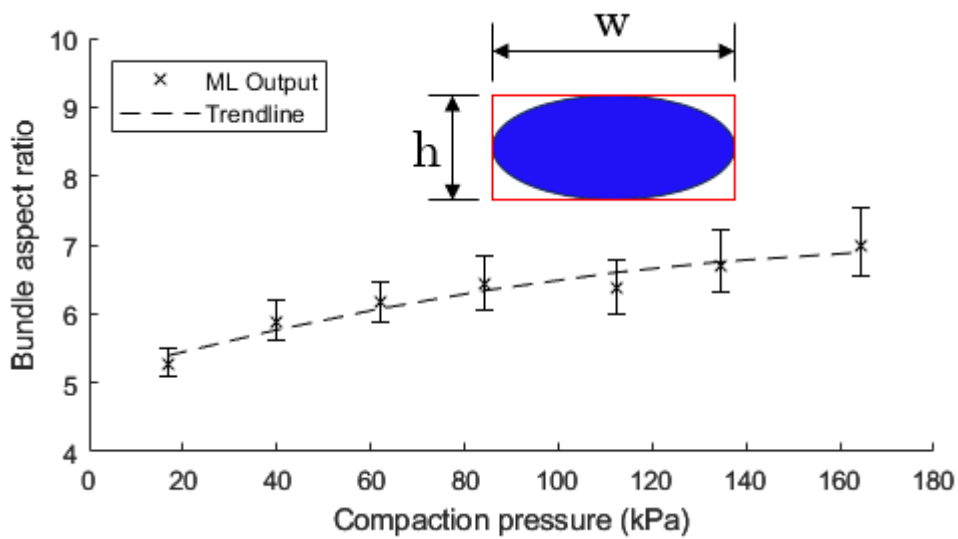
Figure 5.13 - Variation in transverse fibre bundle aspect ratio for each compaction load case. Inset diagram demonstrates the bounding box determination of width (w) and height (h) for aspect ratio of w: h. Error bars indicate the minimum and maximum aspect ratios of each sample, and a quadratic trend is indicated with a dashed line.

5.3.3 Mesoscale inter-ply contact area

Figure 5.14 shows the variation in the normalised contact area and compaction load for 3 different contact sensitivities. No error bars are presented on the figure as each value is a simple sum of the contact areas of each image in each stack. The values of contact area have been normalised to account for the small reduction in the number of bundles detected as compaction pressure increases (as shown in Figure 5.9). The first dataset considers only pixels from longitudinal and transverse edges that share exact coordinates to be in contact (i.e., they overlap). Based on the final output image resolution, this represents an estimated distance of approximately 8.3 µm. The second and third datasets consider a larger contact resolution of +1 and +2 pixels respectively, and as a result, both produce slightly higher

contact areas because a greater number of pixels are considered in the contact summation.
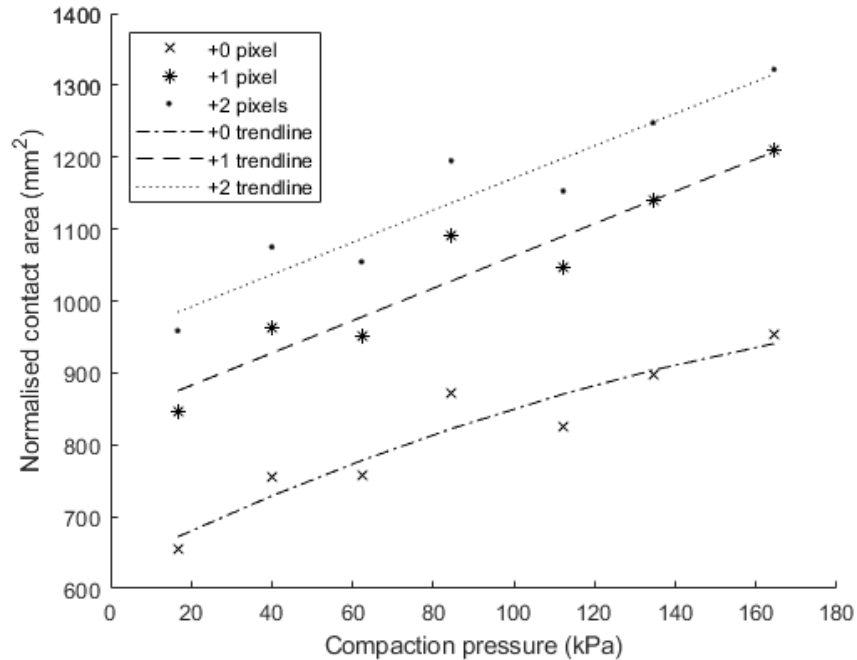
Figure 5.14 - Variation in normalised inter-ply contact area for 3 contact sensitivities: pixel overlap (+0 pixels), +1 pixel and +2 pixels. A quadratic trendline is indicated for the first case, and linear trendlines for the latter two.

The trendlines produced by these analyses are plotted as dashed lines on Figure 5.14. The rate of change of the contact area of the overlapped pixel sensitivity (+0 pixels) decreases as the load increases, agreeing well with the behaviour shown by the volume fractions and aspect ratios. The rate of increase of area reduces as the transverse bundles deform less with increased load, and the quadratic trend displayed produced an R^2 value of 0.90. However, the second two sensitivities follow a linear trend, each exhibiting strong R^2 values of 0.91. However, the overlapped pixel analysis follows a quadratic regression, with the rate of change of area beginning to plateau as the applied compaction pressure increases. The reason for

this difference in behaviour can be explained by analysis of the number of pixels that are included in the area summation at each sensitivity level, as shown in Figure 5.15.
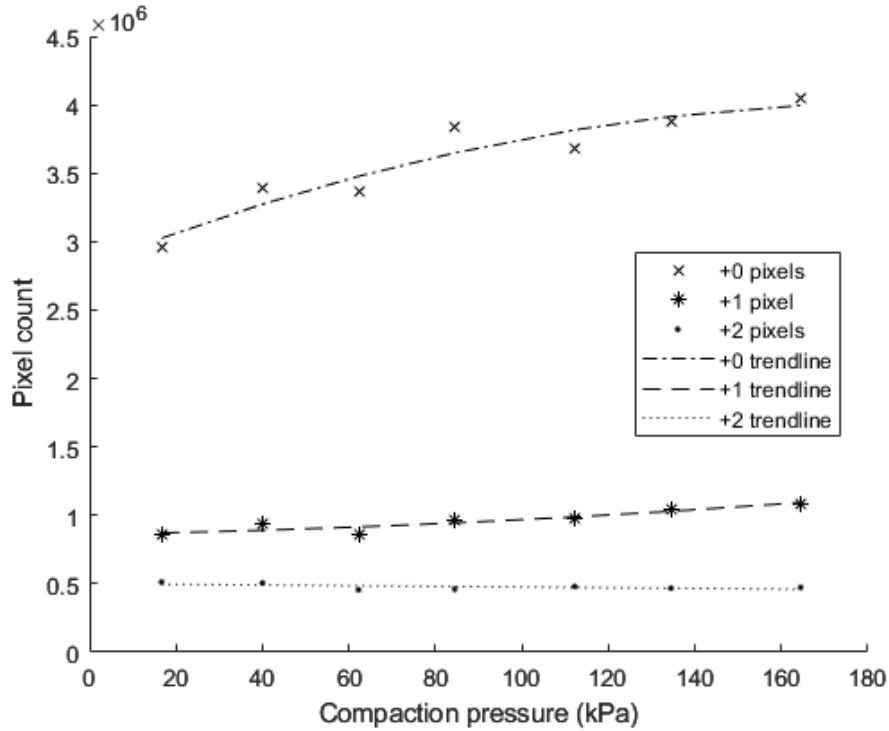
Figure 5.15 - Number of pixels considered to be in contact for 3 different sensitivities.

The majority of pixels considered in contact are those which overlap, accounting for approximately 72% of the total number of pixels under maximum compaction pressure. This generates the quadratic trend for the low sensitivity case shown in Figure 5.14. Although the +1 pixel sum is significantly lower than the +0, the opposing direction of the quadratic trend for the +1 pixels results in a more linear behaviour when included in the sum for total area. The reason for the increase in the number of +1 pixels is due to the change in shape of the transverse tow bundles as they deform: as they flatten from a

lenticular to rectangular shape, the vertical sides of each bundle move closer to the contact region. Despite this, the number of pixels at a distance of +2 from the interface exhibit a linear trend, once again producing a more linear behaviour in the contact area when included in the total sum.

5.4 Relationship between contact area and friction

In a "perfect" contact scenario, where each ply is in complete contact with its opposing partner, the scan volume used would be expected to generate an inter-ply contact area of 2084 mm². To establish the relationship between the observed inter-ply contact area and coefficient of friction, the measured contact areas were first normalised to a normalised coefficient of area (α), which can be defined as the ratio of the contact area calculated by the method outlined in this chapter to the theoretical perfect contact area, as per Equation (5.1):

$$Coefficient\ of\ area, \alpha = \frac{Observed\ contact\ area}{Perfect\ contact\ area} \tag{5.1}$$

Figure 5.16 shows the change in both α and coefficient of friction (μ) over a 0 kPa to 100 kPa pressure range to consider compaction loads representative of a DDF process. The values of α are assumed to be linear for the smaller pressure range, as the fabric has not yet begun to resist deformation. At 100 kPa, α is approximately 0.56, suggesting that, at vacuum pressure, the actual inter-ply contact area at the mesoscale for any flat area of FCIM359 at a 0°/90° interface would be expected to be only 56% of the given fabric surface. This result approximately aligns with a similar study by Mulvihill et al. [79],

who measured a real contact area of 32% at 260 kPa for a different (12K) carbon fibre tow. The resolution of images used in the study by Mulvihill et al. were higher than that used in this study (2048 x 1536 pixels versus 800 x 800 pixels), which combined with the lower tow weight may explain the difference in measured areas between the two.
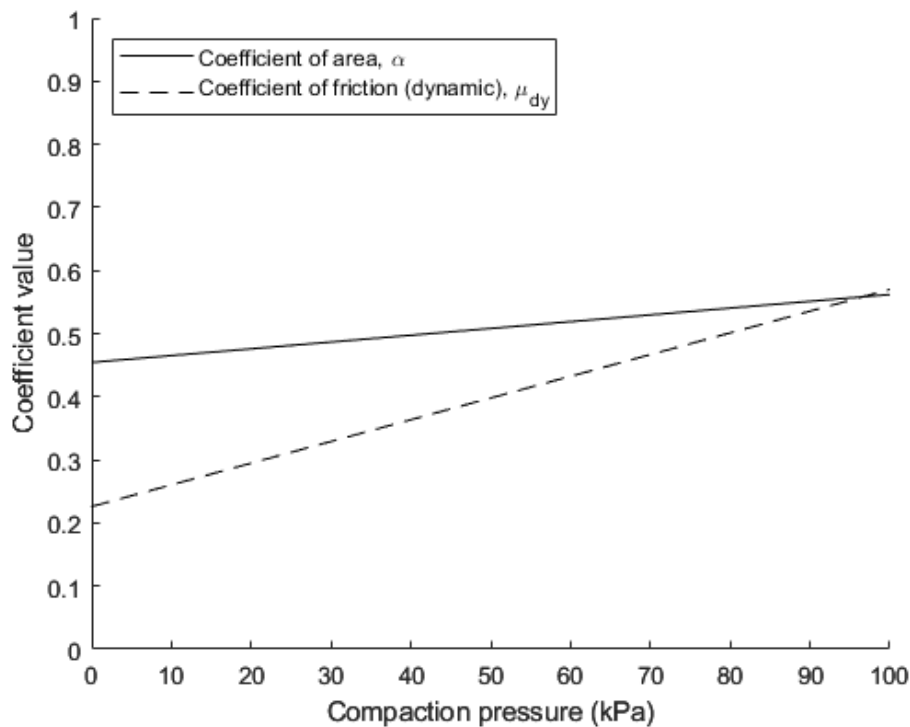
Figure 5.16 - Comparison of variation in coefficients of area and friction with applied normal compaction pressure.

The values of μ were determined using an overlap friction test, as discussed in Chapter 3. Like the trend in α over this pressure range, the increase in μ is linear – as the interface between the fabric samples deforms the coefficient of friction increases. However, it can be seen from the graph that μ is approximately 3 times more sensitive

to changes in pressure than α, the former exhibiting a gradient of $3.4\text{x}10^{-3}$ and the latter $1.1\text{x}10^{-3}$.

The 13.3 µm resolution of the CT images does not permit consideration of microscale inter-yarn intermingling, as a typical fibre has a diameter of 6 µm to 8 µm. Therefore, the microscale inter-ply contact area likely increases more severely with applied load than the mesoscale, agreeing more closely with the macroscale frictional measurements. Additionally, the method presented does not acknowledge the contribution to the sliding behaviour from the polyester stitches, which may further influence the frictional behaviour.

The relationship between estimated contact areas (A_{Real}) and frictional forces (F_f) can be described as a function of the applied compaction pressure. As the increase in area over the vacuum pressure range is linear, the behaviour can be described by the simple function in Equation (5.2), where k_1 is the gradient of the linear trend and c_1 is the estimated area when the material is not subjected to any compaction load. For comparison to experimental data, these values are determined using α and the contact area of the fabric samples used during the test. Equation (5.2) can then be multiplied by pressure to obtain the normal load at the interface, as shown in Equation (5.3).

$$A_{Real} = f_1(P) = k_1 P + c_1 \tag{5.2}$$

$$N = P \cdot A_{Real} = k_1 P^2 + c_1 P \tag{5.3}$$

The coefficients in each equation are determined from Figure 5.16. Likewise, since the increase in dynamic μ is known to increase linearly, it can also be described by a similar function in Equation

(5.4), where k_2 is the gradient of the second linear trend, and c_2 is the theoretical coefficient of friction when no compaction load is applied. A Coulomb friction law can then be used to establish the relationship between applied pressure and subsequent frictional forces for each surface, as a function considering both change in area (subscript 1) and μ (subscript 2), described by Equation (5.5).

$$\mu = f_2(P) = k_2 P + c_2 \tag{5.4}$$

$$F_f = \mu N = (k_1 P^2 + c_1 P)(k_2 P + c_2) \tag{5.5}$$

A comparison of the variation in estimated frictional forces with compaction pressure from the numerical model and experimental results is shown in Figure 5.17. The error bars on the experimental data represent one standard deviation from the mean, and the R^2 value of the quadratic fit is 0.99. It can be seen that the numerical model slightly overestimates the frictional forces produced by an average of 8.0%. One source of this error may be the quality of the ML output data: low image resolution and manual polygon boundary marking in the training process likely results in a small over-estimation of inter-ply contact areas, generating higher frictional forces than observed in reality. Future work may focus on a more accurate method of capturing fibre and bundle deformation, such as through the use of Digital Element models [251]. Despite this small error, the model agrees well with the experimental results, effectively relating the change in inter-ply contact area to increased frictional forces generated at the ply-ply interface.
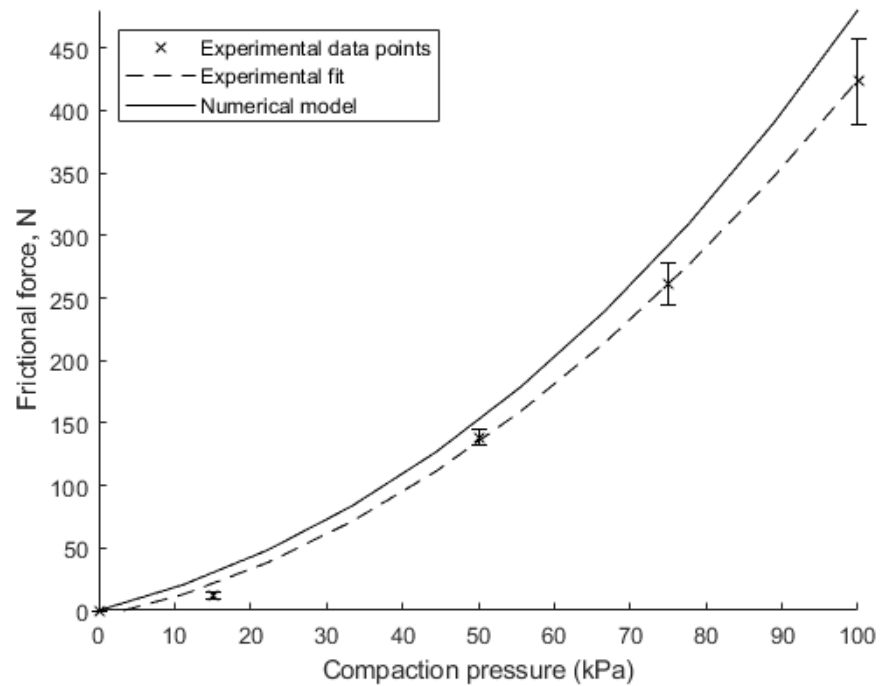
Figure 5.17 - Comparison of numerically estimated frictional forces and experimentally measured frictional forces from Chapter 3.

5.5 Chapter summary and conclusions

This chapter has attempted to explain the macroscale friction and compaction behaviours presented in previous chapters by analysing mesoscale fabric deformation mechanisms. Multi-ply dry NCF laminates were imaged in a μCT scanner to investigate the influence of fibre orientation and normal load on the compaction behaviour. Controlled normal load was applied in-situ using a custom made through-thickness compaction rig.

A methodology using machine learning techniques has been presented for processing CT data to estimate fibre volume fractions, tow deformation and inter-ply contact areas at the mesoscale. ML was used to overcome difficulties distinguishing carbon fibres from air

within CT data. The efficacy of the model has been analysed using conventional ML metrics, and the post-processing of its results to estimate the parameters has been discussed. The results estimated that the real mesoscale contact area between plies is 56% of the apparent contact area at vacuum pressure. Clearly there are some limitations with this model due to the number assumptions, which should be the focus of future work.

A numerical approach was presented that examines the relationship between μ and the change in real inter-ply contact area induced by an applied normal load, up to vacuum pressure (100 kPa). The model produced good agreement with the experimental results, slightly overestimating frictional forces by an average of 8.0%. Further meso and microscopic analysis of the contact interface is considered to be outside the scope of this thesis, but a brief microscale visualisation of the fabric surface using scanning electron microscopy (SEM) can be found in Appendix A – SEM Imaging of FCIM359.

6. The influence of inter-ply friction on NCF formability

6.1 Chapter outline and research aims

This chapter aims to investigate the influence of the friction and compaction deformation behaviours discussed in Chapters 3 and 4 on the macroscale forming of multi-ply NCF preforms, by means of both experimental and numerical analysis. This is achieved by analysing the bending and shear behaviours of multi-ply stacks in comparison to single ply samples, as well as investigating the formability of a larger scale component formed using DDF.

At the coupon scale, novel methods of adapting traditional bending and shear characterisation tests are used to accommodate multi-ply samples and subject them to load cases representative of a DDF process. The influence of inter-ply friction on bending stiffness and shear resistance is quantified both experimentally and numerically, and the effect of varying frictional forces through different layup sequences is presented.

Finally, a DDF case study is presented whereby the effect of the changes to in-plane shear and out-of-plane bending caused by high levels of inter-ply friction are demonstrated. The efficacy of an FEA process model is analysed and validated for a 2-ply case, before being used to predict the formability of 16-ply preforms.

6.2 Experimental methodology

6.2.1 Non-linear bending characterisation

Inter-ply friction influences the bending stiffness for multi-ply stacks, generating theoretical upper and lower bounds depending on the level of slip [252]. The upper limit, where friction is so high that no slip

between layers is possible, causes the stack to effectively bend as a solid beam. The second moment of area for this case is as follows:

$$I_U = \frac{b(nt)^3}{12} \qquad (6.1)$$

where b is the ply width, n is the number of plies in the stack and t is the thickness of each ply. The total second moment of area for the lower limit, where friction is absent so there is no resistance to inter-ply slip, is as follows:

$$I_L = \frac{b(t)^3}{12} \qquad (6.2)$$

The bending stiffness of most real-life multi-layer beams will fall somewhere between these two limits, depending on the coefficient of friction between the layers. A revised cantilever bend test was used to characterise the non-linear bending stiffness of multi-ply laminates, following a proven test methodology [71,72,76]. A Creaform Handyscan 3D Silver Series laser scanner was used to digitise the bending profile of the top ply of each sample in the form of XYZ point cloud data (Figure 6.1a). The resolution of the scanner was up to 0.1 mm. The overhang length of the test was fixed to be 200mm to obtain a sufficiently wide range of curvatures over each specimen. A white powder spray (Ambersil Flaw Developer 3) was applied to the material to minimise reflections from the laser scanner and to improve the quality of the scan data. No difference in bending behaviour was observed when the spray was applied. Only the central 10% of data points from each scan were used to produce a bending

profile, reducing the influence of any unwanted twist or rotation in the fabric. A deflection curve was obtained by fitting a 6th order polynomial to the data points for each sample, as per previous non-linear bending studies of the same NCF material [71].
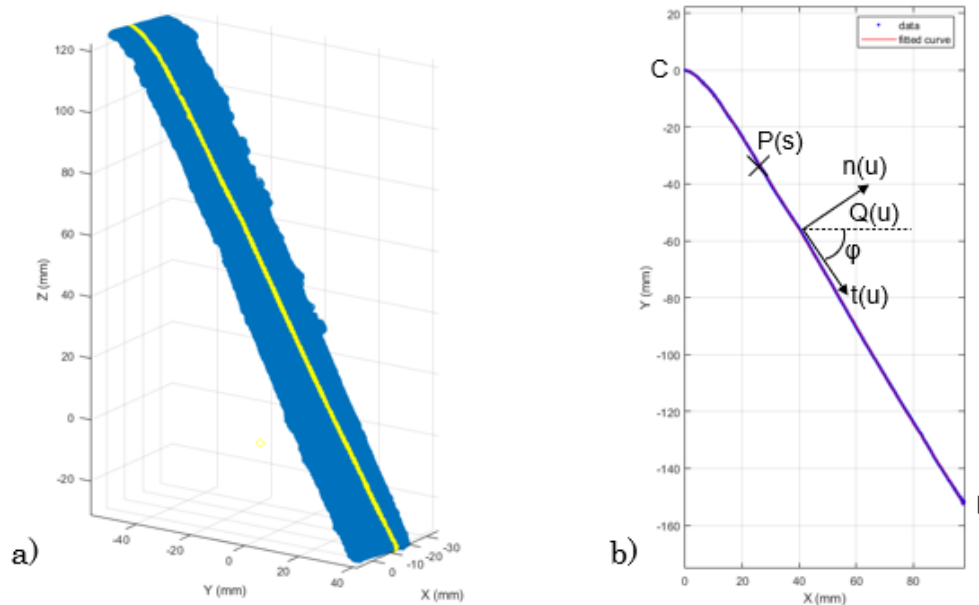
Figure 6.1 - a) Example scan of a single ply bending sample of FCIM359. b) Free body diagram of the extracted 2D bending profile.

As shown in Figure 6.2, loops of lightweight thread were added around the multi-ply specimens to prevent deconsolidation, but to still enable inter-ply slip, so to better represent a forming process. This was achieved by tying the thread loops loosely, so no compaction force normal to the surface of the samples was applied. The mass of the thread is considered negligible compared to the NCF specimen, and therefore it is assumed that any additional mass does not directly affect the bending stiffness, other than by encouraging resistance to inter-ply slip by way of friction. Through-thickness tufts were also investigated for the same purpose, as previously used by Liang et al.

[76], however the absence of crimp in the NCF material resulted in too much instability in the sample.

Figure 6.2 - A multi-ply bending sample of FCIM359. Pink loops of light-weight thread to prevent deconsolidation of the stack and reflective points used for the laser scanner can be seen.

As commonly found in the literature [72,223], the non-linear bending behaviour of FCIM359 is described as a function of the specimen curvature and the bending moment. To determine the curvature κ at any given point along the bending profile, Equation (6.3) was used, where y' and y'' are the first and second derivatives of the deflection curve with respect to X, as described by the free body diagram shown in Figure 6.1b.

$$\kappa = \frac{y''}{(1 + y'^2)^{\frac{3}{2}}} \tag{6.3}$$

To calculate the bending moment of the sample, first the accurate bending length of the deflection curve L_B was determined, as per Equation (6.4), where X_F refers to the X coordinate at the free end of the beam and X_C refers to the constrained end. L_B should be equivalent to the overhang length of the sample, which is 210mm for this case.

$$L_B = \int_{X_C}^{X_F} \sqrt{1 + y'^2} \, dx \tag{6.4}$$

From the bending length, the curvilinear abscissa s along the profile can be calculated, as shown in Equation (6.5). Point P (shown on Figure 6.1b), defined by $s = s(P)$, is the point about which the bending moment $M(s)$ applied by the beam PF and κ are determined.

$$s(P) = \int_{X_C}^{X_P} \sqrt{1 + y'^2} \, dx \tag{6.5}$$

Finally, Equation (6.6) is used to determine $M(s)$, where φ is the angle of the curve tangent to the horizontal, u is the curvilinear distance from point P to point Q, and W is the specimen weight per unit length.

$$M(s) = W \int_{s}^{L_B} (u - s) \cos(\varphi) \, du \tag{6.6}$$

The resulting curvature versus bending moment relationship can be described using Voce's model as per Equation (6.7), where R_0 and R_{Inf}

are fitting constants and κ_{lim} is the exponential saturation parameter.

$$M(\kappa) = (R_0 \cdot \kappa) + R_{Inf}(1 - \exp{(1 - \frac{\kappa}{\kappa_{lim}})}) \qquad (6.7)$$

6.2.2 Multi-ply shear characterisation

A bias-extension test was selected to characterise the in-plane shear behaviour of a multi-ply laminate subjected to varying levels of through-thickness compaction. The picture frame shear test (Section 2.7.1) was not used, as additional non-shearing material could not be easily included in the test. The bias extension test methodology is described extensively by Cao. et al [167]. A shear angle (γ) versus shear force (F_{Sh}) curve was obtained from each experiment to describe the shear behaviour of the fabric, calculated using Equations (6.8) and (6.9).

$$\gamma = 90 - 2\cos^{-1}\left(\frac{(H - W) + \delta}{\sqrt{2}(H - W)}\right) \qquad (6.8)$$

$$F_{Sh}(\gamma) = \frac{1}{(2H - 3W)\cos(\gamma)}\left(\left(\frac{H}{W} - 1\right)F\left(\cos\left(\frac{\gamma}{2}\right) - \sin\left(\frac{\gamma}{2}\right)\right)\right.$$
$$\left. - WF_{Sh}\left(\frac{\gamma}{2}\right)\cos\left(\frac{\gamma}{2}\right)\right) \qquad (6.9)$$

where H and W are the height and width of a fabric sample, δ is the crosshead displacement, F is the crosshead load and F_{Sh} is the shear force normalised per unit length.

The fabric samples for the bias extension test were placed inside a vacuum bag to simulate the compaction pressures experienced during DDF (Figure 6.3). The force required to shear the sample and extend the vacuum bag can be described by Equation (6.10) [253]:

$$F_{Sh} = F - F_d - F_f \qquad (6.10)$$

where F_d is the load required to extend the vacuum bag and F_f is the frictional force between the vacuum bag and the fabric sample.
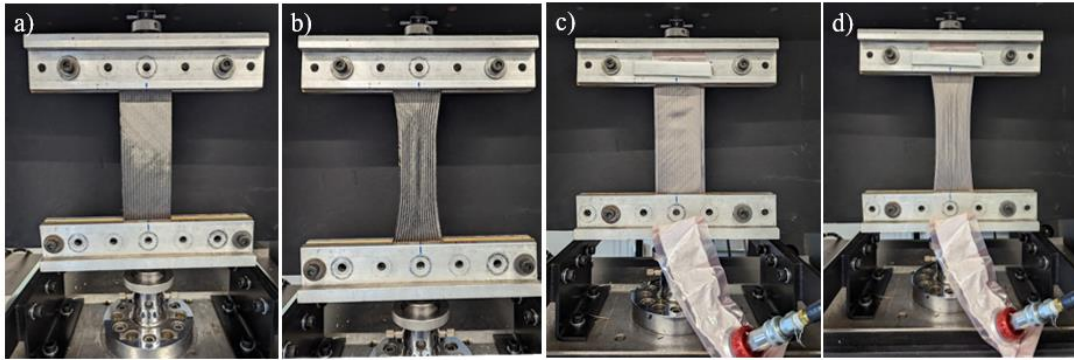
Figure 6.3 – Bias extension tests of a single ply of FCIM359. a) Pre-test, no vacuum. b) Post-shearing, no vacuum. c) Pre-test, induced vacuum. d) Post-shearing, induced vacuum.

Additional NCF plies were included for some bias extension tests to investigate the influence of inter-ply friction on the intra-ply shear behaviour. These fabric plies were orientated at [0°/90°] and were shorter than the original [±45°] plies, as shown in Figure 6.4. They were therefore unconstrained (i.e., not clamped at either end) to avoid the unwanted tensile contribution from the [0°/90°] fabric in the measured crosshead force. The layup sequence of the resulting fabric stack was varied to change the number of sliding interfaces between

[0°/90°] and [±45°] plies. A drawback of this method is the coupling of displacements between the two fibre directions via friction, and therefore the loads measured will no longer be generated by perfect shear, and so can only be considered an indication of the influence of inter-ply friction, and not as direct input into a material model.
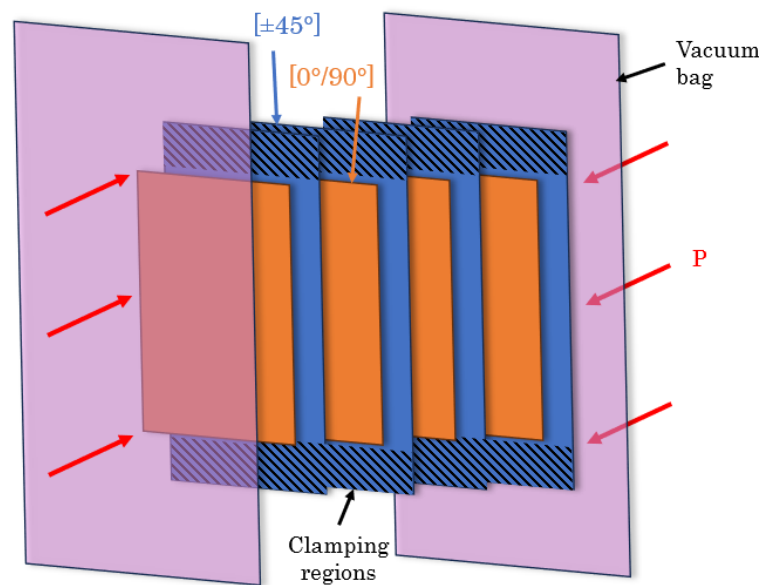
Figure 6.4 – Schematic showing an example sample set up for a multi-ply bias extension test to assess the influence of inter-ply friction on in-plane shear behaviour.

6.2.3 Double Diaphragm Forming experiments

A laboratory-scale double diaphragm forming (DDF) machine was used to conduct experimental forming trials. Stretchlon® HT-350 was used for the diaphragm material, with dimensions of approximately 1.8m x 1.5m. Relevant material properties of Stretchlon® HT-350 can be found in Table 6.3. The two diaphragms are clamped between three aluminium frames on the machine, which are then lowered into position over the male forming tool using four pneumatic cylinders.

Table 6.1 - Material properties of Stretchlon diaphragm material

Name	Stretchlon® HT-350
Material type	Thermoplastic elastomer
Elongation at break	>550%
Tensile strength	62 MPa
Maximum use temp.	162 °C
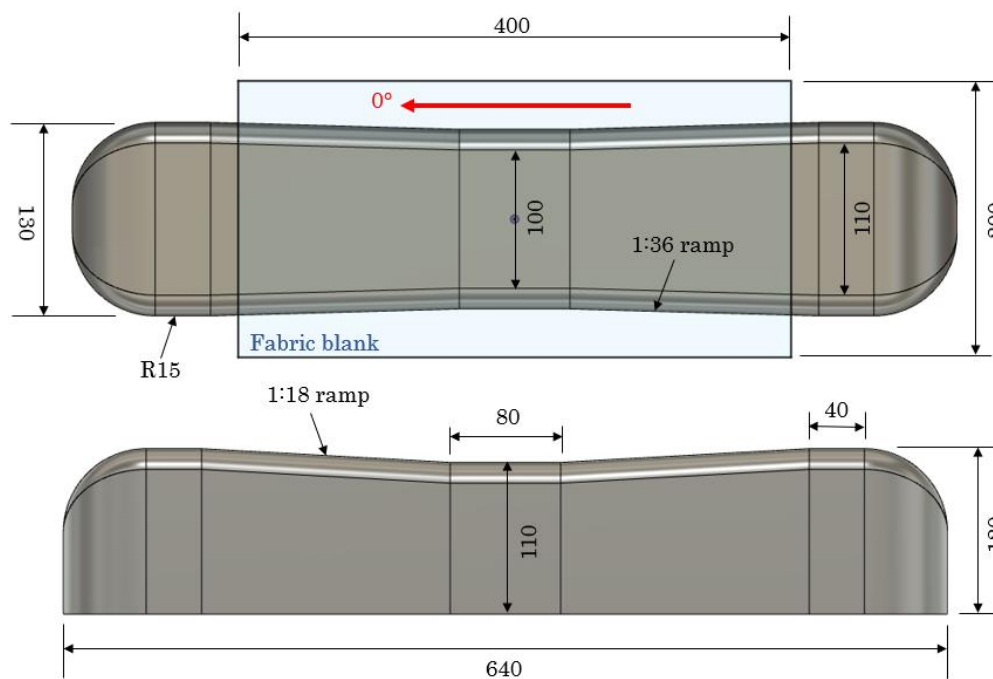
Figure 6.5 - Geometry of male C-spar tool and fabric blank position used for experimental study (dimensions in mm). The principal fibre direction is indicated with a red arrow.

The male tool geometry used for the forming work is displayed in Figure 6.5, which is similar to the geometry used by Johnson et al. [254]. The C-spar was selected as it is representative of a typical aerospace geometry that is typically difficult to form, including sections with double curvature. A fabric blank size of 200 mm x 400 mm was used for both the experiments and the numerical simulations

and was aligned centrally with the spar geometry as shown in Figure 6.5. The longitudinal axis of the spar was designated the 0° fibre direction.

The Creaform laser scanner was used to digitise the geometry of the final DDF preforms. In-situ scanning within the DDF machine was conducted with the diaphragms in place (instead of stabilising the preform with binder and removing from the tool) to eliminate the effect of any uncontrolled preform relaxation and to improve the rate at which preforms could be tested. Additionally, the reduced reflectivity of the diaphragm material compared to the surface of the carbon fibre preform produced significantly higher quality scanning data.

The geometry was aligned to the principal axes using Creaform VX Elements scanning software, based on the centre of mass, producing a result such as the one shown in Figure 6.6. The scan contained a portion of the tool surface, which was used to assist with the alignment of the digital preform to the original geometry. An iterative closest point algorithm in MATLAB was then used to align the preform with its original position on the tool, identifying the normal distance between the preform and the tool surface. This was used to normalise the wrinkle amplitudes across the range of preforms with different nominal thicknesses. A global average thickness was determined for each preform, which was subtracted from the local thickness at each data point to establish the height difference. This wrinkle amplitude is therefore independent of the number of plies in the preform, enabling direct comparison between preforms of varying thicknesses. The same method was used for both the experimental forms and results from the numerical model to ensure consistency.

Figure 6.6 - Workflow for in-situ preform wrinkle amplitude measurement. The tool geometry (1a) and preform scan (1b) are aligned using an iterative closest point algorithm (2). The normal distance between the two surfaces is used to calculate conformity and wrinkle amplitude (3) which is then represented as a colour map on the preform geometry (4).

6.3 Finite element methodology

6.3.1 Material modelling

The pre-existing material model used to simulate deformation of FCIM359 in this thesis has been validated in several previous studies [44,71,218,255]. The model is implemented in Abaqus/Explicit, by using the Composites Layup toolbox to apply a user defined VFABRIC material subroutine. As discussed in Section 2.8.4, each ply is represented by 3 layers to decouple the bending stiffness from the out-of-plane stiffnesses. This membrane-shell structure can be described by the schematic shown in Figure 6.7.

A membrane element (M3R4D) with a through-thickness single integration point is sandwiched between two, much thinner, shell elements (S4R), used to control the bending behaviour, which use 3

integration points to model bending. The membrane elements have 12 degrees of freedom (DoF), and the shear elements have 24.
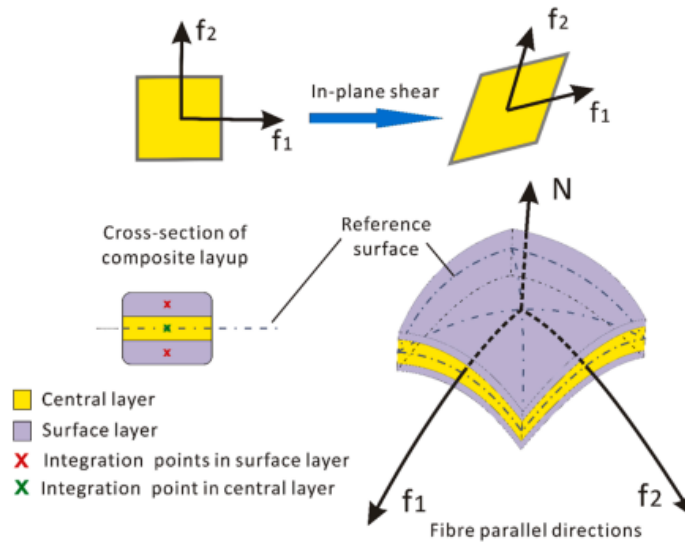
Figure 6.7 – Schematic of the FCIM359 VFABRIC material model used for FE process modelling [223].

The central membrane element layer considers the in-plane behaviour using a non-orthogonal constitutive relation [62], whilst the two outer shell layers are used to define the non-linear, asymmetric bending behaviour. A mesh consisting of elements with a 3.0 mm edge length was used for all fabric instances. The modulus of the fabric in the fibre direction was assigned to be 3 GPa to limit axial strain, as recommended by Harrison et al. [256], and a small mass scaling factor of 350 was applied to reduce the run time of the model.

6.3.2   DDF process modelling

Each ply of the multi-ply stacks was modelled as an individual FE mesh, positioned centrally between two rectangular diaphragms, representing the experimental setup. The diaphragm material was implemented using the Marlow model for hyperelastic materials, defined using previously validated experimental data [218]. The tool bed and geometry, as well as the constraining walls, were modelled as rigid bodies.

The compaction and draping loads were applied to the model in several steps, as shown in Figure 6.8. During the first time step (Origin to A in Figure 6.8) a pressure of 0.1 MPa was applied to the surfaces of both the top and bottom diaphragms at the same rate but in opposite directions. This pressure is maintained for a short period whilst the fabric stack consolidates (A to B in Figure 6.8). The pressure applied to the bottom diaphragm is then gradually reduced, causing the diaphragm and fabric assembly to drape over the tool surface (B to C in Figure 6.8).
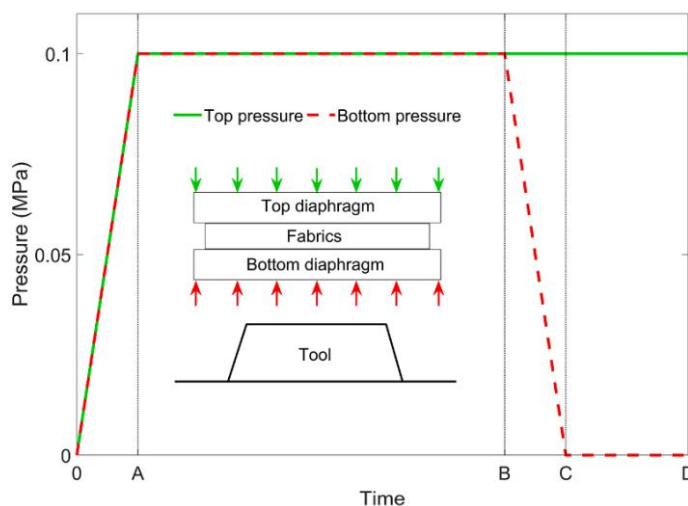
Figure 6.8 - Graph describing pressure variation for the top and bottom diaphragms as a function of time [218].

In contrast to process modelling of single or two-ply laminates, the influence of the inter-ply interactions in multi-ply forming can have a significant influence on the formability of a component as the magnitude of the total frictional forces in the stack are much higher. Therefore, it is important to model inter-ply contact as accurately as the available computational resources allow. For simplicity, the contact behaviour for the macroscale forming model can be divided into tangential and normal behaviours within Abaqus/Explicit (i.e., friction and compaction responses).

The inter-ply frictional behaviour is implemented as a pressure-dependency using the standard Abaqus/Explicit penalty friction algorithm. The experimental data for input into this model was generated in Chapter 3. Although this study showed that the inter-ply frictional behaviour of FCIM359 was also dependent on relative fibre orientations across the ply-ply interface, this behaviour was not represented in the model. The frictional forces at parallel fibre interfaces were shown to be considerably higher than any other angle. However, since plies with parallel fibres are likely to deform via the same mode, the relative slip between them is negligible. Therefore, in the interest of computational efficiency, the inter-ply frictional behaviour is considered to be pressure-dependent but isotropic.

The pressure-dependent response of the material model was validated using a simple sled test simulation, the results of which confirmed a change in coefficient of friction aligning with experimental results. The sled test simulation also enabled the comparison of general and surface-to-surface (S2S) contact algorithms, as shown in Figure 6.9. The coefficients of friction generated by each interaction were very similar (within 0.57% of each other), but the frictional forces

generated by the general contact algorithm were a lot noisier. However, this noise was not observed to have any effect on the DDF simulations discussed later, and the reduced computation time and simplicity of the application of the general contact algorithm make it a more suitable choice for large-scale forming simulations. Additionally, S2S contact requires the definition of a master and a slave surface, which are determined by larger and smaller mesh densities respectively. Similarly, the relative stiffnesses of the surfaces in contact are also important, with the master surface typically being the stiffer of the two. Therefore, S2S contacts are not appropriate for inter-ply interactions where each ply has the same element size.
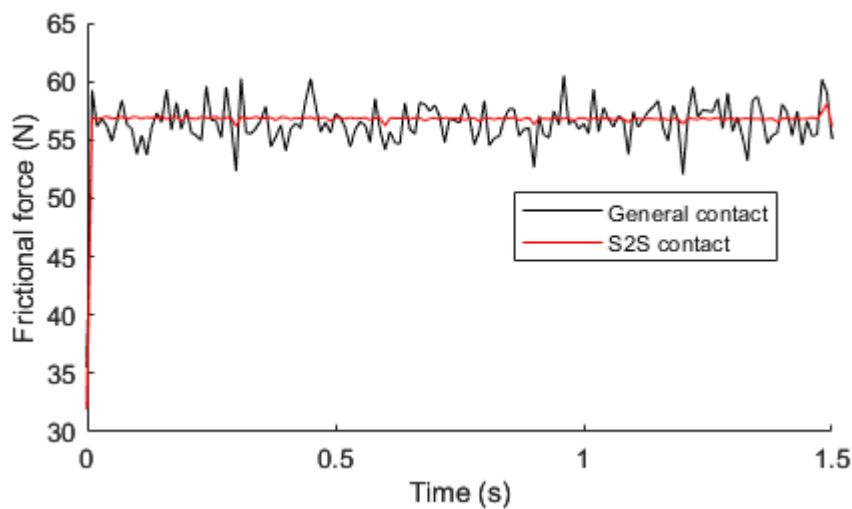
Figure 6.9 - Frictional forces generated by sled test simulations for general and surface-to-surface (S2S) contact algorithms.

6.4 Characterisation results

6.4.1 Multi-ply non-linear bending behaviour

The bending stiffness of a single ply of FCIM359 is described by the bending moment per unit width versus curvature relationship shown in Figure 6.10a. The mean root mean square error (RMSE) between the fitted curve and the experimental data was found to be 4.2% up to a curvature of 0.12 mm^{-1}. These results agree with previous bending characterisation of the same fabric [4]. Figure 6.10b describes the non-linear bending behaviour of a single ply of FCIM359, where the bending stiffness decreases as curvature increases. The initial bending stiffness at 0 mm^{-1} curvature was found to be 0.0076 Nm.
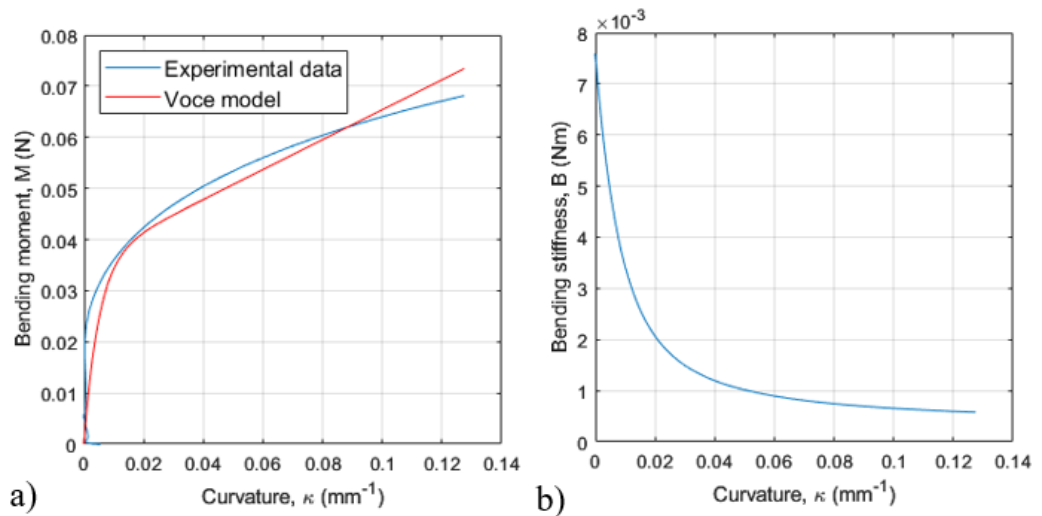
Figure 6.10a) Bending moment per unit width versus curvature for a single ply of FCIM359. b) Bending stiffness per unit width versus curvature for a single ply of FCIM359.

The multi-ply stack exhibited non-linear bending behaviour similar to the curves produced for a single ply. However, for samples of the same length, the multi-ply samples produced a smaller curvature range due to the resulting increased bending stiffness. The bending behaviour for a multiply stack is shown in Figure 6.11, where for a given curvature, the bending moment for a $[0/90]_{16}$ bending sample is greater than the summation of the bending moment for each individual ply in the stack. The R_0, R_{inf} and κ_{lim} bending parameters for each case, as defined by Equation (6.7), can be found in Table 6.2.

Table 6.2 – Bending parameters of tested FCIM359 laminates, as defined by Equation (6.7).

Description	Single ply	16 x single ply	Multi-ply
Layup	[0°/90°]	16 x [0°/90°]	[0°/90°]$_{16}$
R_0	0.2927	4.6908	1.5818×10^{-4}
R_{inf}	0.0361	0.5772	1.4240
κ_{lim}	0.0049	0.0049	0.0083

This difference is defined as the frictional moment (M_{Fric}), and has previously been observed by Liang et al. [76]. It is caused by the inter-ply friction in the laminate and is a significant component of the overall bending moment. This friction inhibits sliding between plies as they bend, effectively increasing the overall second moment of area of the system and subsequently increasing the perceived bending stiffness [252].
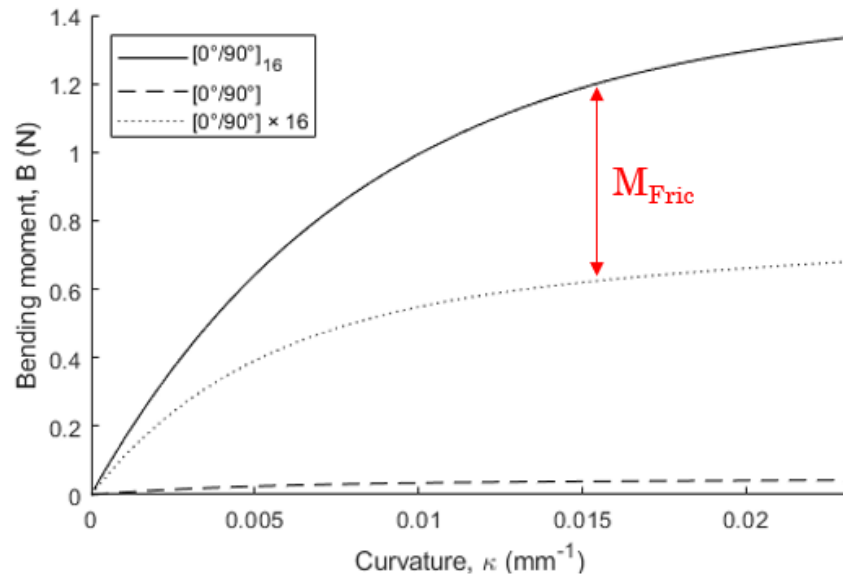
Figure 6.11 - Curvature-bending moment per unit width curves for a 16-ply sample, a 1-ply sample and a 16-ply summation of 1-ply of FCIM359. The difference between 16-ply and 16-ply summation is indicated in red as the frictional moment.

Figure 6.12 shows the variation in the friction moment with curvature for the same 16-ply test (the difference between the solid and dotted black lines in Figure 6.11), which naturally follows a non-linear relationship. The highest values of the friction moment can be seen when the curvature is at its largest, which occurs near the constrained end of the sample. The frictional moment contributes a significant proportion of the total bending moment of a multi-ply stack, up to 51% at the maximum curvature value of 0.023 mm^{-1}. Therefore, any changes to the coefficient of friction at the interfaces between plies (such as those generated when normal load is applied) are expected to have an effect on the bending stiffness of the ply stack.
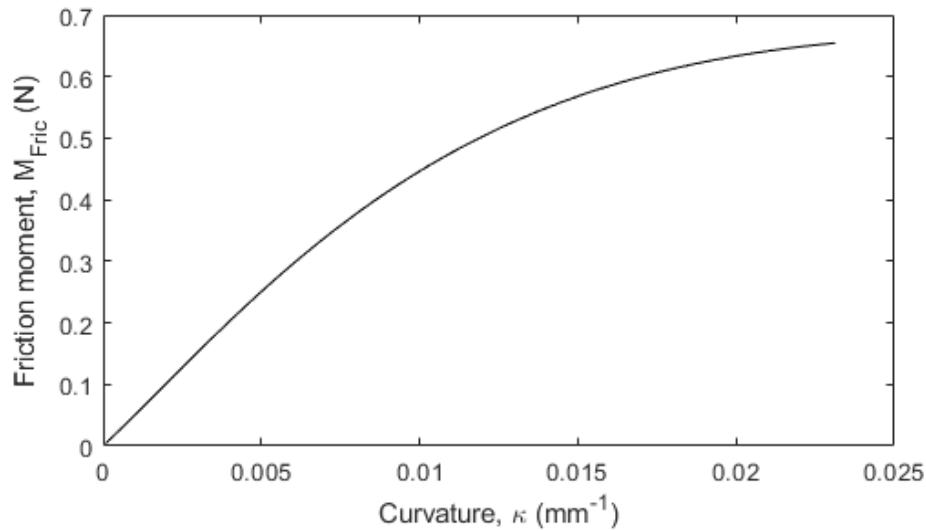
Figure 6.12 – Curvature versus friction moment of a 16-ply sample

The experimental multi-ply bending data presented has been used to investigate the validity of the FE approach used in previous studies when considering the bending behaviour of thick laminates. When modelling a multi-ply cantilever bend test, additional connectors are included to represent the thread loops used in the experiment. Abaqus/Explicit enables the use of axial connectors, which constrain motion within defined limits along the axis of a line connecting two or more nodes. The positions of these connectors are represented by the red lines shown in Figure 6.13, which also shows an example of the subsequent deconsolidation of the stack when the connectors are absent at low compaction pressure.
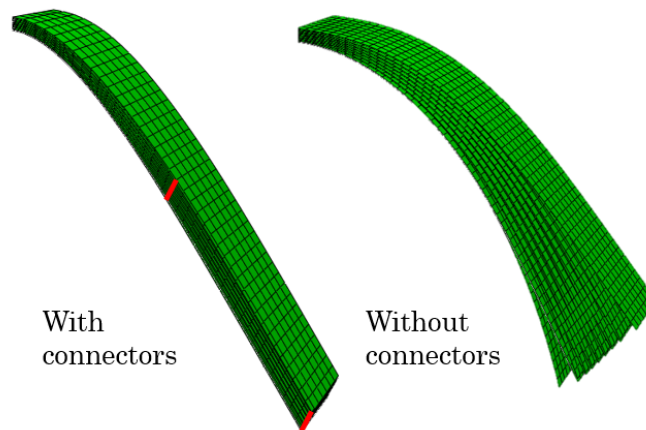
Figure 6.13 - Left: Example FE model of a multi-ply bending test using axial connectors, the positions of which are highlighted in red. Right: The same test without connectors, exhibiting deconsolidation.

The bending profiles generated by the multi-ply cantilever bending simulations are shown in Figure 6.14, for two 16 ply layups - $[0°/90°]_{16}$ and $[\pm45°//0°/90°]_8$. The dashed lines in Figure 6.14 show the bending profile of the sample with the original, single ply bending data (as per Figure 6.10a). The original model (with standard Coulomb friction) does not effectively capture the increased stiffness of the multi-ply stack, resulting in greater levels of ply curvature. This is due to how the material model updates the curvature of the elements within the ply. The bending stiffness of each layer within the laminate shell element is determined at the start of every time increment from a global data array containing fibre curvatures from the previous time increment, which is used to update the stresses and strains at each integration point [223]. The simulated bending stiffness is therefore unaffected by the inter-ply friction since the curvature of each element is independent of the tangential contact behaviour on the surface.

To capture the increase in bending stiffness caused by the inter-ply friction, the curvature-bending moment data has been updated to

account for the stiffer material stack, and the subsequent bending profiles represented by the solid lines in Figure 6.14. The updated model agrees well with the experimental range for both layup sequences. The drawback of this modelling approach is that experimental bending data is required for each layup with a different number of plies, requiring a global bending curve for each ply. Further research is required to establish the relationship between inter-ply friction and multi-ply bending more firmly, and to enable a more robust modelling approach.
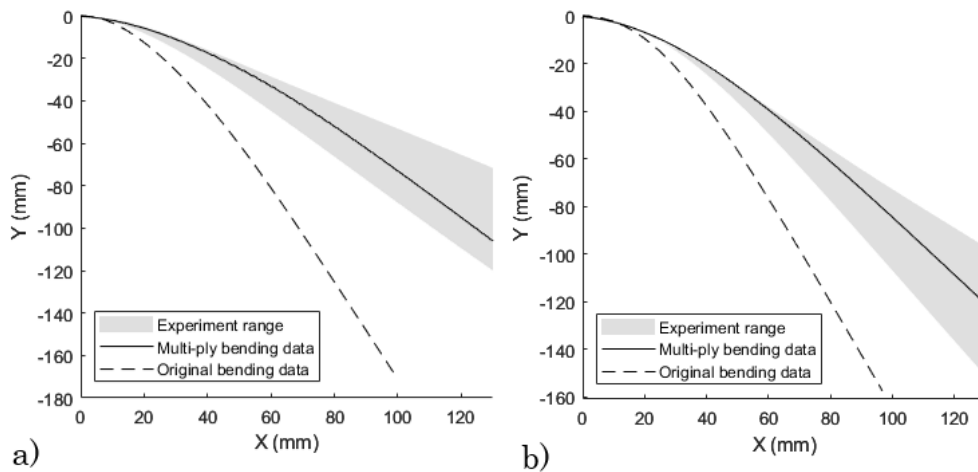
Figure 6.14 - Experimental ranges and simulated bending profiles of a) $[0°/90°]_{16}$ and b) $[±45°//0°/90°]_8$ laminates. The equivalent range of experimental results is shown in grey. Dashed lines indicate the profile of the original, single ply, bending stiffness, and the solid lines indicate the updated multi-ply bending stiffness.

6.4.2 Multi-ply shear behaviour

Figure 6.15 shows the normalised shear force versus shear angle curves for a range of FCIM359 multi-ply layups, produced from the modified bias extension shear test. All curves represent the mean of a minimum of 3 repeats. Error bars have been omitted in Figure 6.15

to improve clarity, but the mean coefficient of variation was found to be less than 1% in each case, indicating good levels of repeatability.

The layup exhibiting the lowest shear resistance was found to be a $[\pm45°]_8$ stack (green curve), which was subjected to atmospheric pressure only. The lack of normal load limits inter-ply surface interactions, avoiding any significant resistance to the shear behaviour of the fabric. When vacuum pressure is introduced the shear resistance of the 8-ply stack (black line) is consistently higher. At an arbitrary shear angle of 20°, the shear force is 26.23% larger for the specimen held under vacuum compared to the specimen at atmospheric pressure. This increase is caused by greater intra-ply friction between the yarns at the shear rotation points, since every ply is at the same orientation and they are shearing in the same manner, the amount of slip between plies is considered to be negligible.
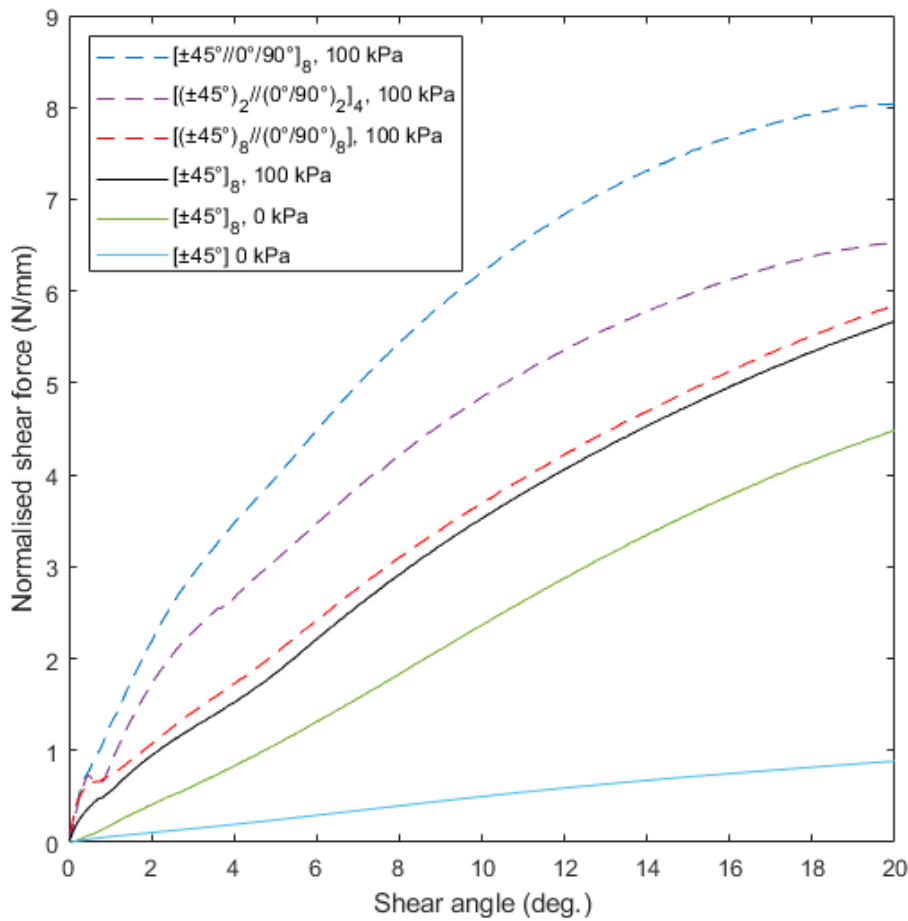
Figure 6.15 - Normalised shear force versus shear angle for a range of multi-ply FCIM359 layups and compaction pressures.

The introduction of 8 additional [0°/90°] plies (indicated by dashed lines in Figure 6.15) increases the magnitude of the inter-ply frictional force present, which is dependent on the number of interfaces between plies of different orientations. It is assumed that the [0°/90°] plies do not shear since they are not clamped. Friction at the [0°/90°] and [±45°] interfaces inhibits the shear deformation of the clamped [±45°] plies, increasing the overall shear resistance of the laminate. A "blocked" layup of [(0°/90°)$_8$, (±45°)$_8$] only has a single inter-ply interface where the ply orientations are dissimilar. The small increase in shear force for any given shear angle produced (3%

greater at a shear angle of 20°) is greater than the mean coefficient of variation of either sample, indicating the increase is due to the introduction of the [0°/90°] material. Increasing the number of inter-ply interfaces to 7 magnifies this increase in shear resistance, producing an increase in shear force of 15.23% at a shear angle of 20°. Finally, an "interleaved" layup of $[(0°/90°), (\pm 45°)]_8$ with 15 dissimilar ply-to-ply orientation interfaces results in a 42% increase in shear force at a shear angle of 20° compared to the $[\pm 45°]_8$ layup, producing a significantly less formable layup.

6.5 DDF case study

6.5.1   2-ply validation case

To assess the influence of friction on in-plane shear and out-of-plane bending behaviours during the forming of a multi-ply preform, a DDF study was undertaken using both numerical simulations and experiments. Using the C-spar geometry described in Figure 6.5, a 2-ply layup was used to validate the FE process methodology. Figure 6.16 shows the wrinkle patterns on the upper face of the C-spar geometry generated by the experiment and simulations of a [45°//0/90°] DDF preform. It can be seen that the standard method of modelling fabric-fabric interactions does not predict any out-of-plane wrinkling, disagreeing with the experiment. Including pressure dependent friction and soft contact modelling enables the simulation to effectively capture the location and the geometry of the lateral wrinkle but results in a small overestimation of its severity. The maximum amplitude of the wrinkle measured from the experiment was 1.04 mm, compared with 1.35 mm from the simulation, a difference of approximately 30%.
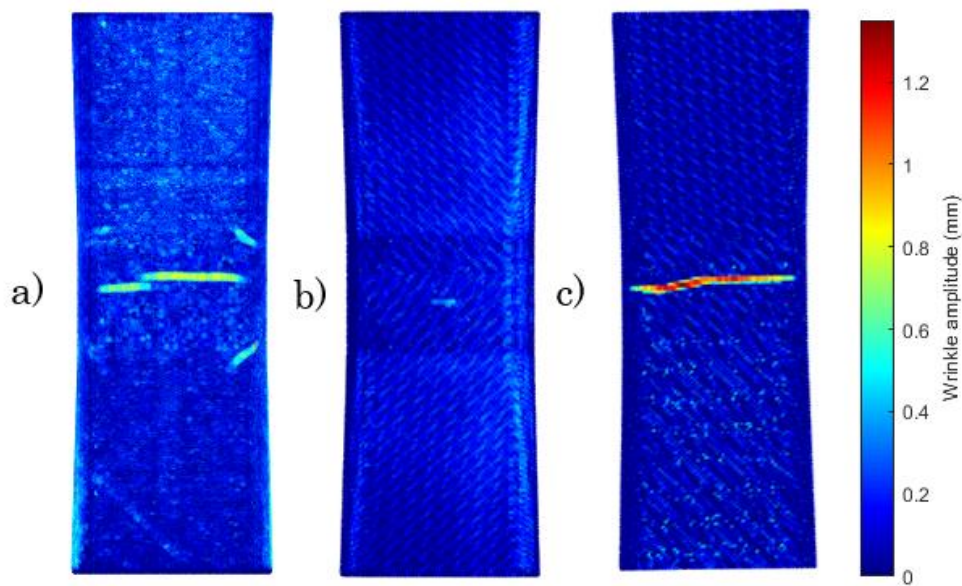
Figure 6.16 - [45°//0/90°] DDF preforms produced using a) experiment, b) simulation with standard interaction modelling and c) simulation with pressure dependent friction.

6.5.2 Effect of stacking sequence

A 16-ply laminate was used to investigate the effect of increasing the magnitude of the frictional forces within a fabric stack. This was achieved by using different stacking sequences, each using 8 plies at [±45°] and 8 plies at [0°/90°] relative to the longitudinal axis of the spar. These layups are described in Table 6.3. Each stacking sequence generates a different number of inter-ply slip interfaces (SI) to generate different levels of relative motion between the plies. As shown in Table 6.3, it is possible to generate laminates with 5 different numbers of SI (1, 2, 3, 7 and 15) using a 16-ply laminate with two different ply orientations.

Table 6.3 - Laminate designs used to generate different frictional forces, where slip interfaces are indicated by lines between rows. Ply #1 is closest to the tool surface. Orientations are shown in degrees from the principal axis of the C-spar geometry.

Ply #/SI	1	2	3	7	15
1	±45	±45	±45	±45	±45
2	±45	±45	±45	±45	0/90
3	±45	±45	±45	0/90	±45
4	±45	±45	±45	0/90	0/90
5	±45	0/90	0/90	±45	±45
6	±45	0/90	0/90	±45	0/90
7	±45	0/90	0/90	0/90	±45
8	±45	0/90	0/90	0/90	0/90
9	0/90	0/90	±45	±45	±45
10	0/90	0/90	±45	±45	0/90
11	0/90	0/90	±45	0/90	±45
12	0/90	0/90	±45	0/90	0/90
13	0/90	±45	0/90	±45	±45
14	0/90	±45	0/90	±45	0/90
15	0/90	±45	0/90	0/90	±45
16	0/90	±45	0/90	0/90	0/90

The results of the DDF case study are presented in Figure 6.17, comparing the wrinkle patterns that are generated on the upper face of the C-spar from both the experiments and the numerical model. As the number of SI increases, the severity of the wrinkling increases for both data sets. This trend can be attributed to the increase in frictional forces in the stack – as the number of opposing deformation modes at interfaces of dissimilar ply orientations increases, the resistance to deformation increases, forcing the fabric out-of-plane.
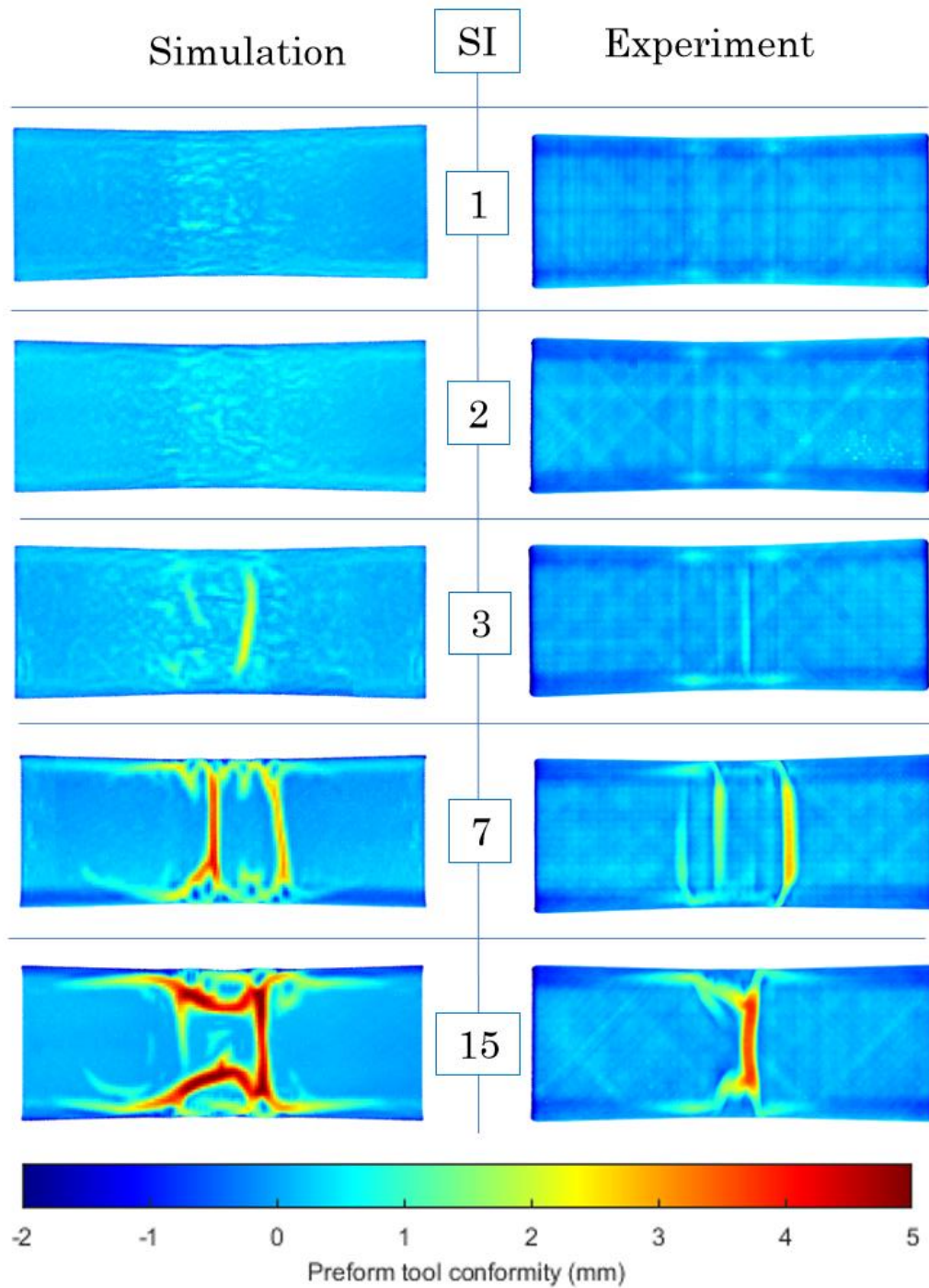
Figure 6.17 - Comparison of experimental and simulation wrinkle patterns for 16-ply preforms with an increasing number of slip interfaces (SI).

When stacks of [0°/90°]$_{16}$ and [±45°]$_{16}$ were formed experimentally and via simulation, no wrinkles were observed. The [0°/90°]$_{16}$ laminate

exhibits the highest bending stiffness because there are continuous fibres running the length of the spar for all 16 plies, yet it remains relatively formable. Therefore, it can be concluded that the increased resistance to shear deformation is the principal mechanism causing the wrinkles for the other ply layups, rather than the increase in bending stiffness caused by the frictional bending moment for these multi-ply laminates.

The shear angle distribution in the plies either side of the mid-plane for the simulated 1SI and 15SI cases are shown in Figure 6.18. The level of in-plane shear in both the [0°/90°] and [±45°] is significantly more constrained in the 15SI form compared with the 1SI. Consequently, the fabric is forced to buckle out-of-plane in order to conform to the tool geometry, generating large wrinkles as a result of the increased bending stiffness.
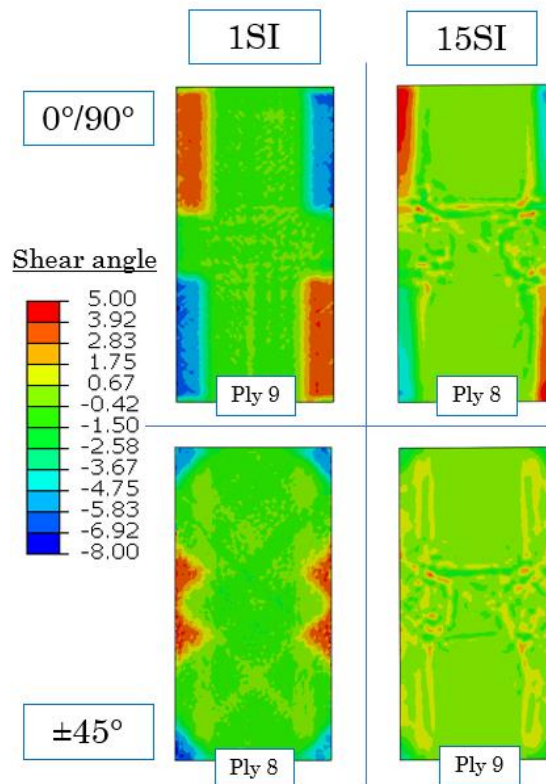
Figure 6.18 - Shear angle distributions in plies about the mid-plane for the 1SI and 15SI simulated forming cases shown on undeformed plies.

The 15SI case ($[\pm45°//0°/90°]_8$) was used to compare the primary transverse wrinkles from the experiment and simulation by taking a section along the principal axis of the spar. The experimental wrinkle was stabilised by forming the laminate with Epikote 05390 Preform Binder, which was allowed to set on the tool before infusing the preform with IN2 epoxy resin under vacuum pressure. Figure 6.19 compares the shape of the experimental and simulated sections. Despite the limited mesh density of the simulation causing relatively low resolution of the wrinkle curvature, the two are in good agreement. In both cases, the wrinkle occurs in every ply, increasing in wavelength through the Z direction.
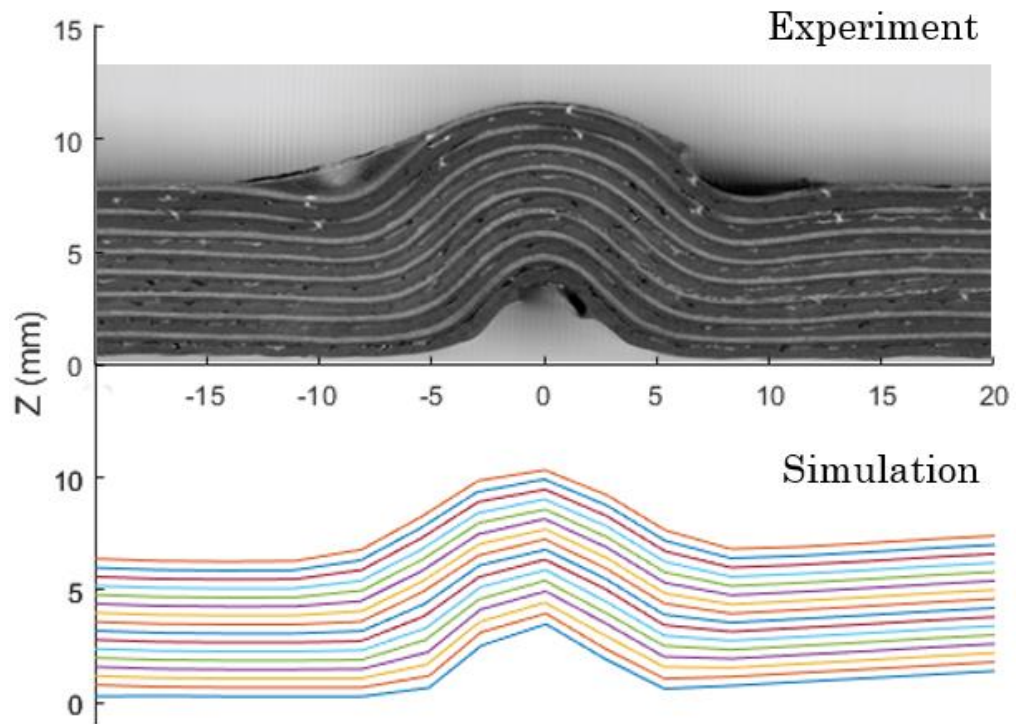
Figure 6.19 - Cross section of the principal transverse wrinkle in the 15SI DDF case for experimental and simulated forms.

The simulation captures the wrinkling trend effectively, and gives a good approximation for the position, wavelength, and amplitude of the wrinkles, considering the levels of experimental variability. A comparison of the maximum wrinkle amplitudes is presented in Figure 6.20, showing reasonable agreement between simulation and experiment. The amplitudes have been normalised for both experimental and simulation data by removing the amplitude of the 1SI case, which was very close to zero. The 1SI and 2SI cases show good formability, producing no significant wrinkling, capturing the tendencies from the equivalent experiments. When wrinkles do begin to form, the simulation over-estimates their severity by between 0.7 and 1.1 mm. The simulation also predicts a number of smaller wrinkles that are not observed at all, in both the 2-ply and 16-ply experimental forms. This under-estimation in formability is caused

by the homogenisation of the biaxial NCF architecture – in the experiment, a small amount of intra-ply slip is possible between fibre bundles, which is not considered by the material model. As a result, energy that is normally able to dissipate via small intra-ply deformation causes the ply to force out of plane, increasing the amplitude of large wrinkles and generating smaller defects that are not observed experimentally. Importantly, however, the trend of decreasing formability with the number of slip interfaces is effectively captured by the simulation, with a strong correlation coefficient between simulation and experimental maximum amplitudes of 0.955.
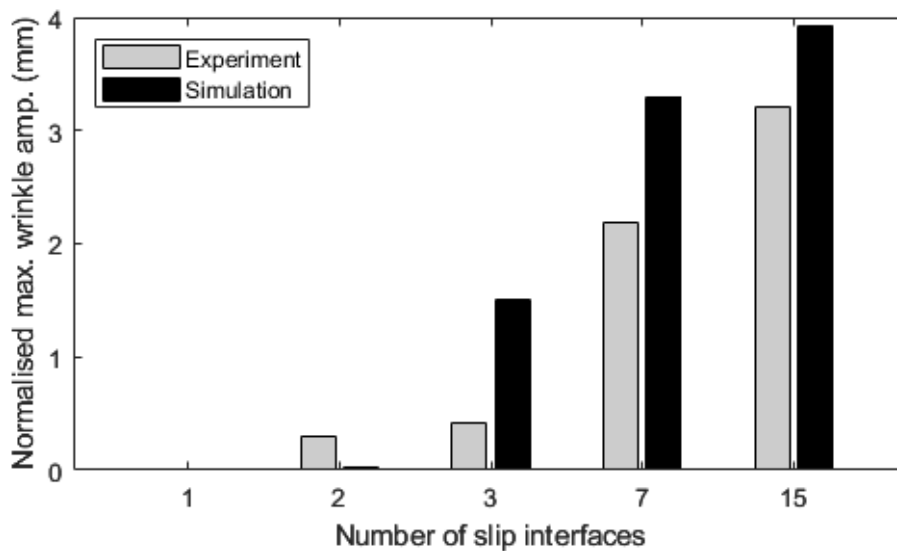
Figure 6.20 - Maximum normalised wrinkle amplitudes for experimental and normal DDF spar preforms, normalised to the 1SI case.

6.6 Chapter summary and conclusions

The mechanisms that contribute to the formation of wrinkling defects during preforming of thick multi-ply NCF laminates have been investigated using novel characterisation tests, numerical simulations and a DDF case study. The non-linear bending stiffness for multi-ply laminates was studied, demonstrating that inter-ply friction produces a significant increase in bending stiffness for thick laminates. This increase was incorporated into an explicit finite element analysis by including the experimental curvature-bending moment relationship for a multi-ply stack, which predicted results that agreed well with experiment.

Multi-ply shear was investigated under varying levels of compaction pressure, representing the conditions experienced during the DDF process. On average, the resulting increase in intra-yarn friction that results from applying vacuum pressure (100 kPa) produced an 18.1% increase in the in-plane shear resistance. In addition, the influence of inter-ply friction on shear resistance was further investigated by inter-leaving additional fabric plies through the laminate stack. It was shown that the shear resistance of the stack increases with the increasing number of slip interfaces between plies of dissimilar orientation.

A multi-ply DDF case study was presented using a C-spar tool geometry, which confirmed that increasing the number of slip interfaces in a 16-ply stack significantly reduced its formability, generating large out-out-plane wrinkling defects. This was attributed to the increase in shear resistance, rather than the increase in bending stiffness, according to the shear distribution from the simulation results. The wrinkle patterns produced by the simulation generally agreed well with the experiments, although the amplitude

of the wrinkles was over-estimated by approximately 1mm for the case with 15 slip interfaces.

7. Conclusions

7.1 Summary of thesis

As the global composites industry transitions away from energy intensive autoclave manufacturing methods, the new challenges presented by automated processes must be addressed. For the case of two-dimensional to three-dimensional fabric preforming, the primary concern is one of defect mitigation, and therefore an understanding of how wrinkles, fabric gapping and other undesirable defects form is required for continued development and industrial uptake.

As initially discussed in Section 1.2 and elaborated further upon in Chapter 2, this thesis aimed to improve understanding of the automated forming composite components constructed of multiple plies of biaxial NCF (as a material with current industrial relevance) through material and process characterisation, analysis, and prediction of the mechanisms that cause these defects to arise. Inter-ply friction and through thickness compaction (and their subsequent effect on out-of-plane bending and in-plane shear) were identified as mechanisms that are poorly understood in the existing literature and are of particular relevance when forming thicker, multi-ply structures.

The novelties from each chapter of this thesis are summarised in Table 7.1.

Table 7.1 - Summary of thesis novelties

Chapter	Summary of novelty points
3	• Development of a new test to characterise frictional behaviour under conditions representative of a forming process • Quantification of anisotropic, pressure dependent frictional behaviour of a biaxial NCF
4	• Demonstration of the anisotropic nesting behaviour of a biaxial NCF, and improved understanding of its relationship with anisotropic inter-ply friction
5	• Development of an image-based method of quantifying through-thickness deformation of dry fabrics under load, representative of a forming process • Prediction of pressure dependent frictional response from results of aforementioned deformation characterisation
6	• Accurate prediction of wrinkling defects in "thick" multi-ply preforms through the inclusion of non-Coulomb friction surface modelling • Introduction of a design guideline on biaxial NCF layup sequence through demonstration of varying number of slip interfaces

7.2 Inter-ply sliding behaviour

The following conclusions have been drawn regarding inter-ply friction characterisation and sliding behaviour of biaxial NCFs, predominantly inferred from the results found in Chapters 3 and 5:

i. The overlap friction test can be used to overcome some of the drawbacks of conventional friction characterisation tests, such as low maximum applicable normal loads and stick-slip behaviour.

ii. Inter-ply friction of a biaxial NCF is highly dependent on the compaction pressure – as the applied normal load increases, the static and dynamic coefficients of friction increase exponentially.

iii. Pressure dependency of inter-ply friction can be attributed to deformation of the fabric when subject to normal loading. A change in contact area between plies at the tow and fibre level contributes to an increased resistance to relative motion but does not fully explain the phenomenon.

iv. Inter-ply friction of a biaxial NCF is dependent on the relative fibre orientations of each ply – ply-ply interactions with parallel fibre interactions generate static and dynamic coefficients of friction of greater magnitude than interactions at any other relative fibre angle.

v. The significance of anisotropic friction on component formability is minor, as the amount of inter-ply slip between plies of similar orientation is negligible. However, additional fabric gapping defects may be generated in some cases as a result of high localised frictional forces.

7.3 Through-thickness compaction behaviour

The following conclusions regarding through-thickness compaction behaviour of biaxial NCFs have been made, informed by results from chapters 4 and 5:

i. Similar to the inter-ply frictional behaviour observed with the overlap test, the compaction response of a biaxial NCF is dependent on inter-ply fibre orientation. Fabric stacks with non-parallel fibre orientations exhibit higher compaction

stiffnesses than those with parallel fibres, as tows are not able to commingle and nest within contacting plies without additional deformation.

ii.   Introduction of additional inter-lamina material, such as a polymer veil, can inhibit nesting between plies, preventing the orientation dependency of the compaction response. Subsequently, the anisotropic inter-ply friction behaviour is also eliminated, confirming the nesting behaviour as its cause.

iii. Real contact area between plies at the mesoscale (tow level) is significantly less than the apparent contact area at the macroscale (ply level) and increases as a function of applied normal load. It can also be used to estimate more accurate frictional forces generated at a given interface under known conditions.

7.4 Multi-ply formability

Finally, from Chapter 6, the following conclusions have been reached concerning the formability of multi-ply laminates, considering the influence of friction and compaction behaviours on the in-plane shear and out-of-plane bending behaviours:

i.   Inter-ply friction can significantly increase the bending stiffness of a multi-ply stack of biaxial NCF material via a frictional bending moment.

ii. Inter-ply friction between plies of dissimilar fibre orientation can increase resistance to in-plane shear deformation. Subsequently, laminate stacks with greater number of ply-ply interfaces with dissimilar fibre orientations (SIs) exhibit much higher shear resistance than those with fewer SIs.

iii. The number of SIs within a laminate stack has a serious impact on the formability of a preform – laminates with a greater number of SIs were shown to generate more severe out-of-plane wrinkling in both experimental and numerical analyses. It can be concluded that, for the C-spar geometry presented, the increased resistance to shear was the most significant factor in this reduced formability, since laminates with no SIs and higher bending stiffness did not produce wrinkles.

iv. To more accurately simulate the forming of thick structures using FEA, it is necessary to take into account the pressure dependency of the inter-ply friction.

7.5 Recommendations for future work

Some limitations of the work conducted in this thesis and potential improvements to the methodologies have been discussed in each chapter. Additionally, some additional questions have been generated that may be prevalent when considering further research on the topic of forming of multi-ply laminates:

i. Are the same inter-ply friction and through-thickness compaction mechanisms observed for biaxial NCFs applicable to UD materials? The characterisation methods outlined in this thesis can be used to investigate multi-ply deformation mechanisms for other materials, which combined with a UD material model, could enable accurate prediction of defects in UD and UD-biaxial hybrid laminates using FEA.

ii. How does a biaxial NCF fabric deform at the mesoscale when subject to not just compaction load, but sliding between plies? High-rate, in-situ CT analysis, such as that made possible using a synchrotron light source, would be required to

effectively capture images of deformation at a sufficient frequency.

iii. A custom surface interaction model may be of interest to improve the accuracy of the homogenised forming simulation. This model could account for not only the pressure dependency of inter-ply friction, but also static and dynamic coefficients of friction, and the fibre orientation dependency that was deemed out of scope for this thesis. By utilising Abaqus/Explicit VFABRIC, VFRICTION and VEXTERNALDB subroutines, the friction bending moment could also be captured, improving the robustness of the material model.

References

[1]   C. Soutis, Introduction: Engineering requirements for aerospace composite materials, in: Polym. Compos. Aerosp. Ind., Elsevier Ltd, 2014: pp. 1–18. https://doi.org/10.1016/B978-0-85709-523-7.00001-3.

[2]   M. Maria, Advanced composite materials of the future in aerospace industry, Incas Bull. 5 (2013) 139–150. https://doi.org/10.13111/2066-8201.2013.5.3.14.

[3]   Airbus Group, Global Market Forecast, 2023. www.airbus.com.

[4]   JEC, Overview of the global composites market 2022-2027, 2023.

[5]   S.S.P. Reddy, R. Suresh, M.B. Hanamantraygouda, B.P. Shivakumar, Use of composite materials and hybrid composites in wind turbine blades, Mater. Today Proc. 46 (2021) 2827–2830. https://doi.org/10.1016/j.matpr.2021.02.745.

[6]   G. Nehls, China's Sany Renewable rolls out 131-meter wind blade, CompositesWorld (2024). https://www.compositesworld.com/news/chinas-sany-renewable-rolls-out-131-meter-wind-blade-.

[7]   S.S.P. Reddy, R. Suresh, M.B. Hanamantraygouda, B.P. Shivakumar, Use of composite materials and hybrid composites in wind turbine blades, Mater. Today Proc. 46 (2021) 2827–2830. https://doi.org/10.1016/j.matpr.2021.02.745.

[8]   P. Nagrale, Wind Turbine Blade Market Research Report, 1 (2024) 1–7. https://www.marketresearchfuture.com/reports/wind-turbine-blade-market-1150 (accessed April 9, 2024).

[9]   K. Madsen, * EP004234192A1 * Designated METHOD FOR MANUFACTURING WIND TURBINE BLADE PREFORMS WITH COMPLEX GEOMETRIES, 2023.

[10]   P.J. Schubel, Cost modelling in polymer composite applications: Case study - Analysis of existing and automated manufacturing processes for a large wind turbine blade, Compos. Part B Eng. 43 (2012) 953–960.

https://doi.org/10.1016/j.compositesb.2011.11.036.

[11] N. Arnold, Carbon fiber: Using the hi-tech material in car-marking, BMW (2020). https://www.bmw.com/en/performance/carbon-fiber-in-a-car.html (accessed March 4, 2024).

[12] L. Luong, Lighter, Faster, Further: Jaguar Land Rover's Groundbreaking Advanced Composites Project, Jaguar L. Rover (2021). https://media.jaguarlandrover.com/news/2021/01/lighter-faster-further-jaguar-land-rovers-groundbreaking-advanced-composites-project (accessed March 4, 2024).

[13] Toyota Industries Corporation Wins JEC Composites Innovation Awards for CFRP Recycling Technology and Recycling System, Toyota Ind. Corp. (2023). https://www.toyota-industries.com/news/2023/03/09/005485/index.html (accessed March 4, 2024).

[14] A. Wazeer, A. Das, C. Abeykoon, A. Sinha, A. Karmakar, Composites for electric vehicles and automotive sector: A review, Green Energy Intell. Transp. 2 (2023). https://doi.org/10.1016/j.geits.2022.100043.

[15] ProDrive, Sustainable Composites, (n.d.). https://www.prodrive.com/sustainable-composites (accessed April 10, 2024).

[16] ProDrive, PRODRIVE SOLVES COMPOSITES RECYCLING CHALLENGE, (2018). https://www.prodrive.com/post/prodrive-composites-recycling (accessed April 10, 2024).

[17] C.H. Choi, S.S. Park, T.W. Hwang, Development of composite body panels for a lightweight vehicle, SAE Tech. Pap. 110 (2001) 143–149. https://doi.org/10.4271/2001-01-0102.

[18] L. Thomson, McLaren reveals new carbon chassis designed for hybrids, Goodwood Road Racing (2020). https://www.goodwood.com/grr/road/news/mclaren-reveals-new-carbon-chassis-designed-for-hybrids/ (accessed April 10, 2024).

[19] P. Malnati, Automotive chassis components lighten up with composites, Compos. World (2023). https://www.compositesworld.com/articles/automotive-chassis-components-lighten-up-with-composites (accessed April 10, 2024).

[20]   L. Dong, Z. Zhang, Y. Jiang, F. Yu, Drop damage analysis of automotive high-pressure composite hydrogen storage cylinders, J. Energy Storage 86 (2024) 111181. https://doi.org/10.1016/j.est.2024.111181.

[21]   Market Insights - Electric Vehicles, Statista (2024). https://www.statista.com/outlook/mmo/electric-vehicles/united-kingdom (accessed March 4, 2024).

[22]   Providing a solid base for high-volume RTM production, Compos. Integr. (2018). https://composite-integration.co.uk/providing-a-solid-base-for-high-volume-rtm-production/ (accessed March 4, 2024).

[23]   M.S. Sarfraz, H. Hong, S.S. Kim, Recent developments in the manufacturing technologies of composite components and their cost-effectiveness in the automotive industry: A review study, Compos. Struct. 266 (2021) 113864. https://doi.org/10.1016/j.compstruct.2021.113864.

[24]   C. V. Katsiropoulos, A. Loukopoulos, S.G. Pantelakis, Comparative environmental and cost analysis of alternative production scenarios associated with a helicopter's canopy, Aerospace 6 (2019). https://doi.org/10.3390/aerospace6010003.

[25]   Processes: Methods of Composite Manufacture, Compos. UK (n.d.). https://compositesuk.co.uk/composite-materials/processes/ (accessed April 9, 2024).

[26]   M. Baskaran, I. Ortiz De Mendibil, M. Sarrionandia, J. Aurrekoetxea, J. Acosta, U. Argarate, D. Chico, Manufacturing cost comparison of RTM, HP-RTM and CRTM for an automotive roof, 16th Eur. Conf. Compos. Mater. ECCM 2014 (2014).

[27]   N. Xie, R.A. Smith, S. Mukhopadhyay, S.R. Hallett, A numerical study on the influence of composite wrinkle defect geometry on compressive strength, Mater. Des. 140 (2018) 7–20. https://doi.org/10.1016/j.matdes.2017.11.034.

[28]   K. Tanaka, R. Ushiyama, T. Katayama, S. Enoki, H. Sakamoto, Formability evaluation of carbon fiber NCF by a non-contact 3D strain measurement system and the effects of blank folder force on its formability, WIT Trans. Built Environ. 137 (2014) 317–326. https://doi.org/10.2495/HPSM140301.

[29]   B. Sköck-Hartmann, T. Gries, Automotive applications of non-crimp fabric composites, Woodhead Publishing Limited, 2011.

https://doi.org/10.1533/9780857092533.4.461.

[30] L. Wood, Global Composites Market Report 2019: $40.2 Billion Market Trends, Forecast and Competitive Analysis 2013-2018 & 2019-2024, GlobeNewswire News Room (2019) 1–7. https://www.globenewswire.com/fr/news-release/2019/04/12/1803326/0/en/Global-Composites-Market-Report-2019-40-2-Billion-Market-Trends-Forecast-and-Competitive-Analysis-2013-2018-2019-2024.html.

[31] L. Harper, M.J. Clifford, Where is the industry heading?, in: L. Harper, M.J. Clifford (Eds.), Des. Manuf. Compos. Mater., 1st ed., Woodhead Publishing Ltd, Oxford, UK, 2023: pp. 9–17.

[32] T. Groetsch, C. Creighton, R. Varley, A. Kaluza, A. Dér, F. Cerdas, C. Herrmann, A modular LCA/LCC-modelling concept for evaluating material and process innovations in carbon fibre manufacturing, Procedia CIRP 98 (2021) 529–534. https://doi.org/10.1016/j.procir.2021.01.146.

[33] The ICE Database, Circ. Ecol. (2019). https://circularecology.com/embodied-carbon-footprint-database.html (accessed June 19, 2024).

[34] A. Endruweit, Liquid Composite Moulding, in: L. Harper, M. Clifford (Eds.), Des. Manuf. Struct. Compos., 1st ed., Elsevier Ltd., 2023: pp. 237–238.

[35] F. Dumont, C. Weimer, D. Soulat, J. Launay, S. Chatel, S. Maison-Le-Poec, Composites preforms simulations for helicopters parts, Int. J. Mater. Form. 1 (2008) 847–850. https://doi.org/10.1007/s12289-008-0268-9.

[36] G. Gardiner, HP-RTM for serial production of cost-effective CFRP aerostructures, Compos. World (2019). https://www.compositesworld.com/articles/hp-rtm-for-serial-production-of-cost-effective-cfrp-aerostructures (accessed January 3, 2023).

[37] G. Gardiner, Reducing manufacturing cost via RTM, Compos. World (2015). https://www.compositesworld.com/articles/reducing-manufacturing-cost-via-rtm (accessed January 3, 2023).

[38] P. Harrison, R. Gomes, N. Curado-Correia, Press forming a 0/90 cross-ply advanced thermoplastic composite using the double-dome benchmark geometry, Compos. Part A Appl. Sci. Manuf. 54 (2013) 56–69. https://doi.org/10.1016/j.compositesa.2013.06.014.

[39] H. Alshahrani, M. Hojjati, Experimental and numerical investigations on formability of out-of-autoclave thermoset prepreg using a double diaphragm process, Compos. Part A Appl. Sci. Manuf. 101 (2017) 199–214. https://doi.org/10.1016/j.compositesa.2017.06.021.

[40] S. Chen, Fabric Forming Simulation and Process Optimisation for Composites, 2016.

[41] M. Hou, Stamp forming of continuous glass fibre reinforced polypropylene, Compos. Part A Appl. Sci. Manuf. 28 (1997) 695–702. https://doi.org/10.1016/S1359-835X(97)00013-4.

[42] J. Krebs, K. Friedrich, D. Bhattacharyya, A direct comparison of matched-die versus diaphragm forming, Compos. Part A Appl. Sci. Manuf. 29 (1998) 183–188. https://doi.org/10.1016/S1359-835X(97)82706-6.

[43] S. Chen, L.T. Harper, Two-dimensional to three-dimensional dry fibre preforming, in: L.T. Harper, M. Clifford (Eds.), Des. Manuf. Struct. Compos., 1st ed., Elsevier Ltd., 2023: p. 106.

[44] S. Chen, O.P.L. McGregor, A. Endruweit, M.T. Elsmore, D.S.A. De Focatiis, L.T. Harper, N.A. Warrior, Double diaphragm forming simulation for complex composite structures, Compos. Part A Appl. Sci. Manuf. 95 (2017) 346–358. https://doi.org/10.1016/j.compositesa.2017.01.017.

[45] F. Yu, S. Chen, L.T. Harper, N.A. Warrior, Investigation into the effects of inter-ply sliding during double diaphragm forming for multi-layered biaxial non-crimp fabrics, Compos. Part A Appl. Sci. Manuf. 150 (2021). https://doi.org/10.1016/j.compositesa.2021.106611.

[46] W.-T. Wang, H. Yu, K. Potter, B.. C.. Kim, Improvement of Composite Drape Forming Quality by Enhancing Interply Slip . In ECCM17 - 17th European Conference on Composite Materials : Munich , German , 26-30 June 2016 . European Conferen, (2016) 26–30.

[47] B. Griffiths, Composite wing spars carry the enormous turboprop engines, (2010) 1–4. https://www.compositesworld.com/articles/composite-wing-spars-carry-the-western-worlds-biggest-turboprop-engines (accessed April 13, 2023).

[48] O.P.L. McGregor, S. Chen, L.T. Harper, A. Endruweit, N.A. Warrior, Defect reduction in the double diaphragm forming process, ICCM Int. Conf.

Compos. Mater. 2017-Augus (2017) 20–25.

[49] K. Potter, Intermediate composite materials, in: L.T. Harper, M.J. Clifford (Eds.), Des. Manuf. Compos. Mater., 1st ed., Elsevier Ltd., Cambridge, 2023: p. 85.

[50] A.C. Long, Introduction, in: A.C. Long (Ed.), Des. Manuf. Text. Compos., Elsevier, Cambridge, UK, 2005: pp. xiii–xvi.

[51] J.P. Snudden, C. Ward, K. Potter, Reusing automotive composites production waste, Reinf. Plast. 58 (2014) 20–27. https://doi.org/10.1016/S0034-3617(14)70246-2.

[52] J. Galos, Thin-ply composite laminates: a review, Compos. Struct. 236 (2020). https://doi.org/10.1016/j.compstruct.2020.111920.

[53] L. Brown, TexGen, (2024). https://texgen.sourceforge.io/index.php/Main_Page (accessed January 30, 2024).

[54] C. Jimenez Martin, V.K. Maes, T. McMahon, J. Kratz, The Role of Bias Extension Testing to Guide Forming of Non-Crimp Fabrics, Front. Mater. 9 (2022) 1–13. https://doi.org/10.3389/fmats.2022.825830.

[55] U. Ahmed, A. Tariq, Y. Nawab, K. Shaker, Z. Khaliq, M. Umair, Comparison of Mechanical Behavior of Biaxial, Unidirectional and Standard Woven Fabric Reinforced Composites, Fibers Polym. 21 (2020) 1308–1315. https://doi.org/10.1007/s12221-020-9915-7.

[56] G.A. Bibo, P.J. Hogg, M. Kemp, Mechanical characterisation of glass- and carbon-fibre-reinforced composites made with non-crimp fabrics, Compos. Sci. Technol. 57 (1997) 1221–1241. https://doi.org/10.1016/s0266-3538(97)00053-5.

[57] K. Vallons, G. Adolphs, P. Lucas, S. V. Lomov, I. Verpoest, Quasi-UD glass fibre NCF composites for wind energy applications: A review of requirements and existing fatigue data for blade materials, Mech. Ind. 14 (2013) 175–189. https://doi.org/10.1051/meca/2013045.

[58] J. Sloan, Large, high-volume, infused composite structures on the aerospace horizon, Compos. World (2019). https://www.compositesworld.com/articles/large-high-volume-infused-

composite-structures-on-the-aerospace-horizon (accessed June 20, 2024).

[59]   P. Böhler, F. Härtel, P. Middendorf, Identification of forming limits for unidirectional carbon textiles in reality and mesoscopic simulation, Key Eng. Mater. 554–557 (2013) 423–432. https://doi.org/10.4028/www.scientific.net/KEM.554-557.423.

[60]   L. Kärger, A. Bernath, F. Fritz, S. Galkin, D. Magagnato, A. Oeckerath, A. Schön, F. Henning, Development and validation of a CAE chain for unidirectional fibre reinforced composite components, Compos. Struct. 132 (2015) 350–358. https://doi.org/10.1016/j.compstruct.2015.05.047.

[61]   F.J. Schirmaier, K.A. Weidenmann, L. Kärger, F. Henning, Characterisation of the draping behaviour of unidirectional non-crimp fabrics (UD-NCF), Compos. Part A Appl. Sci. Manuf. 80 (2016) 28–38. https://doi.org/10.1016/j.compositesa.2015.10.004.

[62]   S. Chen, O.P.L. McGregor, L.T. Harper, A. Endruweit, N.A. Warrior, Defect formation during preforming of a bi-axial non-crimp fabric with a pillar stitch pattern, Compos. Part A Appl. Sci. Manuf. 91 (2016) 156–167. https://doi.org/10.1016/j.compositesa.2016.09.016.

[63]   A. Habboush, N. Sanbhal, H. Shao, J. Jiang, N. Chen, Characterization and analysis of in-plane shear behavior of glass warp-knitted non-crimp fabrics based on picture frame method, Materials (Basel). 11 (2018). https://doi.org/10.3390/ma11091550.

[64]   H. Kong, A.P. Mouritz, R. Paton, Tensile extension properties and deformation mechanisms of multiaxial non-crimp fabrics, Compos. Struct. 66 (2004) 249–259. https://doi.org/10.1016/j.compstruct.2004.04.046.

[65]   S.E. Arnold, M.P.F. Sutcliffe, W.L.A. Oram, Experimental measurement of wrinkle formation during draping of non-crimp fabric, Compos. Part A Appl. Sci. Manuf. 82 (2016) 159–169. https://doi.org/10.1016/j.compositesa.2015.12.011.

[66]   A.. Long, M.J. Clifford, Composite forming mechanisms and materials characterisation, in: A.. Long (Ed.), Compos. Form. Technol., 1st ed., Woodhead Publishing Ltd, 2007: pp. 1–21.

[67]   S. Chen, L.T. Harper, In-plane shear, in: L.T. Harper, M.J. Clifford (Eds.), Des. Manuf. Struct. Compos., 1st ed., Elsevier Ltd., 2023: p. 104.

[68]   P. Boisse, B. Zouari, A. Gasser, A mesoscopic approach for the simulation of woven fibre composite forming, Compos. Sci. Technol. 65 (2005) 429–436. https://doi.org/10.1016/j.compscitech.2004.09.024.

[69]   M. Mei, Y. He, X. Yang, K. Wei, Z. Qu, D. Fang, Shear deformation characteristics and defect evolution of the biaxial ±45° and 0/90° glass non-crimp fabrics, Compos. Sci. Technol. 193 (2020) 108137. https://doi.org/10.1016/j.compscitech.2020.108137.

[70]   G. Creech, A.K. Pickett, Meso-modelling of Non-crimp Fabric composites for coupled drape and failure analysis, J. Mater. Sci. 41 (2006) 6725–6736. https://doi.org/10.1007/s10853-006-0213-6.

[71]   F. Yu, S. Chen, J. V. Viisainen, M.P.F. Sutcliffe, L.T. Harper, N.A. Warrior, A macroscale finite element approach for simulating the bending behaviour of biaxial fabrics, Compos. Sci. Technol. 191 (2020). https://doi.org/10.1016/j.compscitech.2020.108078.

[72]   E. de Bilbao, D. Soulat, G. Hivet, A. Gasser, Experimental Study of Bending Behaviour of Reinforcements, Exp. Mech. 50 (2010) 333–351. https://doi.org/10.1007/s11340-009-9234-9.

[73]   B. Liang, P. Chaudet, P. Boisse, Curvature determination in the bending test of continuous fibre reinforcements, Strain 53 (2017) 1–12. https://doi.org/10.1111/str.12213.

[74]   F. Yu, S. Chen, L.T. Harper, N.A. Warrior, Simulating the effect of fabric bending stiffness on the wrinkling behaviour of biaxial fabrics during preforming, Compos. Part A Appl. Sci. Manuf. 143 (2021). https://doi.org/10.1016/j.compositesa.2021.106308.

[75]   P.H. Broberg, E. Lindgaard, C. Krogh, S.M. Jensen, G.G. Trabal, A.F.M. Thai, B.L.V. Bak, One-click bending stiffness: Robust and reliable automatic calculation of moment–curvature relation in a cantilever bending test, Compos. Part B Eng. 260 (2023) 110763. https://doi.org/10.1016/j.compositesb.2023.110763.

[76]   B. Liang, J. Colmars, P. Boisse, A shell formulation for fibrous reinforcement forming simulations, Compos. Part A Appl. Sci. Manuf. 100 (2017) 81–96. https://doi.org/10.1016/j.compositesa.2017.04.024.

[77]   T. Senner, S. Kreissl, M. Merklein, M. Meinhardt, A. Lipp, Bending of

unidirectional non-crimp-fabrics: experimental characterization, constitutive modeling and application in finite element simulation, Prod. Eng. 9 (2015) 1–10. https://doi.org/10.1007/s11740-014-0568-5.

[78]   U. Sachs, R. Akkerman, K. Fetfatsidis, E. Vidal-Sallé, J. Schumacher, G. Ziegmann, S. Allaoui, G. Hivet, B. Maron, K. Vanclooster, S. V. Lomov, Characterization of the dynamic friction of woven fabrics: Experimental methods and benchmark results, Compos. Part A Appl. Sci. Manuf. 67 (2014) 289–298. https://doi.org/10.1016/j.compositesa.2014.08.026.

[79]   D.M. Mulvihill, O. Smerdova, M.P.F. Sutcliffe, Friction of carbon fibre tows, Compos. Part A Appl. Sci. Manuf. 93 (2017) 185–198. https://doi.org/10.1016/j.compositesa.2016.08.034.

[80]   bo Cornelissen, M.B. de Rooij, B. Rietman, R. Akkerman, Frictional behavior of carbon fiber tows: A contact mechanics model of tow–tow friction, Text. Res. J. 84 (2014) 1476–1488. https://doi.org/10.1177/0040517514525876.

[81]   I. Hutchings, P. Shipway, Friction and Wear of Engineering Materials, 2017. https://doi.org/10.1016/B978-0-08-100910-9.00003-9.

[82]   J.C. Mergel, R. Sahli, J. Scheibert, R.A. Sauer, Continuum contact models for coupled adhesion and friction, J. Adhes. 95 (2019) 1101–1133. https://doi.org/10.1080/00218464.2018.1479258.

[83]   B.N.J. Persson, I.M. Sivebaek, V.N. Samoilov, K. Zhao, A.I. Volokitin, Z. Zhang, On the origin of Amonton's friction law, (2008). https://doi.org/10.1088/0953-8984/20/39/395006.

[84]   E.I. Avgoulas, D.M. Mulvihill, A. Endruweit, M.P.F. Sutcliffe, N.A. Warrior, D.S.A. De Focatiis, A.C. Long, Frictional behaviour of non-crimp fabrics (NCFs) in contact with a forming tool, Tribol. Int. 121 (2018) 71–77. https://doi.org/10.1016/j.triboint.2018.01.026.

[85]   D.M. Mulvihill, M.P.F. Sutcliffe, Effect of tool surface topography on friction with carbon fibre tows for composite fabric forming, Compos. Part A Appl. Sci. Manuf. 93 (2017) 199–206. https://doi.org/10.1016/j.compositesa.2016.10.017.

[86]   M. Kruse, H.O. Werner, H. Chen, T. Mennecart, W. V. Liebig, K.A. Weidenmann, N. Ben Khalifa, Investigation of the friction behavior between

dry/infiltrated glass fiber fabric and metal sheet during deep drawing of fiber metal laminates, Prod. Eng. 17 (2023) 37–46. https://doi.org/10.1007/s11740-022-01141-y.

[87] Z. Xiang, Y. Liu, X. Zhou, Z. Wu, X. Hu, Interlayer contact mechanism of the frictional behavior of glass-fiber woven fabrics and improvements of winding characteristics, Compos. Struct. 233 (2020) 111497. https://doi.org/10.1016/j.compstruct.2019.111497.

[88] N. Wu, X. Xie, J. Yang, Y. Feng, Y. Jiao, L. Chen, J. Xu, X. Jian, Effect of normal load on the frictional and wear behaviour of carbon fiber in tow-on-tool contact during three-dimensional weaving process, J. Ind. Text. 51 (2022) 2753S-2773S. https://doi.org/10.1177/1528083720944615.

[89] E.I. Avgoulas, D.M. Mulvihill, A. Endruweit, M.P.F. Sutcliffe, N.A. Warrior, D.S.A. De Focatiis, A.C. Long, Frictional behaviour of non-crimp fabrics (NCFs) in contact with a forming tool, Tribol. Int. 121 (2018) 71–77. https://doi.org/10.1016/j.triboint.2018.01.026.

[90] H.. Howell, J. Mazur, AMONTONS' LAW AND FIBRE FRICTION, J. Text. Inst. Trans. 44:2 (1953) T59–T69.

[91] B. Cornelissen, The role of friction in tow mechanics, 2013. http://purl.org/utwente/doi/10.3990/1.9789036534727.

[92] J.L. Gorczyca-Cole, J.A. Sherwood, J. Chen, A friction model for thermostamping commingled glass-polypropylene woven fabrics, Compos. Part A Appl. Sci. Manuf. 38 (2007) 393–406. https://doi.org/10.1016/j.compositesa.2006.03.006.

[93] C.F. Tu, T. Fort, A study of fiber-capstan friction. 1. Stribeck curves, Tribol. Int. 37 (2004) 701–710. https://doi.org/10.1016/j.triboint.2004.02.008.

[94] R.H.W. ten Thije, R. Akkerman, L. van der Meer, M.P. Ubbink, Tool-ply friction in thermoplastic composite forming, Int. J. Mater. Form. 1 (2008) 953–956. https://doi.org/10.1007/s12289-008-0215-9.

[95] R. Akkerman, M.P. Ubbnik, M.B. de Rooij, R.H.W. Ten Thije, Tool - Ply Friction In Composite Forming, 1085 (2011) 1080–1085.

[96] J.M. Lee, B.M. Kim, C.J. Lee, D.C. Ko, A characterisation of tool-ply friction behaviors in thermoplastic composite, Procedia Eng. 207 (2017) 90–94.

https://doi.org/10.1016/j.proeng.2017.10.743.

[97]   A. Rashidi, B. Crawford, T. Olfatbakhsh, A.S. Milani, A mixed lubrication model for inter-ply friction behaviour of uncured fabric prepregs, Compos. Part A Appl. Sci. Manuf. 149 (2021) 106571. https://doi.org/10.1016/j.compositesa.2021.106571.

[98]   A.C. Harrison, P., Thije, R.T., Akkerman, R., and Long, Characterising and Modelling Tool-Ply Friction of Viscous Textile Composites, 7 (2011) 5–22.

[99]   Y.R. Larberg, M. Åkermo, On the interply friction of different generations of carbon/epoxy prepreg systems, Compos. Part A Appl. Sci. Manuf. 42 (2011) 1067–1074. https://doi.org/10.1016/j.compositesa.2011.04.010.

[100] A. Codolini, S. Chen, G.D. Lawrence, L.T. Harper, M.P.F. Sutcliffe, Characterisation of process-induced variability in wrinkle defects during double diaphragm forming of non-crimp fabric, Compos. Part B 281 (2024) 111549. https://doi.org/10.1016/j.compositesb.2024.111549.

[101] P. Boisse, A. Gasser, G. Hivet, Analyses of fabric tensile behaviour: determination of the biaxial tension-strain surfaces and their use in forming simulations, Exp. Mech. 32 (2001) 260–269.

[102] K. Buet-Gautier, P. Boisse, Experimental analysis and modeling of biaxial mechanical behavior of woven composite reinforcements, Exp. Mech. 41 (2001) 260–269. https://doi.org/10.1007/BF02323143.

[103] S.V. Lomov, T. Truong Chi, I. Verpoest, Mechanical properties of non-crimp fabric (NCF) based composites: stiffness and strength, Woodhead Publishing Limited, 2011. https://doi.org/10.1533/9780857092533.3.263.

[104] S. V. Lomov, M. Barburski, T. Stoilova, I. Verpoest, R. Akkerman, R. Loendersloot, R.H.W. Ten Thije, Carbon composites based on multiaxial multiply stitched preforms. Part 3: Biaxial tension, picture frame and compression tests of the preforms, Compos. Part A Appl. Sci. Manuf. 36 (2005) 1188–1206. https://doi.org/10.1016/j.compositesa.2005.01.015.

[105] P. Boisse, M. Borr, K. Buet, A. Cherouat, Finite element simulations of textile composite forming including the biaxial fabric behaviour, Compos. Part B Eng. 28 (1997) 453–464. https://doi.org/10.1016/S1359-8368(96)00067-4.

[106] F. Yu, The Prediction of Wrinkle Formation in Non‑ crimp Fabrics during Double Diaphragm Forming, (2021).

[107] F.J. Schirmaier, D. Dörr, F. Henning, L. Kärger, A macroscopic approach to simulate the forming behaviour of stitched unidirectional non‑crimp fabrics (UD‑NCF), Compos. Part A Appl. Sci. Manuf. 102 (2017) 322–335. https://doi.org/10.1016/j.compositesa.2017.08.009.

[108] F. Nosrat Nezami, T. Gereke, C. Cherif, Analyses of interaction mechanisms during forming of multilayer carbon woven fabrics for composite applications, Compos. Part A Appl. Sci. Manuf. 84 (2016) 406–416. https://doi.org/10.1016/j.compositesa.2016.02.023.

[109] R. Sourki, B. Crawford, R. Vaziri, A.S. Milani, Orientation Dependency and Hysteresis Nature of Inter‑Ply Friction in Woven Fabrics, Appl. Compos. Mater. (2021). https://doi.org/10.1007/s10443‑020‑09846‑y.

[110] N. Ersoy, K. Potter, M.R. Wisnom, M.J. Clegg, An experimental method to study the frictional processes during composites manufacturing, Compos. Part A Appl. Sci. Manuf. 36 (2005) 1536–1544. https://doi.org/10.1016/j.compositesa.2005.02.010.

[111] A.. Long, M.J. Clifford, Ply/tool and ply/ply friction, in: A.. Long, M.J. Clifford (Eds.), Compos. Form. Technol., 1st ed., Woodhead Publishing Limited, Cambridge, UK, 2007: pp. 10–12.

[112] A. Rashidi, H. Montazerian, K. Yesilcimen, A.S. Milani, Experimental characterization of the inter‑ply shear behavior of dry and prepreg woven fabrics: Significance of mixed lubrication mode during thermoset composites processing, Compos. Part A Appl. Sci. Manuf. 129 (2020) 105725. https://doi.org/10.1016/j.compositesa.2019.105725.

[113] A.R. Labanieh, C. Garnier, P. Ouagne, O. Dalverny, D. Soulat, Intra‑ply yarn sliding defect in hemisphere preforming of a woven preform, Compos. Part A Appl. Sci. Manuf. 107 (2018) 432–446. https://doi.org/10.1016/j.compositesa.2018.01.018.

[114] S. Allaoui, C. Cellard, G. Hivet, Effect of inter‑ply sliding on the quality of multilayer interlock dry fabric preforms, Compos. Part A Appl. Sci. Manuf. 68 (2015) 336–345. https://doi.org/10.1016/j.compositesa.2014.10.017.

[115] P. Hallander, M. Akermo, C. Mattei, M. Petersson, T. Nyman, An

experimental study of mechanisms behind wrinkle development during forming of composite laminates, Compos. Part A Appl. Sci. Manuf. 50 (2013) 54–64. https://doi.org/10.1016/j.compositesa.2013.03.013.

[116] C. Scarth, Y. Chen, C. Aza, A.T. Rhead, R. Butler, Manufacture of long spars: Laminate design, experimental trials and non-destructive evaluation, Compos. Part B Eng. 255 (2023) 110646. https://doi.org/10.1016/j.compositesb.2023.110646.

[117] B. Cornelissen, M.B. de Rooij, B. Rietman, R. Akkerman, Frictional behaviour of high performance fibrous tows: A contact mechanics model of tow-metal friction, Wear 305 (2013) 78–88. https://doi.org/10.1016/j.wear.2013.05.014.

[118] M. Tourlonias, M.A. Bueno, G. Fassi, I. Aktas, Y. Wielhorski, Influence of friction angle between carbon single fibres and tows: Experimental analysis and analytical model, Compos. Part A Appl. Sci. Manuf. 124 (2019). https://doi.org/10.1016/j.compositesa.2019.105478.

[119] B. Cornelissen, U. Sachs, B. Rietman, R. Akkerman, Dry friction characterisation of carbon fibre tow and satin weave fabric for composite applications, Compos. Part A Appl. Sci. Manuf. 56 (2014) 127–135. https://doi.org/10.1016/j.compositesa.2013.10.006.

[120] N.D. Chakladar, P. Mandal, P. Potluri, Effects of inter-tow angle and tow size on carbon fibre friction, Compos. Part A Appl. Sci. Manuf. 65 (2014) 115–124. https://doi.org/10.1016/j.compositesa.2014.06.002.

[121] A. Dutta, M.K. Hagnell, M. Åkermo, Interply friction between unidirectional carbon/epoxy prepreg plies: Influence of fibre orientation, Compos. Part A Appl. Sci. Manuf. 166 (2023) 107375. https://doi.org/10.1016/j.compositesa.2022.107375.

[122] Y. Sugimoto, D. Shimamoto, Y. Hotta, Evaluation of kinetic friction coefficients between single carbon fibers, Carbon N. Y. 167 (2020) 264–269. https://doi.org/10.1016/j.carbon.2020.06.010.

[123] F. Robitaille, R. Gauvin, Compaction of textile reinforcements for composites manufacturing. I: Review of experimental results, Polym. Compos. 19 (1998) 198–216. https://doi.org/10.1002/pc.10091.

[124] I. Hutchings, P. Shipway, Contact between surfaces, in: I. Hutchings, P.

Shipway (Eds.), Tribol. Frict. Wear Eng. Mater., 1st ed., Butterworth-Heinemann, Oxford, UK, 2017: pp. 18–22.

[125] E. Liamas, S.D. Connell, S.N. Ramakrishna, Probing the frictional properties of soft materials at the nanoscale, (2020) 2292–2308. https://doi.org/10.1039/c9nr07084b.

[126] J.. Greenwood, J.B.. Williamson, Contact of nominally flat surfaces, Proc. R. Soc. London. Ser. A. Math. Phys. Sci. 295 (1966) 300–319. https://doi.org/10.1098/rspa.1966.0242.

[127] J.S. McFarlange, D. Tabor, Relation between friction and adhesion, Proc. R. Soc. London. Ser. A. Math. Phys. Sci. 202 (1950) 244–253. https://doi.org/10.1098/rspa.1950.0097.

[128] R. Sahli, G. Pallares, C. Ducottet, I.E. Ben Ali, S. Al Akhrass, M. Guibert, J. Scheibert, Evolution of real contact area under shear and the value of static friction of soft materials, 115 (2018) 471–476. https://doi.org/10.1073/pnas.1706434115.

[129] J.H. Dieterich, B.D. Kilgore, Direct observation of frictional contacts: New insights for state-dependent properties, Pure Appl. Geophys. PAGEOPH 143 (1994) 283–302. https://doi.org/10.1007/BF00874332.

[130] O. Ben-david, S.M. Rubinstein, J. Fineberg, Slip-stick and the evolution of frictional strength, Nature 463 (2010). https://doi.org/10.1038/nature08676.

[131] T. Baumberger, C. Caroli, Solid friction from stick-slip down to pinning and aging, Adv. Phys. 55 (2006) 279–348. https://doi.org/10.1080/00018730600732186.

[132] B. Derjaguin, Molekulartheorie der äußeren Reibung, Zeitschrift Für Phys. 88 (1934) 661–675. https://doi.org/10.1007/BF01333114.

[133] J.C. Mergel, J. Scheibert, R.A. Sauer, J.C. Mergel, J. Scheibert, R.A. Sauer, Contact with coupled adhesion and friction : Computational framework , applications , and new insights To cite this version : HAL Id : hal-02890104, (2021).

[134] E. Sacco, F. Lebon, International Journal of Solids and Structures A damage – friction interface model derived from micromechanical approach, Int. J. Solids Struct. 49 (2012) 3666–3680.

https://doi.org/10.1016/j.ijsolstr.2012.07.028.

[135] Z. Yousaf, P. Potluri, P.J. Withers, D. Mollenhauer, E. Zhou, S. Duning, Digital element simulation of aligned tows during compaction validated by computed tomography (CT), Int. J. Solids Struct. 154 (2018) 78–87. https://doi.org/10.1016/j.ijsolstr.2017.05.044.

[136] S. V. Lomov, I. Verpoest, T. Peeters, D. Roose, M. Zako, Nesting in textile laminates: Geometrical modelling of the laminate, Compos. Sci. Technol. 63 (2003) 993–1007. https://doi.org/10.1016/S0266-3538(02)00318-4.

[137] A.J. Thompson, B. El Said, D. Ivanov, J.P.H. Belnoue, S.R. Hallett, High fidelity modelling of the compression behaviour of 2D woven fabrics, Int. J. Solids Struct. 154 (2018) 104–113. https://doi.org/10.1016/j.ijsolstr.2017.06.027.

[138] P. Potluri, T. V. Sagar, Compaction modelling of textile preforms for composite structures, Compos. Struct. 86 (2008) 177–185. https://doi.org/10.1016/j.compstruct.2008.03.019.

[139] Z. Yousaf, P.J. Withers, P. Potluri, Compaction, nesting and image based permeability analysis of multi-layer dry preforms by computed tomography (CT), Compos. Struct. 263 (2021) 113676. https://doi.org/10.1016/j.compstruct.2021.113676.

[140] K. Hoes, D. Dinescu, H. Sol, R.S. Parnas, S. Lomov, Study of nesting induced scatter of permeability values in layered reinforcement fabrics, Compos. Part A Appl. Sci. Manuf. 35 (2004) 1407–1418. https://doi.org/10.1016/j.compositesa.2004.05.004.

[141] F. Robitaille, R. Gauvin, Compaction of textile reinforcements for composites manufacturing. III: Reorganization of the fiber network, Polym. Compos. 20 (1999) 48–61. https://doi.org/10.1002/pc.10334.

[142] F. Robitaille, R. Gauvin, Compaction of textile reinforcements for composites manufacturing. II: Compaction and relaxation of dry and H20-Saturated woven reinforcements, Polym. Compos. 19 (1998) 543–557. https://doi.org/10.1002/pc.10128.

[143] S.H. Lee, J.H. Han, S.Y. Kim, J.R. Youn, Y.S. Song, Compression and relaxation behavior of dry fiber preforms for resin transfer molding, J. Compos. Mater. 44 (2010) 1801–1820.

https://doi.org/10.1177/0021998310369583.

[144] A.A. Somashekar, S. Bickerton, D. Bhattacharyya, Modelling the viscoelastic stress relaxation of glass fibre reinforcements under constant compaction strain during composites manufacturing, Compos. Part A Appl. Sci. Manuf. 43 (2012) 1044–1052. https://doi.org/10.1016/j.compositesa.2012.02.004.

[145] J. Echaabi, M.B. Nziengui, M. Hattabi, Compressibility and relaxation models for fibrous reinforcements in Liquid Composites Moulding, (n.d.). https://doi.org/10.1007/s12289-008-0.

[146] S. Bickerton, M.J. Buntain, A.A. Somashekar, The viscoelastic compression behavior of liquid composite molding preforms, Compos. Part A Appl. Sci. Manuf. 34 (2003) 431–444. https://doi.org/10.1016/S1359-835X(03)00088-5.

[147] D. Bublitz, D. Colin, K. Drechsler, Implementation of a viscoelastic material model to predict the compaction response of dry carbon fiber preforms, Compos. Part A Appl. Sci. Manuf. 153 (2022) 106718. https://doi.org/10.1016/j.compositesa.2021.106718.

[148] M. Danzi, C. Schneeberger, P. Ermanni, A model for the time-dependent compaction response of woven fiber textiles, Compos. Part A Appl. Sci. Manuf. 105 (2018) 180–188. https://doi.org/10.1016/j.compositesa.2017.11.002.

[149] Z. Yousaf, P. Potluri, P.J. Withers, Influence of Tow Architecture on Compaction and Nesting in Textile Preforms, Appl. Compos. Mater. 24 (2017) 337–350. https://doi.org/10.1007/s10443-016-9554-8.

[150] T. Grieser, P. Mitschang, Investigation of the compaction behavior of carbon fiber NCF for continuous preforming processes, Polym. Compos. 38 (2017) 2609–2625. https://doi.org/10.1002/pc.23854.

[151] T. Grieser, P. Mitschang, Influence of compaction behavior of carbon NCF on preform mechanics for continuous profile preforming, ICCM Int. Conf. Compos. Mater. 2015-July (2015) 19–24.

[152] S. Mukhopadhyay, M.I. Jones, S.R. Hallett, Tensile failure of laminates containing an embedded wrinkle; numerical and experimental study, Compos. Part A Appl. Sci. Manuf. 77 (2015) 219–228. https://doi.org/10.1016/j.compositesa.2015.07.007.

[153]   S. Mukhopadhyay, M.I. Jones, S.R. Hallett, Compressive failure of laminates containing an embedded wrinkle; Experimental and numerical study, Compos. Part A Appl. Sci. Manuf. 73 (2015) 132–142. https://doi.org/10.1016/j.compositesa.2015.03.012.

[154]   P. Boisse, N. Hamila, A. Madeo, Modelling the development of defects during composite reinforcements and prepreg forming, Philos. Trans. R. Soc. A Math. Phys. Eng. Sci. 374 (2016). https://doi.org/10.1098/rsta.2015.0269.

[155]   P. Boisse, N. Hamila, E. Vidal-Sallé, F. Dumont, Simulation of wrinkling during textile composite reinforcement forming. Influence of tensile, in-plane shear and bending stiffnesses, Compos. Sci. Technol. 71 (2011) 683–692. https://doi.org/10.1016/j.compscitech.2011.01.011.

[156]   J. Sjölander, P. Hallander, M. Åkermo, Forming induced wrinkling of composite laminates: A numerical study on wrinkling mechanisms, Compos. Part A Appl. Sci. Manuf. 81 (2016) 41–51. https://doi.org/10.1016/j.compositesa.2015.10.012.

[157]   J.S. Lightfoot, M.R. Wisnom, K. Potter, A new mechanism for the formation of ply wrinkles due to shear between plies, Compos. Part A Appl. Sci. Manuf. 49 (2013) 139–147. https://doi.org/10.1016/j.compositesa.2013.03.002.

[158]   A.J. Thompson, J.P.H. Belnoue, S.R. Hallett, Modelling defect formation in textiles during the double diaphragm forming process, Compos. Part B Eng. 202 (2020) 108357. https://doi.org/10.1016/j.compositesb.2020.108357.

[159]   B. Liang, N. Hamila, M. Peillon, P. Boisse, Analysis of thermoplastic prepreg bending stiffness during manufacturing and of its influence on wrinkling simulations, Compos. Part A Appl. Sci. Manuf. 67 (2014) 111–122. https://doi.org/10.1016/j.compositesa.2014.08.020.

[160]   J. V. Viisainen, A. Hosseini, M.P.F. Sutcliffe, Experimental investigation, using 3D digital image correlation, into the effect of component geometry on the wrinkling behaviour and the wrinkling mechanisms of a biaxial NCF during preforming, Compos. Part A Appl. Sci. Manuf. 142 (2021) 106248. https://doi.org/10.1016/j.compositesa.2020.106248.

[161]   A. Levy, P. Hubert, Vacuum-bagged composite laminate forming processes: Predicting thickness deviation in complex shapes, Compos. Part A Appl. Sci. Manuf. 126 (2019) 105568.

https://doi.org/10.1016/j.compositesa.2019.105568.

[162] S. Chen, O.P.L. McGregor, L.T. Harper, A. Endruweit, N.A. Warrior, Optimisation of local in-plane constraining forces in double diaphragm forming, Compos. Struct. 201 (2018) 570–581. https://doi.org/10.1016/j.compstruct.2018.06.062.

[163] J.S. Lee, S.J. Hong, W.R. Yu, T.J. Kang, The effect of blank holder force on the stamp forming behavior of non-crimp fabric with a chain stitch, Compos. Sci. Technol. 67 (2007) 357–366. https://doi.org/10.1016/j.compscitech.2006.09.009.

[164] X. Li, S. Shonkwiler, S. McMains, Detection of resin-rich areas for statistical analysis of fiber-reinforced polymer composites, Compos. Part B Eng. 225 (2021) 109252. https://doi.org/10.1016/j.compositesb.2021.109252.

[165] M.A. Turk, B. Vermes, A.J. Thompson, J.P.H. Belnoue, S.R. Hallett, D.S. Ivanov, Mitigating forming defects by local modification of dry preforms, Compos. Part A Appl. Sci. Manuf. 128 (2020) 105643. https://doi.org/10.1016/j.compositesa.2019.105643.

[166] L. Li, Y. Zhao, H. gia nam Vuong, Y. Chen, J. Yang, Y. Duan, In-plane shear investigation of biaxial carbon non-crimp fabrics with experimental tests and finite element modeling, Mater. Des. 63 (2014) 757–765. https://doi.org/10.1016/j.matdes.2014.07.007.

[167] J. Cao, R. Akkerman, P. Boisse, J. Chen, H.S. Cheng, E.F. de Graaf, J.L. Gorczyca, P. Harrison, G. Hivet, J. Launay, W. Lee, L. Liu, S. V. Lomov, A. Long, E. de Luycker, F. Morestin, J. Padvoiskis, X.Q. Peng, J. Sherwood, T. Stoilova, X.M. Tao, I. Verpoest, A. Willems, J. Wiggers, T.X. Yu, B. Zhu, Characterization of mechanical behavior of woven fabrics: Experimental methods and benchmark results, Compos. Part A Appl. Sci. Manuf. 39 (2008) 1037–1053. https://doi.org/10.1016/j.compositesa.2008.02.016.

[168] G. Lebrun, M.N. Bureau, J. Denault, Evaluation of bias-extension and picture-frame test methods for the measurement of intraply shear properties of PP/glass commingled fabrics, Compos. Struct. 61 (2003) 341–352. https://doi.org/10.1016/S0263-8223(03)00057-6.

[169] S. V. Lomov, P. Boisse, E. Deluycker, F. Morestin, K. Vanclooster, D. Vandepitte, I. Verpoest, A. Willems, Full-field strain measurements in

textile deformability studies, Compos. Part A Appl. Sci. Manuf. 39 (2008) 1232–1244. https://doi.org/10.1016/j.compositesa.2007.09.014.

[170] P. Boisse, N. Hamila, E. Guzman-Maldonado, A. Madeo, G. Hivet, F. dell'Isola, The bias-extension test for the analysis of in-plane shear properties of textile composite reinforcements and prepregs: a review, Int. J. Mater. Form. 10 (2017) 473–492. https://doi.org/10.1007/s12289-016-1294-7.

[171] A. Rashidi, H. Montazerian, A.S. Milani, Slip-bias extension test: A characterization tool for understanding and modeling the effect of clamping conditions in forming of woven fabrics, Compos. Struct. 260 (2021) 113529. https://doi.org/10.1016/j.compstruct.2020.113529.

[172] A. Willems, S. V. Lomov, I. Verpoest, D. Vandepitte, Picture frame shear tests on woven textile composite reinforcements with controlled pretension, AIP Conf. Proc. 907 (2007) 999–1004. https://doi.org/10.1063/1.2729644.

[173] S. Chen, Fabric Forming Simulation and Process Optimisation for Composites, Univ. Nottingham (2016).

[174] P. Harrison, M.J. Clifford, A.C. Long, Shear characterisation of viscous woven textile composites: A comparison between picture frame and bias extension experiments, Compos. Sci. Technol. 64 (2004) 1453–1465. https://doi.org/10.1016/j.compscitech.2003.10.015.

[175] S. Liu, J. Sinke, C. Dransfeld, A modified bias-extension test method for the characterisation of intra-ply shear deformability of hybrid metal-composite laminates, Compos. Struct. 314 (2023). https://doi.org/10.1016/j.compstruct.2023.116964.

[176] I. Taha, Y. Abdin, S. Ebeid, Comparison of picture frame and Bias-Extension tests for the characterization of shear behaviour in natural fibre woven fabrics, Fibers Polym. 14 (2013) 338–344. https://doi.org/10.1007/s12221-013-0338-6.

[177] F.T.I. F. T. Peirce B.Sc., F.Inst.P., The "Handle" of Cloth As a Measurable Quantity, J. Text. Inst. Trans. 21 (1930) 1930. http://www.tandfonline.com/doi/abs/10.1080/19447023008661529#.VJoYM14gAA.

[178] Z.Q. Du, T. Zhou, N. Yan, S. Hua, W.D. Yu, Measurement and characterization of bending stiffness for fabrics, Fibers Polym. 12 (2011)

104–110. https://doi.org/10.1007/s12221-011-0104-6.

[179] R. Parachuru, the Kawabata Evaluation System and Its Applications, 100 (2002).

[180] R. Sourki, B. Khatir, S. Shaikhzadeh Najar, R. Vaziri, A.S. Milani, Characterization of the dissipative large deformation bending response of dry fabric composites as occurs during forming, Compos. Struct. 310 (2023) 116728. https://doi.org/10.1016/j.compstruct.2023.116728.

[181] S. Iqbal, B. Li, K. Sonta, R.C. Ihuaenyi, X. Xiao, Probabilistic finite element analysis of sheet molding compound composites with an extended strength distribution model, Finite Elem. Anal. Des. 214 (2023) 103865. https://doi.org/10.1016/j.finel.2022.103865.

[182] S.C. Lee, S.T. Jeong, J.N. Park, S. jin Kim, G.J. Cho, A study on mechanical properties of carbon fiber reinforced plastics by three-point bending testing and transverse static response, J. Mater. Process. Technol. 201 (2008) 761–764. https://doi.org/10.1016/j.jmatprotec.2007.11.248.

[183] M. Tourlonias, M.A. Bueno, D. Poquillon, Friction of carbon tows and fine single fibres, Compos. Part A Appl. Sci. Manuf. 98 (2017) 116–123. https://doi.org/10.1016/j.compositesa.2017.03.017.

[184] I. Etsion, Leonardo da Vinci's Friction Experiments: An Old Story Acknowledged and Repeated, Tribol. Lett. 58 (2015). https://doi.org/10.1007/s11249-015-0504-7.

[185] ASTM D1894 - 14, Standard Test Method for Static and Kinetic Coefficients of Friction of Plastic Film and Sheeting, 2014. https://doi.org/10.1520/D1894-14.2.

[186] N. Fulleringer, J.F. Bloch, Forced stick-slip oscillations allow the measurement of the friction force: Application to paper materials, Tribol. Int. 91 (2015) 94–98. https://doi.org/10.1016/j.triboint.2015.06.021.

[187] K.A. Fetfatsidis, D. Jauffrès, J.A. Sherwood, J. Chen, Characterization of the tool/fabric and fabric/fabric friction for woven-fabric composites during the thermostamping process, Int. J. Mater. Form. 6 (2013) 209–221. https://doi.org/10.1007/s12289-011-1072-5.

[188] K.A. Fetfatsidis, L.M. Gamache, J.L. Gorczyca, J.A. Sherwood, D. Jauffrès,

J. Chen, Design of an apparatus for measuring tool/fabric and fabric/fabric friction of woven-fabric composites during the thermostamping process, Int. J. Mater. Form. 6 (2013) 1–11. https://doi.org/10.1007/s12289-011-1058-3.

[189] J.Y. Kim, Y.T. Hwang, J.H. Baek, W.Y. Song, H.S. Kim, Study on inter-ply friction between woven and unidirectional prepregs and its effect on the composite forming process, Compos. Struct. 267 (2021) 113888. https://doi.org/10.1016/j.compstruct.2021.113888.

[190] G. Lebrun, M.N. Bureau, J. Denault, Thermoforming-stamping of Continuous Glass Fiber/Polypropylene Composites: Interlaminar and Tool-Laminate Shear Properties, J. Thermoplast. Compos. Mater. 17 (2004) 137–165. https://doi.org/10.1177/0892705704035411.

[191] B. Cornelissen, B. Rietman, R. Akkerman, Frictional behaviour of high performance fibrous tows: Friction experiments, Compos. Part A Appl. Sci. Manuf. 44 (2013) 95–104. https://doi.org/10.1016/j.compositesa.2012.08.024.

[192] I.F. Brown, C.J. Burgoyne, The friction and wear of Kevlar 49 sliding against aluminium at low velocity under high contact pressures, Wear 236 (1999) 315–327. https://doi.org/10.1016/S0043-1648(99)00293-8.

[193] S.V. Lomov, Deformability of textile performs in the manufacture of non-crimp fabric composites, Woodhead Publishing Limited, 2011. https://doi.org/10.1533/9780857092533.2.117.

[194] H. Krieger, D. Kaufmann, T. Gries, Kinematic drape algorithm and experimental approach for the design of tailored non-crimp fabrics, Key Eng. Mater. 651–653 (2015) 393–398. https://doi.org/10.4028/www.scientific.net/KEM.651-653.393.

[195] R. Fitas, S. Hesseler, S. Wist, C. Greb, Kinematic draping simulation optimization of a composite B-pillar geometry using particle swarm optimization, Heliyon 8 (2022) e11525. https://doi.org/10.1016/j.heliyon.2022.e11525.

[196] B. Fengler, L. Kärger, F. Henning, A. Hrymak, Multi-objective patch optimization with integrated kinematic draping simulation for continuous–discontinuous fiber-reinforced composite structures, J. Compos. Sci. 2 (2018). https://doi.org/10.3390/jcs2020022.

[197] A.K. Pickett, G. Creech, P. De Luca, Simplified and advanced simulation

methods for prediction of fabric draping methods for prediction of fabric draping, Rev. Eur. Des Éléments (2012) 37–41.

[198] B. Yang, T. Jin, F. Bi, J. Li, A geometry information based fishnet algorithm for woven fabric draping in liquid composite molding, Medziagotyra 20 (2014) 513–521. https://doi.org/10.5755/j01.ms.20.4.6075.

[199] X. Sun, J.P.H. Belnoue, A. Thompson, B. El Said, S.R. Hallett, Dry Textile Forming Simulations: A Benchmarking Exercise, Front. Mater. 9 (2022) 1–20. https://doi.org/10.3389/fmats.2022.831820.

[200] S. Chen, F. Yu, Process simulation: Fabric forming, in: L. Harper, M. Clifford (Eds.), Des. Manuf. Struct. Compos., 1st ed., Elsevier Ltd., Cambridge, MA, 2023: pp. 373–396.

[201] P. Harrison, W.R. Yu, A.C. Long, Rate dependent modelling of the forming behaviour of viscous textile composites, Compos. Part A Appl. Sci. Manuf. 42 (2011) 1719–1726. https://doi.org/10.1016/j.compositesa.2011.07.026.

[202] ANSYS, Discussion of Implicit and Explicit Methods and Time-step Size, (2020).

[203] D. Durville, Simulation of the mechanical behaviour of woven fabrics at the scale of fibers, Int. J. Mater. Form. 3 (2010) 1241–1251. https://doi.org/10.1007/s12289-009-0674-7.

[204] N. Naouar, E. Vidal-Salle, J. Schneider, E. Maire, P. Boisse, 3D composite reinforcement meso F.E. analyses based on X-ray computed tomography, Compos. Struct. 132 (2015) 1094–1104. https://doi.org/10.1016/j.compstruct.2015.07.005.

[205] J. Sirtautas, A.K. Pickett, P. Lépicier, A mesoscopic model for coupled drape-infusion simulation of biaxial Non-Crimp Fabric, Compos. Part B Eng. 47 (2013) 48–57. https://doi.org/10.1016/j.compositesb.2012.09.088.

[206] X. Zeng, A. Endruweit, L.P. Brown, A.C. Long, Numerical prediction of in-plane permeability for multilayer woven fabrics with manufacture-induced deformation, Compos. Part A Appl. Sci. Manuf. 77 (2015) 266–274. https://doi.org/10.1016/j.compositesa.2015.03.027.

[207] P. Boisse, N. Hamila, F. Helenon, B. Hagege, J. Cao, Different approaches for woven composite reinforcement forming simulation, Int. J. Mater. Form.

1 (2008) 21–29. https://doi.org/10.1007/s12289-008-0002-7.

[208]   B. LIANG, P. BOISSE, A review of numerical analyses and experimental characterization methods for forming of textile reinforcements, Chinese J. Aeronaut. 34 (2021) 143–163. https://doi.org/10.1016/j.cja.2020.09.027.

[209]   A.J. Thompson, B. El Said, J.P.H. Belnoue, S.R. Hallett, Modelling process induced deformations in 0/90 non-crimp fabrics at the meso-scale, Compos. Sci. Technol. 168 (2018) 104–110. https://doi.org/10.1016/j.compscitech.2018.08.029.

[210]   P. Xue, X. Peng, J. Cao, A non-orthogonal constitutive model for characterizing woven composites, Compos. Part A Appl. Sci. Manuf. 34 (2002) 183–193. https://doi.org/https://doi.org/10.1016/S1359-835X(02)00052-0.

[211]   P. Boisse, Y. Aimène, A. Dogui, S. Dridi, S. Gatouillat, N. Hamila, M.A. Khan, T. Mabrouki, F. Morestin, E. Vidal-Sallé, Hypoelastic, hyperelastic, discrete and semi-discrete approaches for textile composite reinforcement forming, Int. J. Mater. Form. 3 (2010) 1229–1240. https://doi.org/10.1007/s12289-009-0664-9.

[212]   D. Jauffrès, J.A. Sherwood, C.D. Morris, J. Chen, Discrete mesoscopic modeling for the simulation of woven-fabric reinforcement forming, Int. J. Mater. Form. 3 (2010) 1205–1216. https://doi.org/10.1007/s12289-009-0646-y.

[213]   N. Hamila, P. Boisse, F. Sabourin, M. Brunet, A semi-discrete shell finite element for textile compositereinforcement forming simulation, Int. J. Numer. Methods Eng. 79 (2009). https://doi.org/0.1002/nme.2625.

[214]   R.H.W. ten Thije, R. Akkerman, A multi-layer triangular membrane finite element for the forming simulation of laminated composites, Compos. Part A Appl. Sci. Manuf. 40 (2009) 739–753. https://doi.org/10.1016/j.compositesa.2009.03.004.

[215]   A. Drews, Standard Test Method for Static and Kinetic Coefficients of Friction of Plastic Film and Sheeting, Man. Hydrocarb. Anal. 6th Ed. (2008) 545-545–3. https://doi.org/10.1520/mnl10913m.

[216]   P. Harrison, Modelling the forming mechanics of engineering fabrics using a mutually constrained pantographic beam and membrane mesh, Compos.

Part A Appl. Sci. Manuf. 81 (2016) 145–157. https://doi.org/10.1016/j.compositesa.2015.11.005.

[217] H. Lin, J. Wang, A.C. Long, M.J. Clifford, P. Harrison, Predictive modelling for optimization of textile composite forming, Compos. Sci. Technol. 67 (2007) 3242–3252. https://doi.org/10.1016/j.compscitech.2007.03.040.

[218] F. Yu, S. Chen, L.T. Harper, N.A. Warrior, Double diaphragm forming simulation using a global-to-local modelling strategy for detailed defect detection in large structures, Compos. Part A Appl. Sci. Manuf. 147 (2021). https://doi.org/10.1016/j.compositesa.2021.106457.

[219] P. Boisse, J. Colmars, N. Hamila, N. Naouar, Q. Steer, Bending and wrinkling of composite fiber preforms and prepregs. A review and new developments in the draping simulations, Compos. Part B Eng. 141 (2018) 234–249. https://doi.org/10.1016/j.compositesb.2017.12.061.

[220] F. Schäfer, H.O. Werner, F. Henning, L. Kärger, A hyperelastic material model considering biaxial coupling of tension–compression and shear for the forming simulation of woven fabrics, Compos. Part A Appl. Sci. Manuf. 165 (2023) 107323. https://doi.org/10.1016/j.compositesa.2022.107323.

[221] D. Dörr, F.J. Schirmaier, F. Henning, L. Kärger, A viscoelastic approach for modeling bending behavior in finite element forming simulation of continuously fiber reinforced composites, Compos. Part A Appl. Sci. Manuf. 94 (2017) 113–123. https://doi.org/10.1016/j.compositesa.2016.11.027.

[222] A. Iwata, T. Inoue, N. Naouar, P. Boisse, S. V. Lomov, Coupled meso-macro simulation of woven fabric local deformation during draping, Compos. Part A Appl. Sci. Manuf. 118 (2019) 267–280. https://doi.org/10.1016/j.compositesa.2019.01.004.

[223] F. Yu, S. Chen, J. V. Viisainen, M.P.F. Sutcliffe, L.T. Harper, N.A. Warrior, A macroscale finite element approach for simulating the bending behaviour of biaxial fabrics, Compos. Sci. Technol. 191 (2020). https://doi.org/10.1016/j.compscitech.2020.108078.

[224] M. Nishi, T. Hirashima, T. Kurashiki, M. Kurose, T. Kaburagi, K. Uenishi, Thermoforming simulation of thermoplastic pre-impregnated textile reinforcement, in: ICCM Int. Conf. Compos. Mater., 2015.

[225] E. Lund, 4-Node Stabilised Shell Element Accounting for Large

Displacements , Drilling and Draping in Structural Optimisation of Laminated Composites, 2023.

[226] E. Guzman-Maldonado, P. Wang, N. Hamila, P. Boisse, Experimental and numerical analysis of wrinkling during forming of multi-layered textile composites, Compos. Struct. 208 (2019) 213–223. https://doi.org/10.1016/j.compstruct.2018.10.018.

[227] W. Xing, J. Zhang, C. Song, F. Tin-Loi, A node-to-node scheme for three-dimensional contact problems using the scaled boundary finite element method, Comput. Methods Appl. Mech. Eng. 347 (2019) 928–956. https://doi.org/10.1016/j.cma.2019.01.015.

[228] B.K. Zimmerman, G.A. Ateshian, A Surface-to-Surface Finite Element Algorithm for Large Deformation Frictional Contact in febio, J. Biomech. Eng. 140 (2018) 1–15. https://doi.org/10.1115/1.4040497.

[229] SIMULIA, Abaqus User Assistance 2022, (2022).

[230] O. Seward, F. Cepero-Mejías, J.P.A. Fairclough, K. Kerrigan, Development of a Novel Friction Model for Machining Simulations in Unidirectional Composite Materials, Polymers (Basel). 14 (2022) 1–19. https://doi.org/10.3390/polym14050847.

[231] Technical Data Sheet - VACflexP, Hinckley, United Kingdom, n.d. www.vacinnovation.com.

[232] S. Bel, N. Hamila, P. Boisse, F. Dumont, Finite element model for NCF composite reinforcement preforming: Importance of inter-ply sliding, Compos. Part A Appl. Sci. Manuf. 43 (2012) 2269–2277. https://doi.org/10.1016/j.compositesa.2012.08.005.

[233] B. Chen, T.W. Chou, Compaction of woven-fabric preforms in liquid composite molding processes: Single-layer deformation, Compos. Sci. Technol. 59 (1999) 1519–1526. https://doi.org/10.1016/S0266-3538(99)00002-0.

[234] L. Montero, S. Allaoui, G. Hivet, Characterisation of the mesoscopic and macroscopic friction behaviours of glass plain weave reinforcement, Compos. Part A Appl. Sci. Manuf. 95 (2017) 257–266. https://doi.org/10.1016/j.compositesa.2017.01.022.

[235] S. Allaoui, G. Hivet, A. Wendling, P. Ouagne, D. Soulat, Influence of the dry woven fabrics meso-structure on fabric/fabric contact behavior, J. Compos. Mater. 46 (2012) 627–639. https://doi.org/10.1177/0021998311424627.

[236] D. Bublitz, D. Colin, K. Drechsler, Implementation of a viscoelastic material model to predict the compaction response of dry carbon fiber preforms, Compos. Part A Appl. Sci. Manuf. 153 (2022). https://doi.org/10.1016/j.compositesa.2021.106718.

[237] S. Kulkarni, K.A. Khan, K. Alhammadi, W.J. Cantwell, R. Umer, A visco-hyperelastic approach to model rate dependent compaction response of a 3D woven fabric, Compos. Part A Appl. Sci. Manuf. 163 (2022) 107229. https://doi.org/10.1016/j.compositesa.2022.107229.

[238] M.A. Kabachi, M. Danzi, S. Arreguin, P. Ermanni, Experimental study on the influence of cyclic compaction on the fiber-bed permeability, quasi-static and dynamic compaction responses, Compos. Part A Appl. Sci. Manuf. 125 (2019) 105559. https://doi.org/10.1016/j.compositesa.2019.105559.

[239] L. Jiang, H. Xiong, T. Zeng, J. Wang, S. Xiao, L. Yang, In-situ micro-CT damage analysis of carbon and carbon/glass hybrid laminates under tensile loading by image reconstruction and DVC technology, Compos. Part A Appl. Sci. Manuf. 176 (2024) 107844. https://doi.org/10.1016/j.compositesa.2023.107844.

[240] R. Karamov, L.M. Martulli, M. Kerschbaum, I. Sergeichev, Y. Swolfs, S. V. Lomov, Micro-CT based structure tensor analysis of fibre orientation in random fibre composites versus high-fidelity fibre identification methods, Compos. Struct. 235 (2020) 111818. https://doi.org/10.1016/j.compstruct.2019.111818.

[241] T.B. Nguyen Thi, M. Morioka, A. Yokoyama, S. Hamanaka, K. Yamashita, C. Nonomura, Measurement of fiber orientation distribution in injection-molded short-glass-fiber composites using X-ray computed tomography, J. Mater. Process. Technol. 219 (2015) 1–9. https://doi.org/10.1016/j.jmatprotec.2014.11.048.

[242] A.A. Somashekar, S. Bickerton, D. Bhattacharyya, Compression deformation of a biaxial stitched glass fibre reinforcement: Visualisation and image analysis using X-ray micro-CT, Compos. Part A Appl. Sci. Manuf. 42 (2011)

140–150. https://doi.org/10.1016/j.compositesa.2010.10.017.

[243] Ultralytics, Ultralytics YOLOv8, GitHub (2023). https://github.com/ultralytics/ultralytics (accessed June 5, 2023).

[244] J. Solawetz, Francesco, What is YOLOv8? The Ultimate Guide., Roboflow (2023) 1–15. https://blog.roboflow.com/whats-new-in-yolov8/ (accessed August 8, 2023).

[245] J. Terven, D. Cordova-Esparza, A Comprehensive Review of YOLO: From YOLOv1 to YOLOv8 and Beyond, (2023) 1–31. http://arxiv.org/abs/2304.00501.

[246] P. Galvez-Hernandez, J. Kratz, Annotator bias and its effect on deep learning segmentation of uncured composite micrographs, NDT E Int. 144 (2024) 103088. https://doi.org/10.1016/j.ndteint.2024.103088.

[247] S. Li, General unit cells for micromechanical analyses of unidirectional composites, Compos. - Part A Appl. Sci. Manuf. 32 (2001) 815–826. https://doi.org/10.1016/S1359-835X(00)00182-2.

[248] H.-C. Chang, L.-C. Wang, A Simple Proof of Thue's Theorem on Circle Packing, (2010) 1–4. http://arxiv.org/abs/1009.4322.

[249] F. Gommer, A. Endruweit, A.C. Long, Analysis of filament arrangements and generation of statistically equivalent composite micro-structures, Compos. Sci. Technol. 99 (2014) 45–51. https://doi.org/10.1016/j.compscitech.2014.05.008.

[250] F. Gommer, A. Endruweit, A.C. Long, Quantification of micro-scale variability in fibre bundles, Compos. Part A Appl. Sci. Manuf. 87 (2016) 131–137. https://doi.org/10.1016/j.compositesa.2016.04.019.

[251] Y. Sinchuk, P. Kibleur, J. Aelterman, M.N. Boone, W. Van Paepegem, Geometrical and deep learning approaches for instance segmentation of CFRP fiber bundles in textile composites, Compos. Struct. 277 (2021) 114626. https://doi.org/10.1016/j.compstruct.2021.114626.

[252] M. Henke, G. Gerlach, A multi-layered variable stiffness device based on smart form closure actuators, J. Intell. Mater. Syst. Struct. 27 (2016) 375–383. https://doi.org/10.1177/1045389X15577645.

[253] H. Alshahrani, M. Hojjati, Influence of double-diaphragm vacuum

compaction on deformation during forming of composite prepregs, J. Sci. Adv. Mater. Devices 1 (2016) 507–511. https://doi.org/10.1016/j.jsamd.2016.09.003.

[254]   K.J. Johnson, R. Butler, E.G. Loukaides, C. Scarth, A.T. Rhead, Stacking sequence selection for defect-free forming of uni-directional ply laminates, Compos. Sci. Technol. 171 (2019) 34–43. https://doi.org/10.1016/j.compscitech.2018.11.048.

[255]   F. Yu, S. Chen, G.D. Lawrence, N.A. Warrior, L.T. Harper, A global-to-local sub modelling approach to investigate the effect of lubrication during double diaphragm forming of multi-ply biaxial non-crimp fabric preforms, Compos. Part B Eng. 254 (2023) 13–16. https://doi.org/10.1016/j.compositesb.2023.110590.

[256]   P. Harrison, M.F. Alvarez, D. Anderson, Towards comprehensive characterisation and modelling of the forming and wrinkling mechanics of engineering fabrics, Int. J. Solids Struct. 154 (2018) 2–18. https://doi.org/10.1016/j.ijsolstr.2016.11.008.

Appendices

Appendix A – SEM Imaging of FCIM359

A series of micrographs were obtained using scanning electron microscopy (SEM; FEI XL30; 10 kV; spot size 4.5 μm; 10.5 mm working distance; secondary electron (SE) imaging mode). Imaging of the FCIM359 (see Table 3.1 for material properties) was performed to visualise how increases in microscale filament contact area might directly contribute to the generation of larger frictional forces. The fabric samples were coated with platinum to maximise conductivity and improve the final image quality. It should be noted that the images produced were not subjected to any compaction load prior to or during scanning.

The figure shows 3 examples of areas of the fabric, increasing in magnification from 569x to up to 9416x. As the aspect ratio of the bundles and contact area between them increases, the more individual fibres of opposing plies come into contact with one another. In the images with the highest magnification, it can be seen that the fibres are not perfectly smooth as there are asperities on the surface. These asperities are caused by the application of sizing to the fabric, as well as flaws in the surface of the carbon fibres themselves. The influence of asperities on the microscale contact and frictional behaviour of surfaces has been widely studied, such as in the work of Greenwood and Williamson [126]. As the increase in load is not borne by a directly proportional number of asperities (due to the non-linear deformation of the fibre bundles), the frictional forces produced by the shear strength of the asperities will not be directly proportional to the applied load. Unlike high stiffness materials such as metals, the inter-

ply coefficient of friction of a deformable fabric is subsequently dependent on the normal load applied to the sliding interface. Therefore, to further improve the understanding of the relationship of macroscale ply-ply friction and applied normal load, further microscale analyses may be required.